UNIVERSITY OF CALIFORNIA
SANTA CRUZ

THE CRUSTS OF MARS, TETHYS, AND MIMAS: GEOPHYSICAL EXPLORATION OF HISTORIC HEAT FLOW

A dissertation submitted in partial satisfaction of the
requirements for the degree of

DOCTOR OF PHILOSOPHY

in

EARTH SCIENCE

by

Szilárd Gyalay

June 2023

The Dissertation of Szilárd Gyalay
is approved:

Professor Francis Nimmo, Chair

Professor Ian Garrick-Bethell

Professor Slawomir Tulaczyk

Professor Isamu Matsuyama

Peter Biehl
Vice Provost and Dean of Graduate Studies

Table of Contents

List of Figures

List of Tables

Abstract

The Crusts of Mars, Tethys, and Mimas:

Geophysical Exploration of Historic Heat Flow

by

Szilárd Gyalay

The evolution of a planetary body often determines and is determined by its thermal properties. In my first project, I explore the consequences of heating upon pore closure, allowing me to estimate the heat flow through the Martian crust during the latest significant pore generation event—likely large basin-forming impacts. We apply a pore closure model developed for the Moon to Mars and take into account the geological processes that may alter the depth of a transition between porous and competent crust. If the 8–11 km deep discontinuity in seismic wave speed detected by the InSight lander marks the base of the uppermost porous layer of the Martian crust, then the heat flux at the time the porosity was created must exceed 60 mW m^{-2}, indicating a time prior to 4 Ga. Then, I explore how the global shape of an icy satellite allows us to infer its heat budget and interior—including the presence or absence of a subsurface global ocean. I apply this method in my second and third projects to Tethys and Mimas, respectively. We assume spatial variations in tidal heating are responsible for thickness or temperature variations in an isostatic ice shell, which manifests as surface topography. For Saturn's moon Tethys, our best-fit models require Pratt isostasy and obliquity tides, with a normalized moment of inertia 0.340-0.345 and an average surface heat flux 1-

2 mW m^{-2}. Then, we find that to account for its hydrostaic shape, Mimas' normalized moment of inertia is 0.375, indicating a relatively undifferentiated world. Its remaining topography is consistent with a ∼30 km thick conductive ice shell in Airy isostasy atop a weakly convecting ∼30 km thick layer that itself mantles a ∼140 km radius ice-rock interior. For neither satellite do we find an ocean. However, the total power and pattern inferred to produce both satellites' shapes from tidal heating indicate an ancient era of high obliquity. The common thread of all three projects is the flow of heat, and how our understanding of it can be revealed by or can reveal properties of the planetary bodies we study.

To all who believed in me, even when I could not believe in myself.

—

We are creatures born of heat and pressure and grinding, ceaseless movement. To be still is to be... not alive.

But what is important is that you know it was not all terrible. There was peace in long stretches, between each crisis. A chance to cool and solidify before the grind resumed.

—*The Fifth Season*, by N.K. Jemisin

Acknowledgments

In fourth grade, my teacher asked if I was going to do grad school. In retrospect, that is far too early a moment to ask that sort of question, but this was the first I had ever actually heard of graduate school as a concept. Being that I—both then as a fourth grader and still to this day—loved learning, I, of course, naïvely said yes. Over the years since, I had considered it on and off, pondering whether I was just vain enough to want "Dr." in front of my name. Then when I was a freshman at UCLA, I learned that not only is grad school free for scientists earning their PhD, but the university actually pays *you* to do research. It was, as the kids say, all downhill from there. Thus, I dutifully acknowledge Ms. Dani for putting the seed of going to grad school in my head.

Another teacher I want to acknowledge is my high school physics and calculus teacher, Mr. Carlyle. He probably did the most to set me on the physics-and-math-heavy path I am on today. Additionally I would like to thank all those who advised me in my research, including Prof. Dave Paige, Dr. Eldar Noe Dobrea, Dr. Marissa Vogt, and (of course) my PhD advisor, Prof. Francis Nimmo. All of you have provided me a great deal of help as I swam through this sea we call science. I would also be remiss not to acknowledge the administrative staff of the fine institutions I was fortunate enough to attend. For instance, at UC Santa Cruz I would never have gotten anything done without Jennifer Fish.

I also acknowledge my parents, who during all of my schooling encouraged striving to be the very best in all my educational and research endeavors. Not to

mention the warm meals and much love. I could not even dream of getting this far without your support.

Then while my PhD had the misfortune of occurring in "interesting times," I am glad to have had the chance to become close friends with many of the fellow grad students in my cohort and in the planetary sciences in the few years before the pandemic started. This proved to be an invaluable support network during what turned out to be some of the toughest years of grad school. This includes (at a bare minimum!), the lovely house I lived in my first year at Santa Cruz withso Segre Drive with Araceli, Colleen, Kélian, and Zack; my fellow planetary grad students, Brynna, Carver, Coby, Huazhi, Jack, Jill, Kara, Linfeng, Megan, Nathan, Nick, Rachel, Secana, and Wencheng; the planetary post-docs including Ben and Xinting; and those others who would join us at lunch, including Adrienne, Sarah, and Will. Along with them were the other friends I have made over the years, some going back all the way to my middle school days. With you all, I was able to take much-needed breaks from grad school life to play D&D, play video games, and rock climb. This includes Alba, Alex, Anastasia, Bob, Brian, Daniel, Emma, Kalvin, Kevin, Mac, Ryan, Sharon, Sophia, Teja, and Willie. Then of course, my escape-room crew (among other wonderful activities), the Wild Scallions: Chanel, Han, Liya, Lynn, and Patty. There are likely many names I forgot to list just now, but if you know me—you already know how horrible I am with names.

Perhaps most important, however, is Liya. You have been my partner at my side for many years, and I truly could not have done any of this without you. Thank you, and I look forward to many more years at your side.

Previously published material

The text of this thesis includes modified reprints of the following previously published material:

C. 2: S. Gyalay, F. Nimmo, A.-C. Plesa, and M.A. Wieczorek (2020). "Constraints on Thermal History of Mars From Depth of Pore Closure Below InSight." *Geophysical Research Letters 47*(16), e2020GL088653. doi: 10.1029/2020GL088653

C. 3: S. Gyalay and F. Nimmo (2023). "Estimates for Tethys' Moment of Inertia, Heat Flux Distribution, and Interior Structure from its Long-Wavelength Topography." *Journal of Geophysical Research: Planets 128*(2), e2022JE007550. doi: 10.1029/2022JE007550

Chapter 1

Constraints on Thermal History of Mars from Depth of Pore Closure Below InSight

> My attention was quickly riveted by a large red star close to the distant horizon. As I gazed upon it I felt a spell of overpowering fascination—it was Mars, the god of war, and for me, the fighting man, it had always held the power of irresistible enchantment. As I gazed at it on that far-gone night it seemed to call across the unthinkable void, to lure me to it, to draw me as the lodestone attracts a particle of iron.
>
> —*A Princess of Mars*, by Edgar Rice Burroughs

This chapter is a slightly modified reprint of work previously published as S. Gyalay, F. Nimmo, A.-C. Plesa, and M.A. Wieczorek (2020). "Constraints on Thermal History of Mars From Depth of Pore Closure Below InSight." *Geophysical Research Letters 47*(16), e2020GL088653. doi: 10.1029/2020GL088653

Key Points

- The depth of porosity in Mars' crust depends most on the maximum heat flux after pore generation.
- A seismic discontinuity at a depth of 8-11 km, as suggested by InSight, could be interpreted as the depth of porosity in the crust.
- If pores closed at 8-11 km depth, it indicates pores formed at least 4 billion years ago when heat flow was at least 60 mW m^{-2}.

Abstract

Planetary crusts undergo viscous closure of pores at depth; if the thickness of this porous layer can be measured, constraints on crustal thermal evolution can be derived. We apply a pore closure model developed for the Moon to Mars and take into account the geological processes that may alter the depth of this transition region. If the 8–11 km deep discontinuity in seismic wave speed detected by the InSight lander marks the base of the porous layer, the heat flux at the time the porosity was created must exceed 60 mW m^{-2}, probably indicating a time prior to 4 Ga.

Plain Language Summary

On long timescales, and with enough heat or pressure, rocks in the crust of a planet can flow. This viscous deformation allows the empty pore spaces in a rock

to close up. The history of the temperature at depth plays an important role in how deep one may expect porosity to exist. One can use a computational model to calculate the thickness of this porous layer as a function of the crust's thermal history. If the InSight Mars lander detects the thickness of such a porous layer, we can estimate the necessary temperature structure of the Martian crust and when porosity in the crust was generated. From a potential measurement of this porous layer at around 10 kilometers thick, we predict the last significant pore formation event to have occurred at least 4 billion years ago.

1.1 Introduction

The porosity structure of the Martian crust is important for several reasons. It controls the crustal water carrying capacity (e.g. Clifford, 1993) and affects its near-surface thermal structure (Parmentier and Zuber, 2007). Furthermore, the porosity is an indication of the geological processes that have affected the crust, such as impact cratering, volcanism, and the emplacement of sediments. Less obviously, it contains a record of the thermal evolution of Mars, modulated by the history of crustal growth. Pores can close via plastic/viscous flow at a rate that is highly dependent on temperature (Hanna and Phillips, 2005); accordingly, if the depth to the base of the porous region can be established, the corresponding thermal structure may be deduced.

On the Moon, the presence of a porous layer roughly 40–85 km thick was identified using the very high resolution gravity data provided by GRAIL (Wieczorek

et al., 2013; Besserer et al., 2014). The depth to the base of this layer was found to be consistent with models of viscous pore closure using simple lunar temperature structures (Wieczorek et al., 2013). In regions where the total crustal thickness is less than the depth of pore-closure, the uppermost mantle also likely maintains porosity (Wieczorek et al., 2013). Thermally-driven pore closure has also been modeled on icy satellites (e.g. Kossacki and Lorenz, 1996; Eluszkiewicz, 2004; Besserer et al., 2013) and on asteroids (e.g. Neumann et al., 2015; Gail et al., 2015). On the Moon, production of deep porosity was undoubtedly dominated by large impacts early in its history, and we will assume that the same is true for Mars.

Some studies of Martian aquifers (Clifford, 1993; Clifford and Parker, 2001) modeled porosity in Mars' crust as an exponential decay, scaled from a relationship hypothesized for the Moon, and observed in some geologic environments on Earth (e.g. Schmoker and Gautier, 1988). These relations focused on an elastic closure of pore space. At higher pressures or temperatures, rock deforms via ductile creep (Wong and Baud, 2012). On Earth, Manning and Ingebritsen (1999) interpret a drop in permeability at $\sim$12 km depth due to ductile creep closing pores. Because of the lower gravity (and thus reduced elastic closure) on the Moon and Mars in conjunction with high heating early in their history, it is the latter process which we focus on in this work.

On the Moon, an apparent decay in seismic scattering with depth has been used to infer the depth to which fractured rocks extend (Gillet et al., 2017). In a similar fashion, the recent emplacement of the InSight seismometer on the Martian surface provides the possibility of measuring the thickness of the porous layer. In this work, we

carry out simple models of viscous pore closure for the Martian crust and show how the thickness of the porous layer can be related to the peak heat flux experienced. In Section 1.2, we review the mathematics of viscous pore closure. In section 1.3, we investigate the potential confounding effects of geological processes of Mars' crust. In Section 1.4 we use a detected seismic discontinuity beneath InSight to quantify the thermal environment at the landing site when pore formation stopped, and thus determine *when* it stopped. We conclude with Section 1.5.

1.2 Viscous Closure of Pores on Mars

We approach the problem in a similar fashion to Wieczorek et al. (2013) and references within (i.e. Fowler, 1985; Nimmo et al., 2003; Eluszkiewicz, 2004). How quickly the porosity ϕ closes over time t depends on the dynamic viscosity of the materials η and the overburden pressure P:

$$\frac{\partial \phi}{\partial t} = -\phi \frac{P}{\eta}. \tag{1.1}$$

Pressure $P{=}\rho g z$ where ρ is crustal density, g is gravitational acceleration, and z is depth in the crust.

Under high pressures, viscosity does not depend on grain size but does depend on stress σ, rheological constants A and n, an activation energy Q, and the gas constant R:

$$\eta = \frac{\sigma^{1-n}}{A} \exp\left(\frac{Q}{RT}\right). \tag{1.2}$$

We take this stress to be equal to the overburden pressure, $\sigma = P$. In reality there is a

constant of proportionality of order unity in Equation 1.1 depending on the relationship of overburden pressure to the deviatoric stress, and the ratio of initial to current porosity (e.g. Eluszkiewicz, 2004). However, since the heat flux necessary for pore closure ultimately depends on the logarithm of P (Section 1.2.3), neglecting this constant does not introduce significant errors. For instance, substituting $\sigma = 0.1P$ instead of $\sigma = P$ in Equation 1.1 depresses the depth of pore closure by $\sim$2 km.

1.2.1 Constant Heat Flux Case

For the case of constant temperature, we solve Equation 1.1 to find ϕ relative to some initial porosity ϕ_0 after some elapsed time t as

$$\phi = \phi_0 \exp\left(\frac{-Pt}{\eta}\right). \tag{1.3}$$

For an initially porous crust, we can use this equation to calculate how much the porosity at each depth has changed as a function of time. We assume pores have effectively closed when they reach a critical porosity that is a factor of e^2 less than the initial. The depth of the porous layer after some time is then limited by where porosity is still present; because of the strong temperature-dependence of viscosity, the transition to pore-free material is typically abrupt (less than a few km; Figure 1.1a). Because this transition is abrupt, the exact pore-closure criterion matters very little: one can take the characteristic criterion to be a factor of e or 10 and achieve nearly identical results.

For our nominal model, we use a gravitational acceleration of 3.7 m s^{-2}, an upper crustal density of 2800 kg m^{-3}, a rock thermal conductivity of 3.0 W m^{-1} K^{-1},

no crustal heat production, and a constant surface temperature of 250 K. In this investigation we model Mars with both wet and dry diabase (as used in previous investigations of Mars, see e.g. Hanna and Phillips, 2005). For wet diabase, Q =276±14 kJ Mol^{-1}, n =3.05±0.15, and A =6.12±3.06 10^{-2} MPa^{-n} s^{-1} (Caristan, 1980). Caristan (1980) did not include exact uncertainties, but noted that uncertainty in Q and n would not exceed 5%, and A could vary by a factor of 2. For dry diabase, Q =485±30 kJ Mol^{-1}, n =4.7±0.6, and A =1.9±1.1 10^2 MPa^{-n} s^{-1} (Mackwell et al., 1998). Some other parameter values are uncertain; in particular, thermal conductivity has a strong dependence on porosity as well as the contents of its pore space. We discuss the effect of these uncertainties further below and in A.

For the purpose of illustration, we assume a single rheology (wet diabase) and plot how the depth of pore closure changes through time for a range of constant heat fluxes in Figure 1.1b. Most pore closure happens in a short timespan. The depth of pore-closure over the age of the solar system, as shown in Figure 1.1b, is highly dependent on the assumed heat flux, ranging from depths of more than 50 km for low heat fluxes of about 20 mW m^{-2} to about 10 km for heat fluxes in excess of 120 mW m^{-2}. Present-day heat fluxes on Mars are expected to be roughly 20 mW m^{-2} (see below), but would have been higher at earlier times. It is thus important to take into account the time-evolution of heat flux.

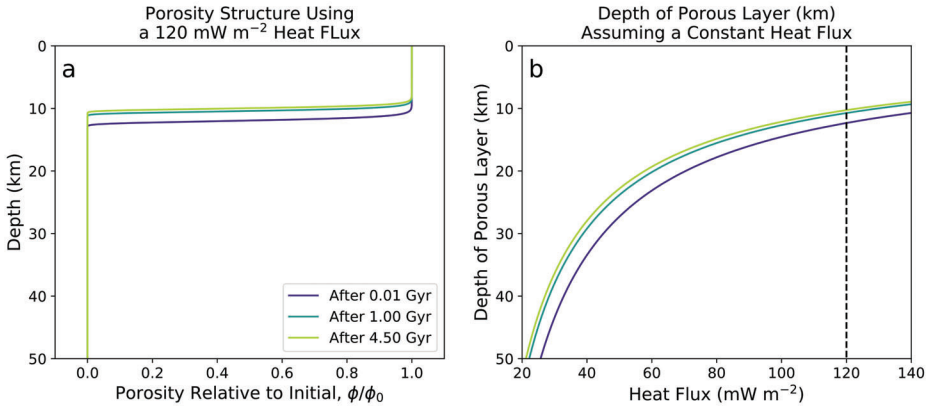

Figure 1.1: Panel a: Porosity structure after 10 Myr, 1 Gyr, and 4.5 Gyr for an assumed heat flux of 120 mW m^{-2}. Temperature structure at depth is calculated from Fourier's law of thermal conduction for a surface temperature of 250 K, a thermal conductivity of 3 W m^{-1} K^{-1}, and no crustal heat production. We use the rock rheology of wet diabase from Caristan (1980) without consideration for uncertainty. Porosity decreases from its initial value to 0 over a sharp interval of about 2 km. Panel b: Depth of pore closure (where the porosity is reduced by a factor e^2 with respect to the initial value) as a function of heat flux. The dashed line illustrates the heat flux used for (a).

1.2.2 Decreasing Heat Flux Case

To investigate the effect of a changing heat flux, we make use of a suite of thermal evolution models developed by Plesa et al. (2018). The model uses a fully 3-D geometry to model the thermal evolution and interior dynamics of Mars. We focus on their case 110, as it represents an upper bound in terms of heat flux through time. Similar to most other cases of Plesa et al. (2018), case 110 uses a crustal thermal conductivity of 3 W m^{-1} K^{-1}, latitudinal variations of the surface temperature leading to a surface temperature of 235 K at InSight location (Ohring and Mariano, 1968; Kieffer, 2013), and spatial variations of crustal thickness. The average crustal thickness of this model is 45 km and the crustal heat production rate is 20% higher than the

value suggested by GRS (Hahn et al., 2011). The crustal heat production for case 110 decreases exponentially from an initial value of 331.1 pW kg^{-1}. We note that this case matches available geophysical, geological, and petrological constraints (cf. supplementary material of Plesa et al., 2018). We use Equation 1.1 to evolve the porosity forward in time, taking into account the effect of the changing crustal temperature structure on the viscosity via Equation 1.2. Figure 1.2a shows the model surface heat flux through Martian history.

We begin the porosity evolution calculation at different points in Mars's history. In this model, porosity is assumed to be present in the crust at some time t_0, and then we compute the depth of pore closure. For each starting time point, we evolved Equation 1.1 forward in time over either 10 Myr or 1 Gyr, showing that the results are not sensitive to the total elapsed time after initation of pore closure (Figure 1.2b). Pore closure reaches shallower depths in cases when closure started earlier (when temperatures were higher). Because of the continuing decrease in heat flux, the pore closure depth is much more sensitive to the heat flux at the start of pore-closure than on the total duration of closure. In effect, the present-day depth of pore closure is a "fossil" signature of an ancient heat flux. We accordingly are justified in using an analytical approach in which the initial, maximum heat flux is calculated from the present-day depth of pore closure.

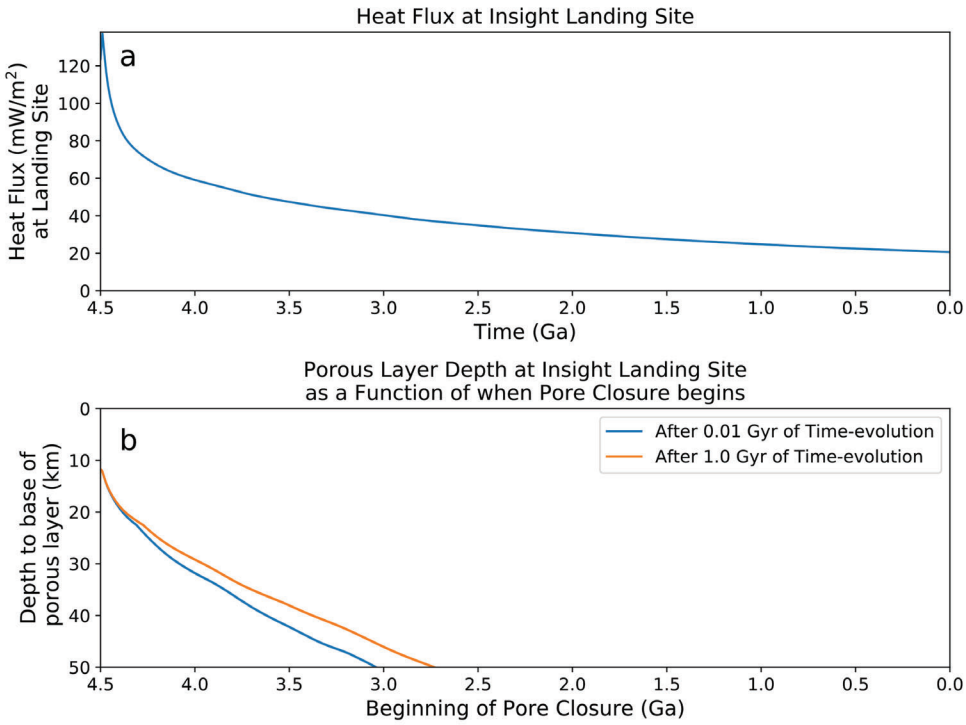

Figure 1.2: Panel a: Surface heat flux at InSight's landing site, modeled through Martian history. This particular model is case 110 from Plesa et al. (2018), and uses a thermal conductivity k=3 W m^{-1} K^{-1}. The surface temperature in this Plesa et al. (2018) model was 235 K at the InSight landing site. Crustal heat production was initially 331.1 pW kg^{-1} and decreased exponentially to 59 pW kg^{-1}. Panel b: To account for how a changing heat flux affects pore closure, we can no longer use Equation 1.3 over the total elapsed time. However, we may still employ this equation over short and successive time steps (we use 100 kyr). For example, if we begin pore closure at 4 Ga, we first assume the heat flux indicated in panel (a) for 4 Ga ($\sim$ 60 mW m^{-2}) and find porosity as a function of depth with Equations 1.2 and 1.3 after 100 kyr have elapsed. For the next time step, we use the heat flux 100 kyr after our start time and repeat the process. After the necessary number of time steps, we calculate the depth of the porous layer after 10 Myr and 1 Gyr of evolution from the corresponding start time. Due to the uncertainty in when pore-generation may have ended we allow the beginning of pore-closure to vary from 1.0-4.5 Ga. So as a function of this start time, we plot the depth of the porous layer after 10 Myr (blue line) and 1 Gyr (orange line) of heat flux evolution. We use the rock rheology of wet diabase from Caristan (1980). While porosity could continue into the upper mantle (cf. Wieczorek et al., 2013), we are primarily concerned with pore closure in the crust, as InSight has potentially detected pore closure at only $\sim$10 km depth (Lognonné et al., 2020). As such, we truncate results at depths greater than a generous crustal thickness of 50 km.

1.2.3 Necessary/Maximum Heat Flux as a Function of Pore-Closure Depth

Assume that pores close at a critical porosity ϕ_C. Rearranging Equation 1.3, the critical temperature T_C to close pores at some depth $z = (P/\rho g)$ (we account for uncertainty in the density due to porosity in A) after some time t is:

$$T_C = \frac{Q/R}{\ln\left(\frac{tP^nA}{\ln(\phi_0/\phi_C)}\right)}. \tag{1.4}$$

This expression shows that the closure temperature is strongly dependent on the activation energy Q and weakly dependent on the overburden pressure P and elapsed time t.

The temperature at depth is related to heat flux by Fourier's law of thermal conduction. We can thus determine the surface heat flux necessary to close pores at a certain depth:

$$F_C = \frac{k}{z}\left[\frac{Q/R}{\ln\left(\frac{tP^nA}{\ln(\phi_0/\phi_C)}\right)} - T_S + \frac{\rho H z^2}{2k}\right], \tag{1.5}$$

where T_S is the surface temperature, and H is the crustal heat production rate per unit mass. Because a decreasing heat flux results in little change in the depth of pore closure over time (assuming that no additional porosity is being generated, see Figure 1.2b), we can use a small elapsed time such as t=10 Myr and be confident that this results in the maximum heat flux a region can have experienced in its history.

1.3 Effects of Geology

Until now, we have made several simplifying assumptions in this analysis. We assumed pores close only viscously and neglected other ways of closing porosity such as cementation or volcanism. We also assume that the entire crust is initially porous, and that no new porosity is generated. Nonetheless, any subsurface region in which porosity is maintained can never have exceeded a given temperature since the most recent generation of porosity, placing an upper bound on the heat flux. For the Moon, it is thought that early bombardment was the main source of porosity and that the decline in impacts greatly reduced subsequent pore generation (Wieczorek et al., 2013; Wahl et al., 2020). On Mars, the last events to generate significant porosity were likely the impacts that formed the Borealis Basin (>4.47 Ga) or Hellas, Isidis, and Argyre basins (∼3.8–4.1 Ga) (Bottke and Andrews-Hanna, 2017).

In this section, we explore the regional geology near InSight and how it may affect our analysis. InSight landed in Elysium Planitia near the boundary of Mars' crustal dichotomy. From orbital data, InSight appears to have landed on a plain of early-Amazonian or late-Hesperian (∼3.0 Ga) lava flows 200-300 m thick, which overlie sedimentary rocks of Noachian age (∼3.7-4.1 Ga) (Pan et al., 2020). The sediments themselves may overlie altered basaltic rocks that are compacted at depth (Smrekar et al., 2019). The surface geology at the landing site was well-predicted by the orbital data (Golombek et al., 2020). Initial analyses of the InSight seismic data using a seismic receiver function analysis shows that there is a seismic discontinuity at 8-11 km

depth (Lognonné et al., 2020). This discontinuity occurs within the crust of Mars, and potentially indicates the presence of altered/fractured rocks to that depth (Lognonné et al., 2020).

We consider four geological phenomena that may affect the depth of pore-closure beneath the InSight landing site: sediment accumulation, emplacement of lava flows, erosion, and the presence of groundwater. If sedimentation occurred after maximum heating, the extra overburden pressure it applies at depth would not cause additional compaction but may effectively increase the depth to pore-closure by the thickness of the additional sediment. In addition, the sediments themselves would be expected to form with significant porosity (see Lewis et al., 2019). Lava flows would greatly increase the surface temperature, but the thermal anomaly will only propagate downwards to a depth comparable to the flow thickness, which is likely much less than the porous layer depth. Like sediment layers, this layer of lava would also increase the depth to pore-closure by the thickness of the deposit, and the lava flows would likely also contain some porosity (e.g. Rust et al., 1999, and references within). Erosion would remove at least some of the upper portion of the porous layer. However, there is little evidence for large scale erosive events in this region of Mars.

The presence of pore water will change the deviatoric stress. However, because of the large density contrast between water and rock, and the logarithmic dependence on P (Equation 1.5), this effect is negligible. Groundwater can also aqueously alter the mineralogy via diagenesis (see Section 1.4 below). Most importantly for our study, an aquifer can affect the temperature structure of the crust and thus the depth to which

pores close. The presence of liquid water in the pore space of Martian rock can lower the effective thermal conductivity of the rock (e.g. Hanna and Phillips, 2005)—increasing the thermal gradient and thus reducing the thickness of the porous layer. The thermal conductivity of the Martian crust may be somewhere between 2 and 3 W m^{-1} K^{-1} (e.g. Clauser and Huenges, 1995; Seipold, 1998) while water's thermal conductivity is 0.57 W m^{-1} K^{-1} (Demming, 2002). A similar reduction in conductivity will arise if the pores are empty rather than water-filled. Uncertainty in the thermal conductivity has the largest effect on the uncertainty in the calculated maximum heat flux (see Appendix A).

Another possibility to consider is if water in the pore-space of the Martian crust is undergoing convection. This is important because convection decreases the thermal gradient—making the required heat flux to close pores at a given depth under the assumption of conduction (Equation 1.5) an underestimate. We can calculate whether the fluid would convect using the Rayleigh number for a fluid in a porous medium:

$$Ra = \frac{\rho_w \alpha_w \Delta T g K l}{\phi \eta_w \kappa_w}, \tag{1.6}$$

where ρ_w is the density of water, α_w is the thermal expansivity of water, ΔT is the temperature difference across the change in depth, K is the permeability of the Martian regolith, l is the lengthscale, ϕ is the porosity of the regolith, η_w is the viscosity of the water, and κ_w is the thermal diffusivity of water (Hewitt et al., 2014).

Although most of these variables are approximately known, the permeability and porosity of the crust are very uncertain. Hanna and Phillips (2005) estimated the

vertical extent of potential Noachian aquifers by modeling the closure of pores in a manner resembling our approach. We approximate from their results, which derived a porosity that varied from 0.16 at the surface to 0.04 at a depth of ∼10 km. They predicted the permeability of Martian regolith to vary from 10^{-11} m^2 at the surface to 10^{-15} m^2 at depths of 5 km or more.

Taking an order of magnitude approach, we take $\rho_w = 10^3$ kg m^{-3}, $\alpha_w = 10^{-4}$ K^{-1}, $g = 4$ m s^{-2}, $\eta_w = 10^{-3}$ Pa s, and $\kappa_w = 10^{-7}$ m^2 s^{-1}. If we take a lengthscale of 10 km, then let us take $K = 10^{-14}$ m^2 as a rough geometric mean of permeability (weighted more towards 10^{-15} m^2 as half the depth has that permeability). Similarly, let us assume a mean porosity of 0.1. If the surface of Mars is near the freezing temperature, then we may take $\Delta T = 100$ K as an upper bound. The Rayleigh number is then ∼400. We do not expect any flow below a Rayleigh number of $4\pi^2$, and then some transition range above that (Hewitt et al., 2014). Depending on alterations in our order-of-magnitude assumptions, our simplified aquifer may be transitioning into convection. Since the effect of any such convection is to reduce the temperature gradient, our conductive solutions for the heat flux required to produce a particular porous layer depth (see below) will, if anything, be underestimates.

1.4 Application to InSight's Landing Site

InSight has detected a discontinuity in seismic wave velocity 8-11 km below the surface, which may indicate the presence of altered or fractured rocks to that depth

(Lognonné et al., 2020). We treat this as the transition from porous to compacted crust, but as a deeper probing of the Martian crust requires higher magnitude marsquakes, we cannot yet be sure if porosity actually continues to greater depths. Mineralogical changes can also cause seismic discontinuities, but the two transitions need not be independent: fluids fluxing through the permeable crust may cause diagenesis (Sun et al., 2019, e.g.) and a corresponding reduction in seismic velocities, while leaving the impermeable crust unchanged. In effect, the porous/compacted rock boundary can become a mineralogical boundary that is detectable by InSight. In any event, if a different depth of pore closure is ultimately detected, we can deduce the maximum heat flux experienced at the InSight landing site after pore generation.

In making our prediction for maximum heat flux experienced at the InSight landing site, we account for the uncertainty of each term in Equation 1.5 (see Appendix A). To account for a wide range of estimates of thermal conductivity of the Martian crust (with or without groundwater), we use separate thermal conductivities of $k = 1.5$, 2.0, and 3.0 W m^{-1} K^{-1}. We use an average present-day temperature of 235 K at the InSight landing site (Plesa et al., 2018). Solar luminosity in the early solar system was as little as 70% of its present value (Ribas, 2010). To account for this range, we use a surface temperature $T_S = 220 \pm 30$ K. We use a crustal density $\rho = 2950 \pm 250$ kg m^{-3}, and the rheological constants as listed in Section 1.2.1. For each rheology and thermal conductivity, we calculate the necessary heat flux (and its uncertainty) for pore closure as a function of pore-closure depth. We assume two extremes of crustal heat production: that of the present day (47$\pm$3 pW kg^{-1}) and what one might expect of

Mars in its earliest days (290±40 pW kg^{-1}) (Hahn et al., 2011; Plesa et al., 2018). Results are displayed in Figure 1.3.

As expected, higher heat fluxes, lower thermal conductivities or weaker rheologies result in thinner porous layers. For the same given temperature required to close pores at some depth, a higher crustal heat production will result in a higher surface heat flux. In turn, this heat flux can be related to a particular time in Martian history. For example, to close pores at a depth of 8-11 km requires heat fluxes in excess of 60 mW m^{-2} for a wet diabase rheology. For dry diabase, the heat fluxes are larger. A larger crustal heat production (as one would expect early in Mars' history) will result in a higher surface heat flux when pores closed, but the effect is not significant when closing pores at shallower depths. Based on the surface heat flux through time resulting from the thermal evolution model of Plesa et al. (2018) plotted in Figure 1.2a, we conclude that pore closure must have occurred before 4 Ga and that pore production must have been even earlier. This conclusion is robust to uncertainties in thermal conductivity, rheology, and crustal heat production (at least to close pores at ∼10 km depth). Because the employed thermal evolution model of Plesa et al. (2018) is an upper bound on likely heat fluxes, this age estimate is conservative and robust to uncertainties in Mars' initial conditions: other cases cool to a heat flux of 60 mW m^{-2} earlier in Mars' history.

Our constraint can be compared with thermal models and other measurements. For instance, Hauck and Phillips (2002)'s thermal model predicts a surface heat flux of up to ∼65 mW m^{-2} before 4 Ga, albeit for an average crustal thickness of 62 km. By

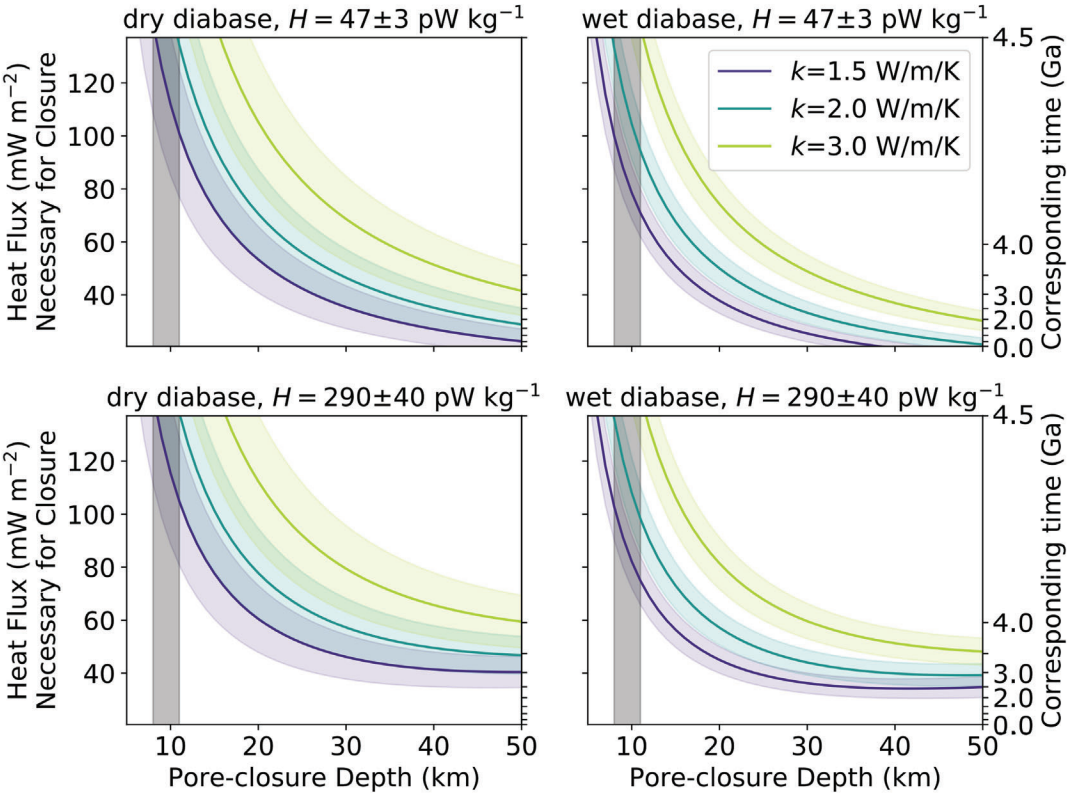

Figure 1.3: For each rheology and crustal heat production (H) combination, we vary the thermal conductivity to find the necessary surface heat flux needed to close pores viscously as a function of depth (Equation 1.5), assuming 10 Myr have elapsed to close pores. The secondary y-axis relates the necessary heat flux to the time that heat flux occurred at the InSight landing site according to case 110 of the Plesa et al. (2018) Mars thermal evolution model. The colored shaded regions highlight the corresponding uncertainty for each assumed thermal conductivity. Examining multiple thermal conductivities allows us to ascertain its effect on the maximum heat flux without needing to factor it into the calculation of uncertainty. The vertical grey shaded region highlights the 8-11 km depth at which InSight detects a discontinuity in seismic wave speed.

examining the viscous relaxation of craters, Karimi et al. (2016) were able to construct a map of Mars' surface heat flux during the Noachian, finding a heat flux ∼70 mW m^{-2} near where InSight landed. Both Hauck and Phillips (2002)'s thermal model and Karimi et al. (2016)'s inversion are consistent with heat fluxes exceeding 60 mW m^{-2} before 4 Ga. Another independent estimate of paleo heat fluxes may be derived from measurements of elastic thickness. For instance, McGovern et al. (2004) find heat fluxes in excess of 35, 43, 48 and 50 mW m^{-2} for four Noachian terrains. Likewise, Broquet and Wieczorek (2019) generally obtain heat fluxes greater than 50 mW m^{-2} for ancient, eroded volcanoes. Although uncertain, all these estimates are very consistent with our constraint.

1.5 Conclusion

This analysis assumes that the porous-to-non-porous transition is the cause of the seismic wave speed discontinuity detected by InSight (Lognonné et al., 2020). From that transition depth we conclude that pores formed prior to 4 Ga and in the presence of a heat flux exceeding 60 mW m^{-2}. If the seismic discontinuity instead marks a different transition of rock composition and porosity continues to a greater depth, this may indicate a delayed onset of pore-closure until later in Mars' history when it had cooled down. Alternatively, a Mars that had started off colder would also ensure a smaller heat flux, resulting in a deeper porous-to-compacted transition. Finally, if the crust has cooled significantly, additional layers of sediments or lavas could depress the

transition from porous-to-compacted crust without further closing pores due to the extra overburden pressure.

In the future, further seismic events will allow improved estimation of the depth at which pores close. When such a new measurement is made, the approach we present in this paper can be used to further clarify the thermal state of the ancient Martian crust.

1.6 Acknowledgements

We thank Adrien Broquet for his insightful comments on our manuscript. We also thank Walter Kiefer and an anonymous reviewer for their thoughtful and constructive comments. This is InSight contribution number 163. Parts of this work were supported by NASA grant 80NSSC18K1627 to FN. ACP gratefully acknowledges the financial support and endorsement from the DLR Management Board Young Research Group Leader Program and the Executive Board Member for Space Research and Technology. MAW was supported by the French Space Agency (CNES).

Data for the heat flux and temperature as a function of depth of the Martian crust were outputs of the Plesa et al. (2018) 3D Mars thermal evolution model at the InSight landing site. Data for several cases (the conditions of each are detailed in the Supplementary Material of Plesa et al., 2018) are archived in the Dryad repository (Gyalay et al., 2020b).

Chapter 2

Estimates for Tethys' Moment of Inertia, Heat Flux Distribution, and Interior Structure from its Long-Wavelength Topography

> Tethys, she was called, great nurse of the world's waters, born like her husband at the dawn of ages from Mother Earth herself. Her robes puddled blue at her feet, and around her neck was wrapped a water-serpent like a scarf. Before her was a golden loom that held her weaving. Her face was old but not withered. Countless daughters and sons had been birthed from her flowing womb, and their descendants were still brought to her for blessing. I myself had knelt to her once. She had touched my forehead with the tips of her soft fingers. *Welcome, child.*
>
> —*Circe*, by Madeline Miller

This chapter is a slightly modified reprint of work previously published as S. Gyalay and F. Nimmo (2023). "Estimates for Tethys' Moment of Inertia, Heat Flux Distribution, and Interior Structure from its Long-Wavelength Topography." *Journal of Geophysical*

Research: Planets 128(2), e2022JE007550. doi: 10.1029/2022JE007550

Key Points

- We can infer patterns of tidal heating from the long wavelength topography of an icy satellite.
- The tidal heating pattern can indicate a moon's internal structure.
- Tethys has no sub-surface ocean, but could have had a larger obliquity in the past.

Abstract

We examine if Saturn's moon Tethys may be an ocean world by assuming spatial variations in tidal heating are responsible for thickness or temperature variations in an isostatic ice shell, which manifests as surface topography. Because patterns of tidal heating depend on average ice shell thickness and whether the shell overlies a rigid or liquid layer, we can use Tethys' long-wavelength topography to infer its interior structure. We test a wide range of assumed parameters to hone in on the characteristics of Tethys that produce self-consistent and physically plausible interior models. To verify our technique, we apply it to Enceladus and recover the signature of a sub-surface global ocean with an appropriately thick ice shell and moment of inertia. Our best-fit Tethys models require Pratt isostasy and obliquity tides, with a normalized moment of inertia 0.340-0.345 and an average surface heat flux 1-2 mW m^{-2}. The best-fit basal heat flux

distribution indicates that Tethys does not have an ocean. The total power inferred (4-8 GW) to produce Tethys' shape from tidal heating indicates either a highly dissipative interior or an obliquity higher than previously estimated. The topography may also be a relic of a warmer past when the obliquity was higher.

Plain Language Summary

Oceans have been discovered beneath the surfaces of many icy moons, the most famous among them Europa and Enceladus. We examine if Tethys, a moon of Saturn's, may also have a sub-surface ocean. We cannot answer this question using the techniques employed at other worlds, as those required close flybys of spacecraft. However, the movement of Tethys within Saturn's gravity field causes tidal heating in Tethys' interior. The exact spatial distribution of tidal heating can then indicate if there is a liquid or rigid layer beneath Tethys' ice shell, as well as how thick this ice shell is. This tidal heating can be inferred from the large scale topography (essentially, the shape) of Tethys. We iterate through assumed values for a series of parameters to find a scenario that best explains Tethys' interior, finding it does not have an interior ocean. However, the amount of tidal heating we infer indicates that Tethys should have a higher tilt relative to its orbit than is currently predicted. Given how long heat takes to conduct through ice, we may be seeing the effect of a high tilt from a billion years ago.

2.1 Introduction

The presence of a global ocean underneath an icy moon's shell has profound geophysical and astrobiological implications. Discoveries of these oceans have typically relied on close flybys, using libration, gravity data, or magnetic induction (Nimmo and Pappalardo, 2016). We focus on one of Saturn's moons without the luxury of these data: Tethys. We argue that not only does the long-wavelength topography of this moon imply moderate tidal heating, but that it can be used to infer Tethys' moment of inertia, heat flux distribution, and internal structure (namely the presence or lack of an ocean). After a brief background (Section 2.2), we outline the general methodology by which we probe the interior of Tethys without gravity data (Section 2.3). We then walk through an example of the methodology (Section 2.4) before presenting our full set of results (Section 3.3) and discussing them (Section 2.6). The supplementary material details our methodology and its limitations. Additionally, the supplement presents an application to Enceladus, benchmarking the method on a satellite with a better-constrained interior.

2.2 Background

Tethys is one of Saturn's mid-sized icy satellites and has a low bulk density of 984 kg m^{-3} (Roatsch et al., 2009), very close to that of water ice—implying a very low amount of radionuclide-bearing rocks within Tethys as a potential heat source. However, the satellite features terrain that hints at a more active past such as Ithaca Chasma, a 1000 km long flexural crack (Smith et al., 1981; Giese et al., 2007). Another striking

feature is Odysseus crater, one of the largest craters in proportion to its body's surface area (Moore et al., 2004).

In this paper, we seek to assess the present thermal state and tidal heating distribution of Tethys from its shape. Over the course of the Cassini orbiter mission at Saturn, the long-wavelength topography of Tethys was characterized using limb profiles (Thomas, 2010; Nimmo et al., 2011). Because these moons are nearly spheres, we use the language of spherical harmonics to perform calculations and derive results. We can express some function f (e.g. topography or heat flux) that varies across a sphere's colatitude θ and longitude λ as the sum of weighted spherical harmonics of degree l and order m:

$$f(\theta,\lambda) = \sum_{l=2}^{\infty} \sum_{m=0}^{l} (C_{l,m} \cos m\lambda + S_{l,m} \sin m\lambda) P_{l,m}(\cos\theta), \tag{2.1}$$

where $P_{l,m}(\cos\theta)$ is an associated Legendre function (Blakely, 1995). $C_{l,m}$ and $S_{l,m}$ are coefficients determined by integration. We also refer to normalized coefficients $\bar{C}_{l,m}$ that are related by $C_{l,m} = \bar{C}_{l,m}\sqrt{(2-\delta_0^m)(2l+1)(l-m)!/(l+m)!}$, where δ_0^m is the Kronecker delta.

When comparing the relative power of topography per degree l of Tethys (Nimmo et al., 2011), we find that while degree 2 dominates Tethys' shape, degree 4 has much more power than degree 3 (Figure 2.1). Much of the degree 2 shape arises from the rotational flattening and the tidal stretching of the moon (Beuthe et al., 2016). However, the degree 4 shape may be indicative of strong tidal heating at Tethys. The spatial variations of tidal heating act at degrees 2 and 4 (Beuthe, 2013), and can give rise to topographic variation (e.g. Nimmo et al., 2007). Topography in higher degrees,

meanwhile, may be due to the large amount of cratering upon Tethys. The largest crater, Odysseus, is clearly visible in the spherical harmonic topography at degree 7 (Nimmo et al., 2011) but does not contribute significantly at degree 4 (Figure 2.1). More uncertain is the source of topography in odd orders of degree 4, which dominate the degree 4 signal but would not be caused by variations in tidal heating. Fortunately, the results we obtained are quite insensitive to the degree 4 values used (see Section 2.4 below).

At Enceladus, strong tidal heating can sustain a sub-surface water ocean, so we examine if Tethys might also possess such an ocean. Unlike Enceladus, Tethys has not been privileged with gravitational flybys to characterize the interior structure, so we developed a new method to infer the interior as described below. Tethys remains a compelling world to search for an ocean, given their increasing ubiquity underneath the shells of the outer planets' icy moons, and for the aforementioned evidence of past activity.

2.3 Methodology

With our model, we ultimately infer the tidal heating distribution of a moon from its topography based on an assumption of isostasy. This pattern in turn indicates whether there is a solid or liquid boundary beneath the ice shell. In deriving the tidal heating pattern, we test multiple moments of inertia, ice shell thicknesses, and different forms of isostasy and tides to see which combination fits best.

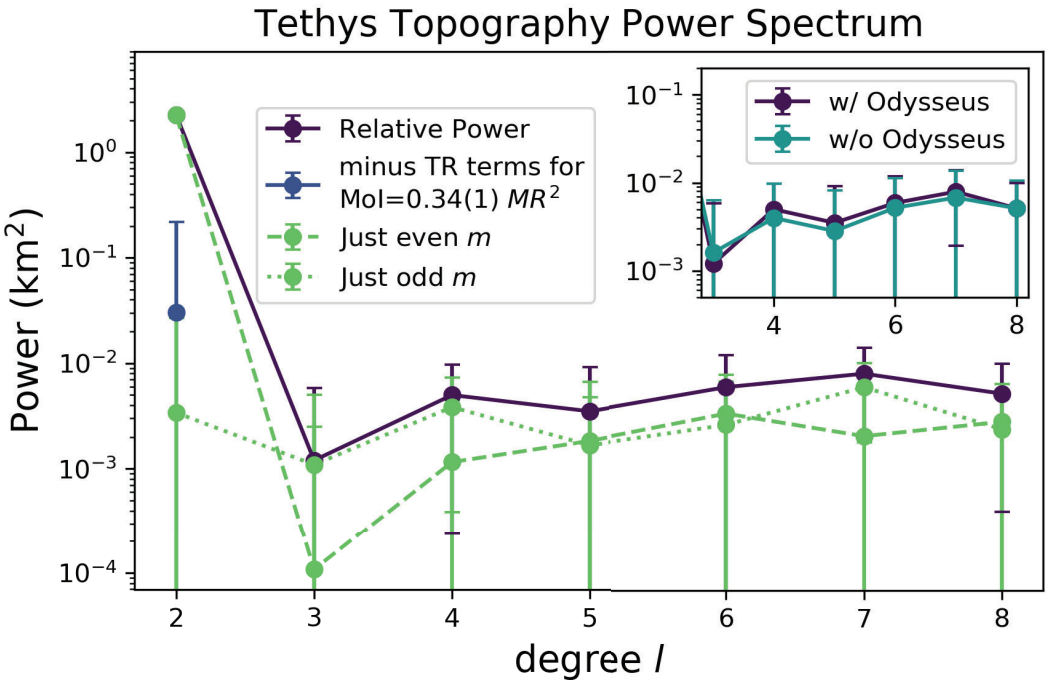

Figure 2.1: For each spherical harmonic degree l, we calculate the relative power of observed topography. This is the sum of the squares of the spherical harmonic coefficients (Nimmo et al., 2011) of each order m within that degree (note that Nimmo et al. (2011) imposed an *a priori* constraint when deriving the harmonic coefficients). To normalize power for the number of orders per degree, we divide by $2l+1$. We decompose the power from even and odd orders m as dashed and dotted lines, respectively. As Nimmo et al. (2011) computed the spherical harmonic coefficients of topography from limb profiles, we compare the power spectrum using topography coefficients calculated with and without profiles that pass over Tethys' largest crater, Odysseus, in an inset plot, to show how little it varies with Odysseus. In addition, we plot the power of observed topography less topography due to tidal and rotational stretching of a hydrostatic body with a normalized moment of inertia 0.34±0.01. We include propagation of individual coefficient uncertainties in both cases. In the case subtracting the hydrostatic shape, error in degree 2 is dominated by error of observed topography and is simply exaggerated by the log scale.

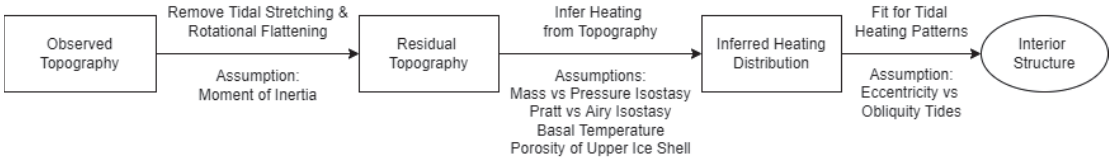

Figure 2.2: Simplified flowchart of the methodology that we apply, highlighting some of the key parameters we assume and vary in each model.

Figure 2.2 displays a flow chart of the methodology we employ in inferring the interior structure of a moon from its topography. We begin by calculating the shape of the moon due to tidal and rotational forces, which often accounts for a significant portion of the world's long-wavelength topography (Section 2.3.1). After we remove this contribution, we are left with a residual topography that we assume is primarily due to variations in tidal heating at these long wavelengths, causing variations in either shell thickness or density (Section 2.3.2). Finally, we infer tidal heating patterns from the residual topography, and thus the moon's internal structure—including whether or not it possesses a subsurface global ocean (Section 2.3.3). We verify *a posteriori* that our model is physically plausible by building a density profile from its inferred structure and moment of inertia.

As spatial variations of tidal heating depend only on cosine terms of even degrees $l \leq 4$ and positive even orders m (Beuthe, 2013), we focus on topography $h(\theta, \lambda)$ spherical harmonic coefficients $C^h_{l,m}$ for even $l \leq 4$, $0 \leq$ even $m \leq l$. We utilize the long-wavelength topographies of Saturnian satellites in Nimmo et al. (2011).

2.3.1 Effect of tidal and rotational potential on shape

In addition to tidal heating, the degree 2 topography of icy satellites is likely dominated by contributions from tidal and rotational forces. Thus to determine spatial variations in tidal heating from topography we must first remove these other contributions. The tidal contribution we remove is the time-averaged physical distortion of the moon by Saturn along the Saturn-moon axis (not to be confused with the resultant tidal heating), while the rotational contribution is a result of the flattening that occurs when a sphere spins. For a sufficiently distant satellite these contributions are only in degree $l = 2$. In addition to the angular rotation rate ω, the bulk density of the body $\bar{\rho}$ and its Love number h_2 are needed to ascertain the tidal and rotational contribution to its shape. Assuming the body is hydrostatic, we use the Darwin-Radau relationship (e.g. Munk and MacDonald, 1960) to find the Love number h_2 from the body's mean moment of inertia C:

$$h_2 = \frac{5}{1 + \left[\frac{5}{2}\left(1 - \frac{3}{2}\frac{C}{MR_0^2}\right)\right]^2}, \tag{2.2}$$

where M is the mass of the body, and R_0 its average radius. For a synchronous satellite the contribution of tidal and rotational forces to a body's topography is

$$C_{2,0}^{tr} = -\frac{5}{6}h_2 R_0 q\left(1 + \frac{76}{105}h_2 q\right) \tag{2.3}$$

$$C_{2,2}^{tr} = \frac{1}{4}h_2 R_0 q\left(1 + \frac{44}{21}h_2 q\right), \tag{2.4}$$

where $q = \frac{\omega^2 R_0^3}{GM}$, as according to Beuthe et al. (2016). These equations include second-order corrections for rapidly rotating satellites. There should likewise be small degree-4 contributions to the satellite's shape from tidal and rotational terms, but as the degree-4

terms are small to begin with, deriving these contributions is outside the scope of the paper.

As Tethys' moment of inertia is unknown, we must vary its assumed value in fitting for Tethys' heating distribution. A limiting case is that for a homogeneous body of incompressible material, $C = 0.4MR_0^2$. If a body undergoes differentiation, its moment of inertia is lower as denser material sinks to the center. Using Voyager data on Tethys' shape, Thomas and Dermott (1991) concluded that Tethys' normalized moment of inertia was between 0.17 and 0.35. Repeating their methodology (detailed in the supporting information, Appendix B) with updated parameters from Cassini (Nimmo et al., 2011), we find Tethys' normalized moment of inertia must lie between 0.34 and 0.37. However, Thomas and Dermott (1991)'s method used first-order relations to solve for the expected moment of inertia while we use second-order theory of figures to account for the moment of inertia in our model. Furthermore, Thomas and Dermott (1991) did not investigate the effect that tidal heating variations might have on the degree-2 shape of Tethys, which is the focus of our work. For these reasons, we constrain the normalized moment of inertia $\frac{C}{MR_0^2}$ to vary $0.3 \leq \frac{C}{MR_0^2} \leq 0.4$.

2.3.2 Inferring Tidal Heating from Topography

Once the contribution of tidal/rotational forces to topography is removed, we are left with residual topography. Tethys has strong topography in degrees l=2, 4 (Figure 2.1). As tidal heating only varies in those degrees, we can assume that a significant portion of the residual topography is the result of spatial variations in

tidal heating. Lateral differences in heating would manifest as variations in either shell thickness or density. Assuming isostasy, the mass or pressure at depth will be constant in spite of variations in either quantity. The assumption of isostasy is likely to hold because even at low temperatures, the viscosity of ice is small compared to that of rock (e.g. $\sim 3 \times 10^{17}$ Pa s at 200 K), and thus the timescale for the shell to relax to isostasy (e.g. Melosh, 1989) is much faster than the other timescales of interest. Below we give an overview of our approach. First, however, we discuss two potential complicating factors: craters and lithospheric flexure.

Tethys' largest crater, Odysseus, is 400 km rim-to-rim (Moore et al., 2004) or 12% of Tethys' circumference. This is not insignificant when compared to the lengthscale of degree 4 features and thus has the potential to make a major impression on the degree 4 spherical harmonic coefficients of topography. To examine if Odysseus crater may have a significant impact upon our result, we compare the power spectrum of spherical harmonic coefficients of topography derived from all limb profiles of Tethys used in Nimmo et al. (2011), as well as derived from all limb profiles excluding those that pass through Odysseus (Figure 2.1). We find no significant differences between these two approaches.

In the rest of this manuscript we assume the bulk of residual long-wavelength topography is due to isostasy, but a potentially complicating factor is the role of any elastic lithosphere. Because of Tethys' small radius, even a thin intact lithosphere can have important effects. Assuming the elastic thickness of Tethys' upper crust from Giese et al. (2007), Tethys is not expected to be fully compensated even at $l = 2$,

using the equations of Turcotte et al. (1981). If, however, the lithosphere is fractured (as is certainly the case around Ithaca Chasma), then spherical membrane stresses will not be available to support topography and a higher degree of compensation is expected. Furthermore, since we envisage variations in shell thickness as producing bottom loads, any elastic strength will reduce the surface topography for a given shell thickness contrast. As a result, the heat fluxes we estimate below would be lower bounds in the case that elastic strength was important. With these caveats in mind, we now proceed with our isostatic analysis.

Once we are satisfied that there are no other major contributions to even orders of degree 2 and 4 topography, we may begin to use the residual topography to infer spatial variations in tidal heating. The strongest tidal heating is at the base of the ice shell because either tidal dissipation is strongest for warm, low-viscosity ice at the base of a shell overlying an ocean or because of shear heating due to the no-slip boundary with the more rigid, rocky interior beneath. In either case, we approximate tidal heating as a basal heat flux beneath the moon's ice shell. Endogenic radionuclide heating can also add a constant background heat flux. Although we assume for our analysis that the residual shape is due to present-day tidal heating, it is important to consider the conduction timescale of ice. The thermal conduction timescale goes as d^2/κ, where d is the ice shell thickness and κ the thermal diffusivity. Depending on the ice shell thickness, this timescale could vary from tens of Myr to a Gyr. This timescale will determine how long lateral temperature variations or lateral shell thickness variations can persist, unless the latter are first removed by viscous flow. It is thus important

to remember that the present-day shape we use in our analysis may have arisen from conditions occurring hundreds of Myr ago. We return to this issue in Section 2.6 below.

We invoke isostasy to infer tidal heating from residual topography. Historically, isostasy has assumed that there is a constant mass at the base of equal columns penetrating a planetary body. This is adequate for worlds with thin crusts, as one can approximate such a crust as a plane locally. For thicker crusts, the spherical geometry may become important. Some solve this by assuming that the pressure at depth is constant (Hemingway and Masuyama, 2017), while others argue that one must minimize deviatoric elastic stresses within the ice shell itself (Beuthe, 2021). Minimum-stress isostasy can be approximated by equal-weight isostasy, which will fall between the results expected for equal-pressure and equal-mass isostasy. To cover the full breadth of possibilities, we test for both equal-mass and equal-pressure isostasies as endmember cases. Additionally, we need to assume whether Tethys' ice shell is acting under Airy or Pratt isostasy (Figure 2.3). The important difference is that these two processes depend in an opposite way on heat flux variations: in Airy isostasy the shell thins beneath higher heat-flux areas, so high heat flux correlates with low topography; while if the shell thickness remains relatively constant under Pratt isostasy, higher heat fluxes result in a warmer, less dense ice shell and thus higher topography. Either of these two processes can operate, depending on the tendency of lateral flow to even out shell thickness variations. Airy isostasy presumes the existence of a subsurface ocean, while Pratt isostasy does not require one.

In both cases, we determine variations in basal heat flux from changes in shell

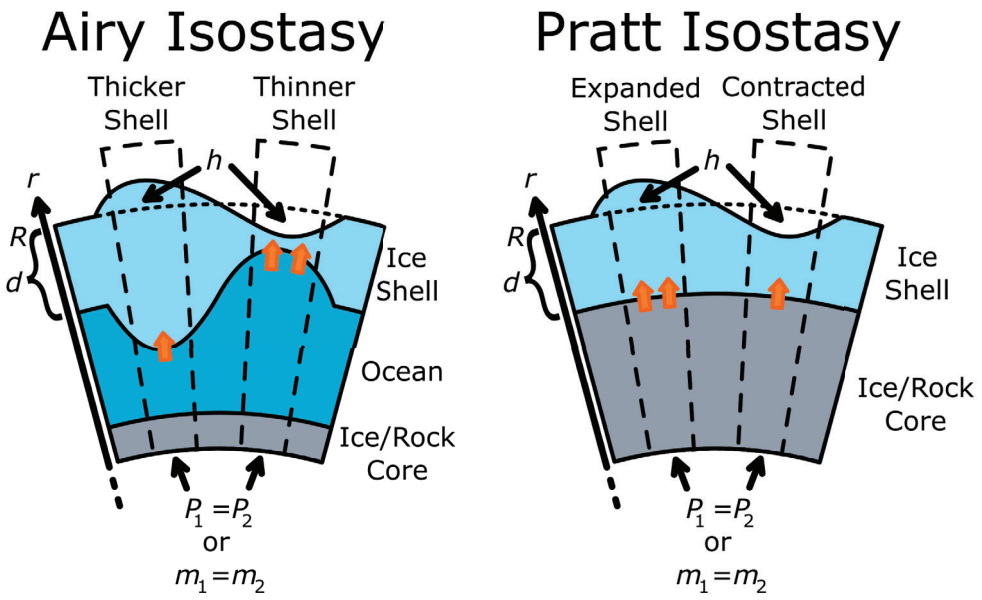

Figure 2.3: Schematic highlighting the differences between Airy and Pratt isostasy. In both cases, columns penetrating the moon must maintain a constant pressure or mass at depth, despite a topographic variation h about the average radius R of the moon. In Airy isostasy, the constant-density ice shell thickness d varies and is compensated by an isothermal ocean below. In Pratt isostasy, the ice-shell varies in thickness due to a change in the density of the ice from thermal expansion and contraction. Thus for the same topographic variation h, the two cases imply opposing basal heat flux variations (marked by more or less orange arrows) assuming all other conditions are equal.

thickness under a spherical geometry. Changes in shell thickness are relative to the average shell thickness, which is calculated from a spherical-geometry form of Fourier's law and assumes an average surface temperature and average basal heat flux. We use a temperature-dependent thermal conductivity of solid ice from Klinger (1980), and the thermal conductivity of porous ice is calculated according to Shoshany et al. (2002). From the residual topography and surface temperatures calculated according to Nadeau and McGehee (2017) assuming satellite albedoes of Howett et al. (2010), we can then calculate the variations in basal heat flux required to explain the observed topography.

2.3.2.1 Fourier's Law

Fourier's law relates a heat flux and temperature gradient across a material interface to the material's thermal conductivity k. This thermal conductivity depends on the temperature of the ice T as $k = k_0/T$ (Klinger, 1980). Then one can determine the heat flux F_b at the base of an ice shell with thickness d on a moon with average radius R_0, surface temperature T_S, and basal temperature T_B as

$$F_b = \frac{-k_0 \ln T_S/T_B}{d(1 - \frac{d}{R_0})}. \tag{2.5}$$

We derive this formula in the supporting material (Appendix B). In the limit of a thin shell ($d \ll R_0$) and constant thermal conductivity, Equation 2.5 reduces to the flat-plane approximation, $F_b = -k(T_S - T_B)/d$.

To account for the possibility of surface porosity, we imagine a two layer system with an upper porous ice shell and a lower solid ice shell, separated by some annealing temperature T_A under the assumption that porosity only persists at temperatures less

than a particular value, here taken to be 140 K (Besserer et al., 2013). While lateral variations in porosity may occur (cf. Besserer et al., 2013), we make the simplifying assumption that the upper layer has a constant porosity and thickness to assess its impact upon our Tethys models in an order of magnitude sense. To account for lateral variations in porosity in our models would require solution of the time-dependent evolution of temperature and thermal conductivity—increasing the computational complexity—and is thus outside the scope of this paper. Furthermore, a laterally-varying porous layer thickness would yield the same behavior as shell thickness variations, and is thus approximately described by our Airy isostasy analysis (see below).

Porous ice has a temperature-dependent thermal conductivity k_p calculated according to Shoshany et al. (2002) as a function of porosity ϕ. We define a constant $k_{0,p} = k_p T$ such that the thermal conductivity of porous ice k_p depends on temperature as the thermal conductivity of solid ice did. As derived in the supporting material (Appendix B), Fourier's law for a two-layer spherical shell (where the upper layer is porous) of temperature- and porosity-dependent thermal conductivity is then

$$F_b = \frac{-k_0 \ln(T_A/T_B) - k_{0,p} \ln(T_S/T_A)}{(R_0 - d)(1 - \frac{R_0 - d}{R_0})}, \tag{2.6}$$

where d is still the total ice shell thickness. Equation 2.6 reduces to Equation 2.5 when porosity $\phi = 0$.

2.3.2.2 Airy Isostasy

Under Airy isostasy, changes in topography are due to the thinning or thickening of the ice shell (Fig. 3). A low in topography is caused by a thinner ice shell

which is compensated below by a subsurface ocean. Assuming an isothermal ocean, a thinner ice shell necessitates higher basal heat flux (again, a proxy for tidal heating) under Fourier's law (Equation 2.6).

Assuming equal-pressure isostasy for an ice shell with crustal density ρ_C (a volume-weighted average in the case of a porous upper layer and solid lower layer) that is $\Delta\rho$ less than the density of the ocean, we find a basal topography h_b as a function of the corresponding surface topography h (measured as the difference from an average radius R_0; e.g. (Hemingway and Masuyama, 2017)):

$$h_b = -h\frac{\rho_C}{\Delta\rho}\left(\frac{g_S}{g_B}\right), \tag{2.7}$$

where g_S is the surface gravity and g_B gravity at the base of the ice shell. $\frac{g_S}{g_B}$ can be calculated

$$\frac{g_S}{g_B} = \frac{\left(\frac{R-d_0}{R}\right)^2}{1+\left[\left(\frac{R_0-d_0}{R_0}\right)^3 - 1\right]\frac{\rho_C}{\bar{\rho}}}. \tag{2.8}$$

As the change in ice shell thickness under Airy isostasy from average thickness d_0 is $\Delta d = h - h_b$, and h_b is proportional to topography h (equation 2.7), we can directly find Δd as a function of h:

$$\Delta d = h\left(1 + \frac{\rho_C}{\Delta\rho}\frac{g_S}{g_B}\right). \tag{2.9}$$

Under equal-mass isostasy, we need only account for the difference in volume due to a change in topography:

$$\Delta d = h\left[1 + \frac{\rho_C}{\Delta\rho}\left(\frac{R_0}{R_0 - d_0}\right)^2\right]. \tag{2.10}$$

Finally, using Equation 2.6 we can find the local heat flux variation ΔF from the background value F_0 given the variation in shell thickness Δd (itself directly related to

the variation in residual topography) and surface temperature. That is,

$$\Delta F = \frac{-k_0 \ln(T_A/T_B) - k_{0,p} \ln(T_S/T_A)}{[R_0 - (d_0 + \Delta d)]\left[1 - \frac{R_0 - (d_0 + \Delta d)}{R_0}\right]} - F_0. \tag{2.11}$$

2.3.2.3 Pratt Isostasy

Under Pratt isostasy, changes in topography are due to the thermal expansion and contraction of the ice shell, using a thermal expansivity of ice from Röttger et al. (1994). So in contrast to Airy isostasy, lower basal heat fluxes are necessary for topographic lows. We expect that if there is a sub-surface ocean, Airy isostasy will dominate. Thus, if we find Tethys experiences Pratt isostasy, it is less likely there will be a sub-surface ocean. We do, however, assume both an ocean-bearing and an ocean-absent case in the consistency checks for our results.

Assuming an average shell thickness d_0 determined with Equation 2.6, the change in crustal density $\delta\rho$ from ρ_C that is responsible for a topography h when operating under equal-pressure isostasy is

$$\delta\rho \simeq \frac{-\rho_C h}{\frac{g_B}{g_S}(R_0 - d_0) - R_0 + \frac{2\pi G}{g_S}\rho_C[R_0^2 - (R_0 - d_0)^2]} \tag{2.12}$$

(derived in the supporting material, Appendix B). In the limit of a thin shell this expression simplifies to $\delta\rho = -\rho_C \frac{h}{d_0}$, the usual Cartesian case.

Once we have the change in density for a given topography, we can relate this to the change in volume due to thermal expansivity:

$$\frac{\Delta V}{V} = \frac{-\delta\rho}{\rho_C + \delta\rho} = \alpha_0 \Delta\bar{T} \tag{2.13}$$

where α_0 is the thermal expansivity of water ice for the reference average temperature of the ice shell $\bar{T}_0$, $\Delta\bar{T} = \bar{T}_0 - \bar{T}$, and $\bar{T} = \frac{1}{2}(T_S + T_B)$. In equal-mass isostasy, we can skip calculating the change in density, as the change in volume of some equal mass is purely due to the additional topography. That is,

$$\frac{\Delta V}{V} = \frac{(R_0 + h)^3 - R_0^3}{R_0^3 - (R_0 - d_0)^3} \tag{2.14}$$

Following from Fourier's law (Equation 2.5) and again neglecting internal heat sources,

$$T_B = T_S e^{Fd(1-d/R)/k_0}. \tag{2.15}$$

Then for a situation in which the conductivity is temperature-dependent the mean temperature variation $\Delta\bar{T}$ is given by

$$\Delta\bar{T} = \frac{1}{2}\left\{\Delta T_S + T_{B,0}\left[\frac{T_S}{T_{S,0}} e^{\Delta F d(1-d/R)/k_0} - 1\right]\right\} \tag{2.16}$$

where ΔT_S is the variation in surface temperature T_S from the reference value $T_{S,0}$ and ΔF is the variation in basal heat flux F from the reference value F_0. This equation makes it clear that the variation in mean temperature can arise either from variations in basal heat flux (second term on right hand side) or surface temperature variations (both terms). We let d stay constant at the average ice shell thickness d_0 for ease of derivation.

By combining thermal expansivity (Equation 2.16) with Fourier's law (Equation 2.5) we may derive (in detail in the supporting material, Appendix B) the change in basal heat flux implied by topography due to Pratt isostasy as:

$$\Delta F = \frac{k_0}{d_0(1 - d_0/R_0)} \ln\left(\frac{T_{S,0}}{T_S}\left\{1 + \frac{1}{T_{B,0}}\left[\frac{2}{\alpha_0}\frac{(-\delta\rho)}{\rho_C + \delta\rho} - \Delta T_S\right]\right\}\right), \tag{2.17}$$

where $\delta\rho$ is calculated in Equation 2.12 when assuming equal-pressure isostasy. Under equal-mass isotasy, we substitute $\frac{-\delta\rho}{\rho_C+\delta\rho}$ in Equation 2.17 with $\frac{\Delta V}{V}$, calculated using equation 2.14. We account for a porous layer with modifications to this formula in the supporting material (Appendix B).

2.3.3 Interior Structure from Tidal Heating

Beuthe (2013) demonstrated that one could compose tidal heating patterns as the linear combination of three angular basis functions A, B, and C. These basis functions are themselves linear combinations of spherical harmonic functions of even degrees $l \leq 4$. The basis set of angular functions ψ_J are:

$$\psi_A = \psi_0 + \psi_2 + \psi_4 \tag{2.18}$$

$$\psi_B = \psi_0 + \frac{1}{2}\psi_2 - \frac{2}{3}\psi_4 \tag{2.19}$$

$$\psi_C = \psi_0 - \psi_2 + \frac{1}{6}\psi_4, \tag{2.20}$$

where

$$\psi_l = \sum_{m=0}^{l} P_{l,m}(\cos\theta) a_{l,m} \cos m\lambda. \tag{2.21}$$

Note that $\psi_0 = a_{0,0}$. Then given a spatially-averaged heat flux due to tidal heating $F_{0,T}$, we find the heat flux due to tidal dissipation F_T:

$$F_T(\theta,\lambda) = \frac{F_{0,T}}{\psi_0}(\chi_A\psi_A + \chi_B\psi_B + \chi_C\psi_C), \tag{2.22}$$

where χ_J are weights of each basis angular function. Each weight ranges from 0 to 1, and the sum of all three is 1. $a_{l,m}$ for each harmonic function vary depending on the type of tide as shown in Table 2.1, and affects the pattern functions.

Table 2.1: Tidal dissipation harmonic function coefficients for eccentricity e and obliquity θ_0

	$a_{0,0}$	$a_{2,0}$	$a_{2,2}$	$a_{4,0}$	$a_{4,2}$	$a_{4,4}$
Eccentricity tides ($\times e^2$)	21/5	-33/7	9/14	387/140	-27/140	-3/160
Obliquity tides ($\times \sin^2\theta_0$)	3/5	3/7	3/14	-36/35	3/35	0

Note: Values from Beuthe (2013).

As the tidal heating is a linear combination of these basis functions, we perform a multilinear regression on the spherical harmonic coefficients of heat flux $C^F_{l,m}$ to solve for the A, B, and C function weights. (Recall that the heat flux coefficients are in turn inferred from the measured topography via equation 2.11 or 2.17). A high B function weight generally indicates a rigid interior, while a high C function weight generally indicates a subsurface global ocean or a homogenous body (Figure 2.4). Exact A, B, and C function weights can also be used to infer the thickness of the ice shell for comparison with the assumed ice shell thickness.

For this multi-linear regression (explained in detail in the supporting material, Appendix B), we calculate a goodness-of-fit value known as the coefficient of determination R^2. The closer R^2 is to the maximum of 1, the more accurately the basis heating pattern weights fit the inferred basal heat flux distribution. Thus, a high R^2 implies our inferred heating pattern is indeed due to tidal heating.

Another goodness-of-fit metric that we employ is the Root Mean Square (RMS) difference of observed and forward-modeled topography (more detail in the supporting material, Appendix B). We calculate the forward modeled topography h_{fwd} for each $0.1^\circ \times 0.1^\circ$ latitude-longitude bin. For each bin i we have its angular area $\Omega_i = \sin(\theta_i)\Delta\theta\Delta\phi$, the forward modeled topography $h_{\text{fwd},i}$, and the observed topography

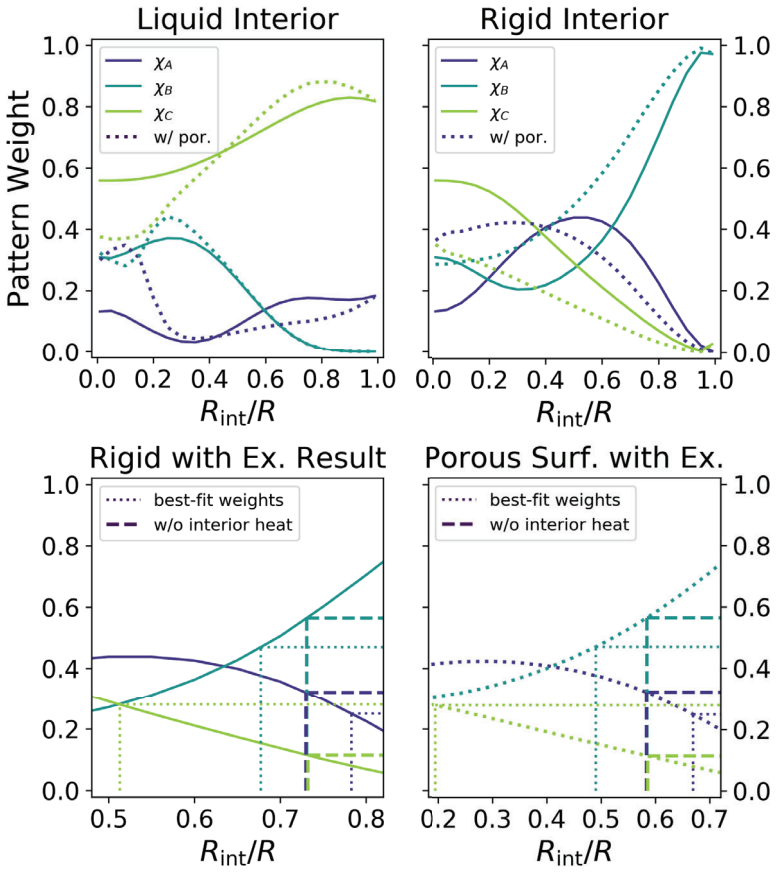

Figure 2.4: We use the solid body tidal heating code of Roberts and Nimmo (2008) to model tidal heating within Tethys. In the upper plots, solid lines indicate a two-layer Tethys consisting of an ice shell over a liquid (left) or rigid (right) interior. We assume a solid ice density of 940 kg m^{-3}, and calculate interior density from Tethys' remaining mass. We vary the radius of the interior R_{int} relative to the total radius of Tethys R, and calculate the proportion of each tidal heating weight (solid lines). These are indistinguishable from Beuthe (2013)'s results for a satellite of uniform density. Thick dotted lines assume an upper ice shell with porosity $\phi = 0.3$, with lower rigidity and higher viscosity than solid ice. Porous layer thickness assumed porosity closed at 140 K and the base of the solid ice shell was 270 K. On the lower left plot, we zoom in on the rigid interior case and overlay where the best-fit heating pattern weights from our example of the methodology (Section 2.4) intersect these patterns as a function of the interior's radius (dotted lines). After eliminating the uniform heating term suspected from radiogenic heating in the ice-rock core, the core radius for each heating term would barely changes. However, the removal of suspected interior core heating allows the radius to converge (dashed lines). This is repeated for models that include an upper porous shell in the lower right.

$h_{\mathrm{obs},i}$. The weighted RMS is then:

$$\mathrm{RMS} = \sqrt{\frac{\sum_i \Omega_i (h_{\mathrm{fwd},i} - h_{\mathrm{obs},i})^2}{\sum_i \Omega_i}}. \tag{2.23}$$

We can thus explore the parameter space of moment of inertia, ice shell thickness, upper ice shell porosity, isostasy type, and tide type. After we confirm a given model is physically possible (e.g. constraints of ice shell thickness and moment of inertia imply an ice density that is similar to what we expect; see the supporting material, Appendix B), the models with the highest R^2 and lowest RMS are most likely to accurately describe the circumstances necessary for Tethys' shape.

One must be careful however, to discern between patterns of heat generated by tidal heating or by other sources. For instance, we expect that radiogenic heat within the interior of Tethys would produce a uniform heating pattern ($\chi_A = 0.2$, $\chi_B = 0.4$, $\chi_C = 0.4$). We can compose some function of the total heat flux as a sum of the uniform, endogenic heat flux F_D and the spatially-varying tidal heat flux F_T:

$$F(\theta, \lambda) = F_D(\theta, \lambda) + F_T(\theta, \lambda). \tag{2.24}$$

Each flux term in Equation 2.24 can be written in the form of Equation 2.22, or

$$\frac{F_0}{\psi_0} \begin{bmatrix} \chi_A \\ \chi_B \\ \chi_C \end{bmatrix} \cdot \begin{bmatrix} \psi_A \\ \psi_B \\ \psi_C \end{bmatrix} = \frac{F_{0,D}}{\psi_0} \begin{bmatrix} 0.2 \\ 0.4 \\ 0.4 \end{bmatrix} \cdot \begin{bmatrix} \psi_A \\ \psi_B \\ \psi_C \end{bmatrix} + \frac{F_{0,T}}{\psi_0} \begin{bmatrix} \chi_{A,T} \\ \chi_{B,T} \\ \chi_{C,T} \end{bmatrix} \cdot \begin{bmatrix} \psi_A \\ \psi_B \\ \psi_C \end{bmatrix}, \tag{2.25}$$

where the $\chi_{A-C,T}$ denote the heating pattern weights specifically for tidal heating.

Let the averages of each component be

$$F_{0,T} = \chi_T F_0 \tag{2.26}$$

$$F_{0,D} = \chi_D F_0, \tag{2.27}$$

where $\chi_T + \chi_D = 1$ and represent fractions of the basal flux that are the tidal and direct, uniform components, respectively. After performing the appropriate substitutions and dropping like-terms in Equation 2.25, we find,

$$\begin{bmatrix} \chi_A \\ \chi_B \\ \chi_C \end{bmatrix} = \chi_D \begin{bmatrix} 0.2 \\ 0.4 \\ 0.4 \end{bmatrix} + \chi_T \begin{bmatrix} \chi_{A,T} \\ \chi_{B,T} \\ \chi_{C,T} \end{bmatrix}. \tag{2.28}$$

For some given endogenic heating as a fraction of total heating χ_D and recalling that $\chi_D + \chi_T = 1$, we can remove the uniform heating component from the total tidal heating to find only the *tidal* heating pattern weights:

$$\begin{bmatrix} \chi_{A,T} \\ \chi_{B,T} \\ \chi_{C,T} \end{bmatrix} = \frac{1}{\chi_T} \begin{bmatrix} \chi_A \\ \chi_B \\ \chi_C \end{bmatrix} - \frac{\chi_D}{\chi_T} \begin{bmatrix} 0.2 \\ 0.4 \\ 0.4 \end{bmatrix}. \tag{2.29}$$

To make use of this equation, we must estimate the radiogenic fraction. From moment of inertia and ice shell thickness and densities, we may solve for the mass of rock within our moon's interior. Assuming a rock density of 2710 kg m^{-3} (e.g. Roberts, 2015) and applying a chondritic rock radioactivity of $\sim 3.5 \times 10^{-12}$ W kg^{-1} (e.g. Turcotte and Schubert, 2014), we solve for the endogenic heat production—which we may then directly compare to the total heat production of our model (determined from ice shell thickness, upper shell porosity, and basal temperature).

Table 2.2: Assumed parameters for Tethys and its orbit.

Parameter		Value
Radius	R_0	531.1 km (Roatsch et al., 2009)
Angular Rotation Rate	ω	3.85×10^{-5} rad s^{-1} (JPL 2020 Satellite Ephemerides)
Bulk Density	$\bar{\rho}$	984 kg m^{-3} (Roatsch et al., 2009)
Average Surface Temperature*	$T_{S,0}$	68.25 K
Bolometric Bond Albedo	A_{BB}	0.67 (Howett et al., 2010)
Solar Luminosity	L_{Sun}	3.828×10^{26} W (IAU Working Group, 2015)
Solar Distance	a	1.429×10^{12} m
Saturn Obliquity	i	0.466 rad
Solid Ice Density	ρ_{ice}	940 kg m^{-3}
Thermal Conductivity Constant	k_0	567 W m^{-1} (Klinger, 1980)
Annealing Temperature	T_A	140 K (Besserer et al., 2013)
Tethys Eccentricity	e	0.0001 (JPL 2020 Satellite Ephemerides)
Tethys Obliquity	θ_0	0.039° (theoretical value; Chen et al., 2014)

*Calculated from other values in this table.

2.4 Example of Methodology

Before presenting our full results, we walk through the procedure for a specific (well-fitting) model of Tethys. We assume the values listed in Table 2.2 as needed. The parameters assumed for this specific model are listed in Table 2.3. From Nimmo et al. (2011) we have the spherical harmonic coefficients of topography in Table 2.4. Using Equations 2.3 and 2.4, we find the spherical harmonic coefficients for topography due to tidal stretching and rotational flattening assuming a normalized moment of inertia of 0.34, also presented in Table 2.4. We assume spherical harmonic coefficients for topography with all the limb profiles used in Nimmo et al. (2011), without excluding those that pass through Odysseus.

From the bolometric bond albedo, solar luminosity, and average distance to

Table 2.3: Assumed parameters for our example of the methodology.

Parameter		Value
Upper Shell Porosity	ϕ	0.2
Average Ice Shell Thickness	d_0	250 km
Average Basal Temperature	$T_{B,0}$	250 K
Moment of Inertia	C	0.340 MR_0^2
Isostasy Type		Equal-pressure Pratt Isostasy
Tide Type		Obliquity Tides

Table 2.4: Spherical harmonic coefficients for observed and modeled properties in our example

l	m	$C_{l,m}^{h,obs}$ (km)	$C_{l,m}^{h,TR}$ (km)	$C_{l,m}^{h,res}$ (km)	$C_{l,m}^{T_S}$ (K)	$C_{l,m}^{F}$ (mW m^{-2})
2	0	-4.76	-4.81	0.042	-8.00	0.685
	2	1.67	1.46	0.21	0.0	0.337
4	0	-0.021		-0.021	-1.18	0.0152
	2	-0.013		-0.013	0.0	-0.0213
	4	0.0014		0.0014	0.0	0.00152
6	0				-0.160	

$C_{l,m}^{h,obs}$: Observed topography of Tethys from Nimmo et al. (2011). These values are not normalized as they are in Nimmo et al. (2011).
$C_{l,m}^{h,TR}$: Topography as a result of tidal stretching and rotational flattening for the example model of Tethys with MoI=0.335 MR_0^2, calculated as in Section 3.1
$C_{2,0}^{h,res}$: Residual topography after removing the contribution from tidal stretching and rotational flattening in our example model of Tethys.
$C_{l,m}^{T_S}$: Surface temperature variation, calculated as according to Nadeau and McGehee (2017).
$C_{l,m}^{F}$: Calculated spherical harmonic coefficients of basal heat flux for the example model of Tethys (Sec. 3.2).

the sun (using Saturn's semi-major axis), we find the average surface temperature to be 68.26 K. We further find the spatial variation of average surface temperature from the orbital inclination (taken as Saturn's tilt) using Nadeau and McGehee (2017) (detailed in the supporting material, Appendix B).

With the choice of Pratt isostasy, we must calculate the average basal heat flux and variations in that basal heat flux required from the observed topography. For our assumed total shell thickness d_0=250 km, upper layer porosity ϕ =0.2, and a basal ice shell temperature T_B =250 K, we use Equation 2.6 to find that the average basal heat flux F_0 =4.65 mW m^{-2} (implying a total power of 4.6 GW generated by Tethys). We also find the average thickness of the porous region of the ice shell L_0 = 156 km. We use d_0 and L_0 to calculate a bulk ice-shell density of 797 kg m^{-3}, from which we may in turn calculate the ratio of basal gravity to surface gravity $\frac{g_B}{g_S}$=1.01 (where surface gravity g_S=0.146 m s^{-2}). The change in crustal density as a function of topography h is then found with Equation 2.12 and yields a value of $\delta\rho$ =3.26×10^{-3} kg m^{-4} h.

We calculate an average thermal expansivity of ice α_0 to use in our model, assuming an average shell temperature of $\bar{T_0} = \frac{1}{2}(T_{S,0} + T_{B,0})$ = 159 K. Then according to Röttger et al. (1994), our volumetric expansivity of solid ice is 8.674×10^{-5} K^{-1}.

Using the change in crustal density $\delta\rho$, average shell thickness d_0, thermal expansivity α_0, and change in surface temperature ΔT_S, we find the change in basal heat flux via Equation 2.17. We take care to make the appropriate substitutions to account for a porous layer (detailed in the supporting information, Appendix B): we use a new bulk expansivity of α_0' =7.36×10^{-5} K^{-1}, and instead of $\frac{d_0}{k_0}(1 - \frac{d_0}{R_0})$ we use

a new value that encompasses the porous layer: 289 m^2 W^{-1}. This yields spherical harmonic coefficients of basal heat flux in Table 2.4. We expect the ratio $\frac{C^F_{2,0}}{C^F_{2,2}} = 2$ for obliquity tidal heating, and find 2.04. Further, we expect $\frac{C^F_{4,0}}{C^F_{4,2}} = -12$, and find -0.71. As we assumed obliquity tides, we also expect $C^F_{4,4} = 0$. We find a non-zero amount, but still smaller than any of the other values. As the degree-4 terms affect our results far less than the degree-2 terms, we regard any deviation from what is expected of the degree-4 terms as of secondary importance.

Performing the multilinear regression without assuming radioactivity, we find the spatial heating pattern weights $\chi_A = 0.250$, $\chi_B = 0.470$, and $\chi_C = 0.280$, with a coefficient of determination $R^2 = 0.991$. The high R^2 of nearly 1 tells us this is a very good fit, indicating it is very likely this heat flux distribution is due to tidal heating. The RMS misfit of forward modeled topography to observed topography is low at 56.8 m, also indicating a very good fit. The high B weight tells us the interior is very likely rigid, supporting our original assumption of Pratt rather than Airy isostasy. This fit is dominated by the degree-2 terms as seen in Table 2.4. As the multilinear regression essentially fits for a plane between the origin, degree-2 coefficients, and degree-4 coefficients, we must still assume degree-4 coefficient values in order to make the fits, despite their small value or large relative uncertainty. Even setting all degree-4 terms to zero, the inferred heating pattern weights only change by as much as 0.03.

By assuming a simplified model of Tethys as 3 concentric, homogeneous layers of a porous ice shell, solid ice shell, and a core, we can derive the internal structure as follows (detailed in the supporting material, Appendix B). Assuming there exists a

porous layer with density $(1-\phi)*\rho_{ice}$ and a thickness L_0 derived from the temperature structure, the remaining unknowns are the core density and total ice shell thickness $d_{3-layer}$ (assumed to have a density ρ_{ice}). Given our two constraints, the moment of inertia and bulk density, we can solve for $d_{3-layer}$ and the core density. We find this thickness to be 236 km, in agreement with our original assumption of 250 km.

This means the core density is 1903 kg m^{-3}, which would be a mix of ice and rock with a 54% rock-fraction by volume. If we calculate the mass of rock in the interior and assume chondritic radioactivity, we find radioactive heat of 0.4 GW, or 8% of the total power generated in Tethys, 4.6 GW. In the Discussion (Section 2.6) we use Equation 2.29 to remove this uniform component by estimating $\chi_D = 0.08$.

2.5 Results

While this paper is focused on the inversion of Tethys' thermal state and interior structure from its long-wavelength topography, we tested our methodology on a world for which we already know the moments of inertia and interior structures: Enceladus. Best-fit results for Enceladus (detailed further in the supporting information, Appendix B) have heating weights that indicate a combination of tidal heating in an ice shell above a subsurface ocean and uniform heating, with moments of inertia and ice shell thicknesses that are broadly consistent with the findings of Iess et al. (2014) and Beuthe et al. (2016). The fraction of heating that is due to uniform heating is more than one would expect from Enceladus' radionuclides but is feasible if about 70% of

Enceladus' total heating occurred in its core and was then redistributed uniformly by the overlying ocean. Having validated our technique, we return to Tethys.

For Tethys we explore a large parameter space, detailed in Table 2.5, assuming the constants in Table 2.2 as needed. While the basal temperature could be lower than 200 K without *any* tidal heating, we did not attain better-fitting results at lower temperatures and thus did not spend more computational time at lower basal temperatures. For each case we followed our outlined methodology (Section 2.3, with an example in Section 2.4) to calculate the average basal heat flux (Equation 2.6), and the heating pattern weights and coefficient of determination R^2 as outlined in the supporting material (Appendix B).

From the derived heat flux distribution, we calculate the ratio of spherical harmonic coefficients for the heat flux distribution, $C^F_{2,0}/C^F_{2,2}$. This serves as a consistency check because if the heating distribution is in fact due to tidal heating, then this ratio will be near 2 for obliquity tides or near -22/3 for eccentricity tides (Table 2.1).

As an additional consistency check we also use a forward model (detailed in the supporting information, Appendix B) to calculate the RMS difference between modeled and observed topography (Equation 2.23) and the RMS difference between the spherical harmonic coefficients of the observed and modeled topography.

As in Section 2.4 (and detailed further in the supporting information, Appendix B), we may generate a density profile of Tethys from the assumed moment of inertia, ice shell thickness, and upper ice shell porosity. We can also do such a physical consistency check if we assume an ocean, where we assume the densities of the porous ice layer, the

Table 2.5: Parameter space of values for Tethys explored in this investigation.

Parameter		Value ranges	Resolution
Porosity	ϕ	0.0-0.3	0.1
Ice Shell Thickness	d	10-250 km	10 km
Average Basal Temperature	$T_{B,0}$	200-270 K	10 K
Moment of Inertia	C	0.3-0.4 MR_0^2	0.005 MR_0^2
Isostasy Type		Equal-Mass or Equal-Pressure, Pratt or Airy	
Tide Type		Obliquity or Eccentricity	

solid ice layer, and the ocean, as well as the thicknesses of the both ice layers. This leaves the core density and the ocean thickness as the only two unknowns.

After we infer the heating pattern and goodnesses of fit for each set of parameters, we can begin to eliminate models with inferred structures that are not physically feasible or not consistent with their assumed parameters. We limit ourselves to results in which the degree 2 spherical harmonic coefficients of our forward modeled topography are within 3× the uncertainty of the observed topography (Nimmo et al., 2011). We further narrow down our results to those where the total ice shell thickness from a three layer model $d_{3\text{ layer}}$ is greater than the porous ice shell thickness L and less than a maximum ice shell thickness $d_{\max}$ imposed by the requirement that the bottom of the shell not melt. If we assume an ocean, we instead limit ourselves to cases where the ocean thickness is greater than 0, and less than the remaining radius of Tethys without either ice layer. We also constrain which results to accept by checking for resulting core densities that are greater than the density of ice. Finally, we limit our results to those where the ratio of degree 2 spherical harmonic coefficients of inferred heat flux $C^F_{2,0}/C^F_{2,2}$ is 2±0.3 for obliquity tides, or -7.33±1.33 for eccentricity tides. While some constraints

can be applied before we even infer the heating pattern, we cannot calculate $C^F_{2,0}/C^F_{2,2}$ or the spherical harmonic coefficients of forward-modeled topography until afterward, and as such apply these constraints after exploring the parameter space.

The constraints listed above greatly reduce the number of viable results (Figure 2.5), and vary little between equal-pressure or equal-mass isostasy. No model results using a combination of Pratt isostasy and eccentricity tides were found to be physically self-consistent. Any results that use Airy isostasy have a lower R^2 compared to results for Pratt isostasy, because the inferred heating pattern does not match the expected tidal heating as well (Table 2.6). We are more-inclined to believe the Pratt isostasy results due to their better R^2 and RMS goodnesses of fit. However, for the sake of thoroughness, we still examine the viability of the Airy isostasy results. These heating pattern weights using Airy isostasy appear slightly perturbed from a uniform heating pattern. In obliquity tide cases, this might be due to a combination of a uniform background heating flux, the heating pattern of core heating, and the heating pattern of an ice shell atop a rigid interior, as the B-weight is increased compared to the 0.4 one expects from a uniform pattern. In Airy isostasy and eccentricity tide cases, the higher C weight could potentially be indicative of an ocean or homogenous interior. However, in these cases higher R^2 are correlated with higher RMS, whereas we seek the cases where R^2 is high and RMS is low. As the R^2 was lower than the Pratt isostasy cases to begin with, we ignore the Airy isostasy and eccentricity tide cases for the remainder of this paper. While we had calculated our constraints with either an ocean or no ocean to not exclude the possibility that Airy could operate with warm ice instead of an ocean,

or that Pratt could still occur with an ocean; the dominance of heating pattern B in all remaining physically-consistent cases is indicative of a rigid interior, so we focus on those results that do not assume an ocean. Within Pratt isostasy and obliquity tides cases, there are 34 successful results for ϕ =0.2 under equal-mass isostasy, and 28 results for equal-pressure isostasy (Table 2.6). For a porosity $\phi = 0.3$, there are 47 successful results for equal-mass Pratt isostasy and 54 for equal-pressure. For Airy isostasy and obliquity tides, there are 12 viable cases spanning upper shell porosities from 0.1 to 0.3, across both equal-pressure and equal-mass cases. However, Airy isostasy is hard to reconcile with the rigid interior deduced from the B-weights, while Airy cases show worse goodness-of-fit values than Pratt cases (see above).

For an idea of Tethys' structure in models that satisfy the physical constraints, we examine the thickness of each layer of the ice shell as well as the average density interior to the ice shell (Figure 2.6). Broadly speaking, in viable equal-mass Pratt isostasy cases (we address the Airy isostasy cases in the discussion, Section 2.6), the porous portion of the ice shell is assumed to vary from >130 to <190 km thick, while the pore-free portion of the ice shell predicted by moment of inertia varies from 0 to 100 km thick (where the thickest porous shells are accompanied by the thinnest pore-free shells and vice-versa). The bulk density of Tethys interior to the ice shell varies from 1600-2000 kg m^{-3}, where the denser cores are accompanied by thicker ice shells. All viable models also result in very low RMS values (Figure 2.6). An ice porosity of 0.2 cannot persist above 25-35 MPa (Durham et al., 2005), which for Tethys would translate to a porous region thickness from $\sim 170 - 210$ km. Greater thicknesses are possible if there

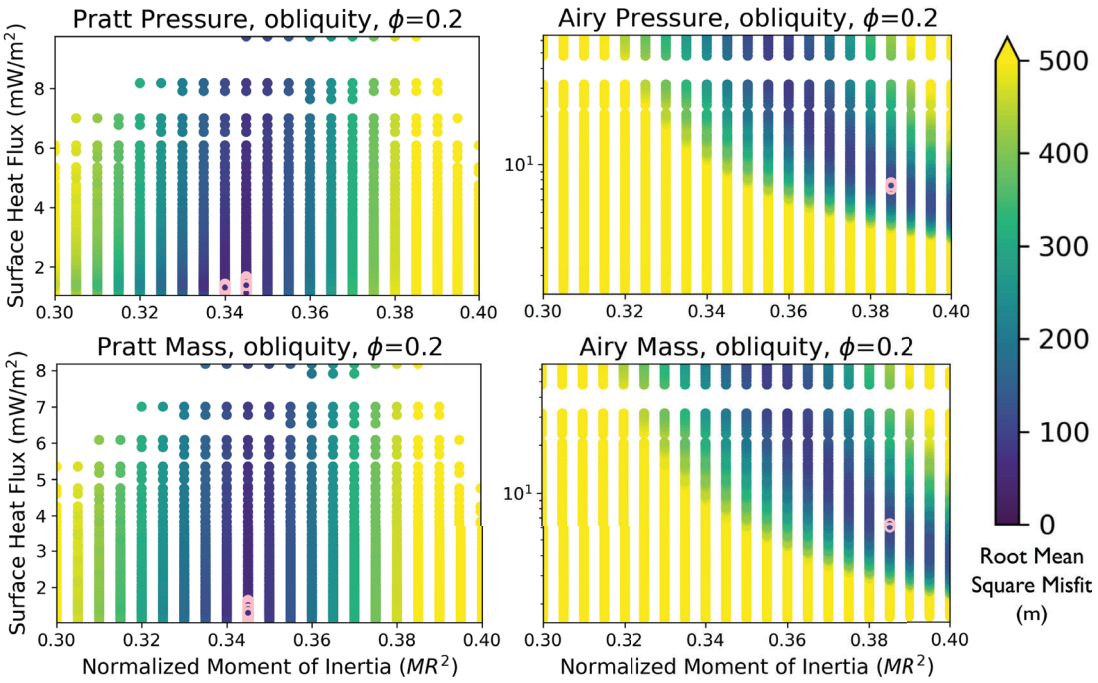

Figure 2.5: For each isostasy and tide type combination, we vary the parameters of upper layer porosity, total ice shell thickness, average temperature at the base of the ice shell, and Tethys' moment of inertia (Table 2.5). All varied parameters but the moment of inertia are captured in the average heat flux. These are the root mean square (RMS) goodness of fit values for all results with 20% upper layer porosity ϕ for a Tethys undergoing obliquity tides. Results that satisfy the constraints assuming no ocean as outlined in the text (Section 3.3) are circled in pink. Results with lower RMS values have been plotted over results of higher RMS values to better highlight which heat fluxes and moments of inertia result in the best fits to observed topography.

was a porosity gradient with an average porosity of 0.2 and lower porosities at depth.

After incorporating the criteria listed above to identify the most physically plausible scenarios, we can quantify the tidal heating patterns of our remaining models in Table 2.6. Full results are hosted in a dryad repository (Gyalay and Nimmo, 2023).

2.6 Discussion

The fact that obliquity tides produced better fits than eccentricity tides is consistent with and even expected from Tethys' very small eccentricity $e \sim 10^{-4}$. A high B heating pattern weight indicates a rigid layer underneath the ice shell (Table 2.6, Figure 2.6), consistent with Pratt isostasy.

We inferred that to satisfy the moment of inertia in Pratt isostasy cases, Tethys must have an ice-rock-mixture core with a radius of about 280-340 km (compared to Tethys' total radius of 531 km), overlain by solid ice, and then a final 130-180 km thick porous ice layer. The interior being an undifferentiated ice-rock mixture is consistent with accretional heating, which yields a heating profile strongest near the surface (Squyres et al., 1988).

In our viable results for equal-mass Airy isostasy, the "core" region is expected to be much larger, with a radius of about 440-490 km. If there is a porous layer, it is not expected to be thicker than 70 km. Due to the lower bulk density in the interior region (< 1100 kg m^{-3}) and the higher amount of power required by the topography ($\sim$20 GW) as compared to the Pratt case, the fraction of power derived from radiogenic

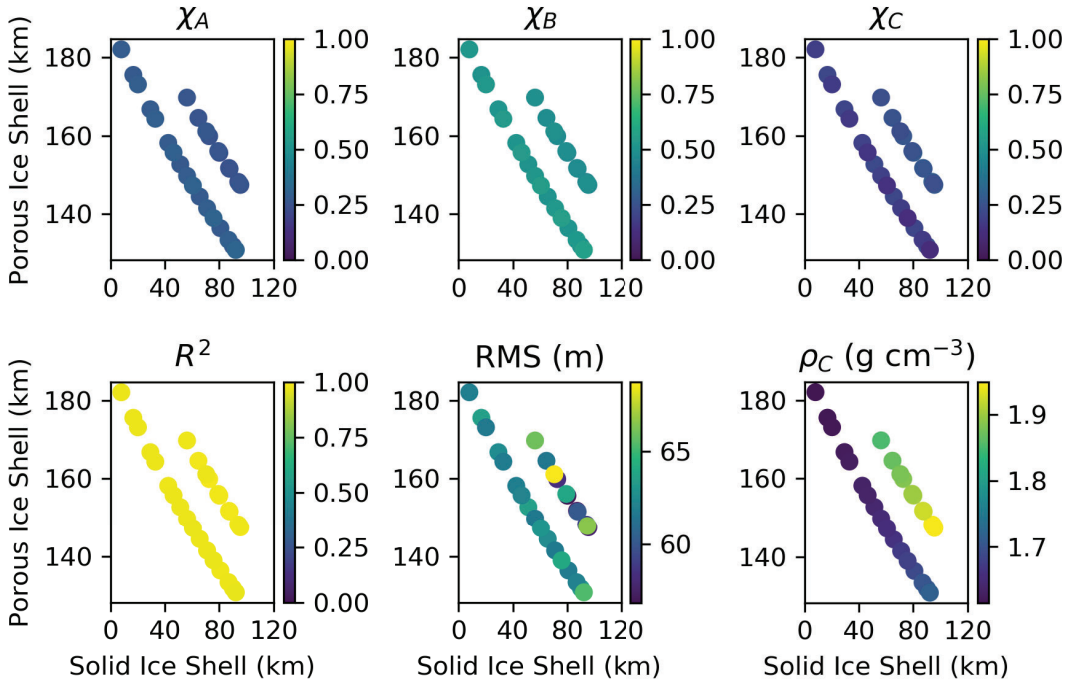

Figure 2.6: These viable results for a Tethys under an equal-mass Pratt isostasy with an outer shell density of $\phi = 0.2$ demonstrate that the tidal heating distribution of Tethys is dominated by heating pattern B, and that this tidal heating distribution fits well. It illustrates also the structure of Tethys. We plot several parameters for each thickness of the porous ice shell L and solid ice shell $d_{3\text{ layer}} - L$. We plot only results for cases with an upper layer porosity of ϕ =0.2 that satisfy all constraints described in Section 3.3. In these models, the basal temperature varies from 200 to 270 K. All results have a surface heat flux of ∼1-2 mW m^{-2} as seen in Figure 2.5. From bottom-left to top-right of each subplot, Tethys' assumed moment of inertia falls from 0.345 to 0.340 MR_0^2.Tethys assumed moment of inertia is 0.335 MR_0^2 for all these models. The parameters plotted are: χ_{A-C}: The respective weights for heating patterns A, B, and C. Each weight can range from 0 to 1. R^2: The coefficient of determination, a measure of how well the multilinearly-regressed heating pattern weights fit the inferred heating pattern, and thus a measure of how well the inferred heating pattern corresponds to tidal heating. R^2 ranges from 0 to 1, with 1 being the best fit. RMS: The root mean square, described Section 2.3.3. A smaller RMS means that there is less misfit between the forward-modeled topography and the observed topography. ρ_C: The bulk density of the "core," everything interior to the ice shell. This gives an idea of the internal structure of Tethys.

Table 2.6: Heating pattern weight statistics for results that fulfill constraints outlined in Section 3.3

Isostasy	Tide	ϕ	Oc?	n	χ_A	χ_B	χ_C	R^2
Pratt (mass)	Obl	0.2	F	34	0.31(3)	0.54(4)	0.15(7)	0.97(1)
Pratt (mass)	Obl	0.2	T	25	0.30(3)	0.54(4)	0.16(7)	0.97(1)
Pratt (pres)	Obl	0.2	F	28	0.28(2)	0.51(3)	0.21(5)	0.979(6)
Pratt (pres)	Obl	0.2	T	45	0.27(3)	0.50(4)	0.22(7)	0.98(1)
Pratt (mass)	Obl	0.3	F	47	0.30(3)	0.54(4)	0.16(6)	0.97(1)
Pratt (mass)	Obl	0.3	T	11	0.31(3)	0.55(3)	0.14(6)	0.96(1)
Pratt (pres)	Obl	0.3	F	54	0.28(3)	0.51(4)	0.22(7)	0.98(1)
Pratt (pres)	Obl	0.3	T	13	0.29(3)	0.52(3)	0.19(6)	0.970(9)
Airy (mass)	Obl	0.1	F	4	0.2034(3)	0.4058(4)	0.3908(7)	0.649(9)
Airy (pres)	Obl	0.1	F	1	0.2018	0.4032	0.395	0.345
Airy (mass)	Obl	0.2	F	2	0.2035(2)	0.4056(3)	0.3909(6)	0.665(8)
Airy (pres)	Obl	0.2	F	3	0.2032(5)	0.4050(6)	0.382(1)	0.64(2)
Airy (mass)	Obl	0.3	F	1	0.2016	0.4026	0.3958	0.3587
Airy (pres)	Obl	0.3	F	1	0.2011	0.4019	0.397	0.3084
Airy (mass)	Ecc	0.2	T	6	0.198(4)	0.387(3)	0.415(7)	0.5(2)
Airy (mass)	Ecc	0.3	F	1	0.2359	0.4153	0.3487	0.6438
Airy (mass)	Ecc	0.3	T	53	0.191(6)	0.382(4)	0.43(1)	0.9(1)
Airy (pres)	Ecc	0.3	T	7	0.20(1)	0.391(8)	0.41(2)	0.6(2)

Note: n is the number of remaining results for each isostasy type, tide type, and upper layer porosity ϕ combination. We indicate in parentheses whether we use pressure- or mass-based isostasy. The ocean (Oc?) column indicates whether the constraint on the density structure of the moon assumed an ocean layer or not. All other combinations yield 0 results after the constraint. For each heating pattern weight χ_{A-C} and coefficient of determination R^2 we list the average and the standard deviation, where the standard deviation is in parentheses following the digit it applies to. e.g. 0.2470(9)=0.2470±0.0009. Isostasy, tide, and porosity combinations with only 1 constrained result have a standard deviation of 0 by definition.

heating is <1%. Although radiogenic heating provides a uniform heating pattern, if the radiogenic contribution is so small then we cannot say that the similarity of the derived heating pattern weights for Airy isostasy to a uniform heating pattern is because of significant radiogenic heating. If we assume ∼60% of the heating pattern is instead due to tidal heating of a homogeneous body (χ_A=0.13, χ_B=0.31, χ_C=0.56), then we can back out a tidal heating pattern that is consistent with a rigid interior below a ∼ 50-80 km ice shell. However, this simultaneously requires an interior that is warm enough to flex tidally and flow to compensate thinner regions of the ice shell, but rigid enough to generate the correct heating pattern weights in the shell. As the interior would only have a maximum rock volume-fraction of 0.09, its rheological properties would be nearly identical to that of just ice (e.g. Roberts, 2015). Simultaneous core and shell heating may be more feasible in a system like Enceladus, where the two regions can independently have the low rigidity and viscosity necessary for tidal heating while separated by an ocean.

Another line of evidence that favors our Pratt isostasy results is its moment of inertia. In Section 2.3.1, we argued that with the method of Thomas and Dermott (1991), we expect Tethys' normalized moment of inertia to lie between 0.34 and 0.37. This is more consistent with the moments of inertia of our best-fit Pratt isostasy cases (0.340-0.345) than with our Airy isostasy cases (nearly homogeneous at 0.380-0.385). And again, our Airy results had a lower R^2 and higher RMS and are thus less likely than our Pratt results in the first place.

One puzzle in our Pratt isostasy results is that the B weights we derive (Table

2.6) are larger than one would expect from a roughly homogeneous body with an ice shell ∼32-47% of the total radius. Despite a high R^2 and a low RMS, the individual heating pattern weights do not produce a consistent value of a rigid core radius. Taking our lowest RMS case for equal-mass Pratt isostasy, we assumed an ice shell thickness of 250 km (assuming a basal temperature of 250 K) which is the equivalent of a ratio of interior radius to total radius R_{int}/R of 0.53. However, the best-fit heating pattern weights are χ_A=0.25, χ_B=0.47, and χ_C=0.28; which would be predicted by a R_{int}/R of 0.78, 0.68, and 0.51, respectively, for a uniform density sphere with a rigid interior (Figure 2.4). These values neither agree with one another, nor with the assumed ice shell thickness. However, if we calculate the predicted radioactivity from the amount of rock in the interior necessary for our derived core density, then we estimate this radiogenic heating is 8% of the total heating predicted by our model. Assuming our inferred heating patterns are a linear combination of a uniform pattern and a tidal heating pattern, we can remove the fraction of the pattern that is uniform by setting χ_D=0.08 in Equation 2.29 to find updated heating pattern weights of χ_A=0.254, χ_B=0.476, and χ_C=0.270. These scarcely change the predicted R_{int}/R for each heating pattern weight. However, if we assume an additional 32% of our inferred heating pattern is due to a homogenous interior that is also tidally flexing, then resulting pattern due only to tidal heating in the ice shell is χ_A=0.32, χ_B=0.56, and χ_C=0.11. All three of these weights each predict that R_{int}/R=0.73 for a uniform density case. This is not equal to our original assumption of 0.53, but closer to the ratio of the interior to the radius of the interior plus the *solid* portion of the ice shell. If we numerically calculate the expected tidal heating for a

stratified Tethys that includes a less-rigid but more-viscous porous ice layer, then these weights *are* what one expects for R_{int}/R=0.55. This suggests that the porous portion of the ice shell can be "ignored" in terms of its effects on tidal heating when the interior is rigid (Figure 2.4).

The removal of the expected radiogenic component and an assumed interior tidal heating component from our heating pattern can thus result in a self-consistent thickness of the solid ice shell. However, the proper heating weights for our ice shell thickness can also be attained by assuming 58% of the inferred heating pattern is a uniform background heating flux. Here, there are other ways of constructing a spatially-constant heat flow from the core without appealing to radioactivity. One is to invoke the sensible heat from cooling of the core from an earlier, hotter state. This pattern might also be modified by porous flow of any liquid water generated (cf. Choblet et al., 2017). If we appeal to tidal heating in the core (cf. Roberts, 2015), which produces a heating pattern equivalent to a body of $R_{\rm int}/R = 0$ in Figure 2.4 (and has heating pattern weights similar to those of a uniform heating distribution), it may seen hard to reconcile with a rigid interior as discussed above. However, in our Pratt isostasy best-fit results, the core has a rock fraction of $\sim$ 54% by volume, rather than the paltry 10% in our Airy isostasy cases. Additionally, because we do not need the ice-rock mixture to flow as in the Airy isostasy case, it is more feasible for this ice-rock mixture to tidally flex while maintaining a greater rigidity and viscosity than the solid ice. The bulk viscosity and rigidity of an ice-rock mixture is not well constrained, but using the solid-body tidal heating numerical code of Roberts and Nimmo (2008) we find we can

create a combination of a tidally-heated ice shell and a tidally-heated interior using an interior viscosity of 7×10^{13} Pa s (compared to our input ice viscosity of 1×10^{13} Pa s), and a rigidity ranging anywhere from 4-40 GPa (compared to our input ice rigidity of 3.3 GPa). This produces a tidal heating pattern of χ_A=0.23, χ_B=0.50, and χ_C=0.27; remarkably similar to our inferred tidal heating pattern.

This combination of shell heating and core heating is only possible because of the strikingly low density of Tethys' core at 1600-2000 kg m^{-3}, which necessitates a high ice fraction. This is similar to that inferred for Enceladus ($\approx$ 2400 kg m^{-3}). In the case of Enceladus the core is assumed to be porous rock potentially filled with ocean. In the case of Tethys, it implies the satellite only ever partially differentiated.

2.6.1 Causes and Consequences of Tethys' Heat Flow

Our inferred ice shell thickness suggests Tethys' surface heat flux is 1.0-1.6 mW m^{-2}. Evidence of relaxed craters implying high heat fluxes ($\sim$50 mW m^{-2}) (White et al., 2017) is not obviously consistent with our arguments in favor of low heat fluxes and a thick porous layer. The most likely resolution of this apparent paradox is that these craters record an ancient period of more intense heating, while our analysis is sensitive to the temperature and heat flux distribution in the recent past. The existence of unrelaxed craters on Tethys like Penelope suggests heat fluxes <3 mW m^{-2} (White et al., 2017) which is roughly consistent with our findings and supports the idea of a heat flux declining with time. One consequence of an early high heat flux episode is that it would have removed porosity by viscous flow (Kossacki and Lorenz, 1996; Eluszkiewicz,

2004; Besserer et al., 2013; Wieczorek et al., 2013; Gyalay et al., 2020) even at shallow depths. Our results would thus require porosity to have been regenerated later, presumably either by subsequent impacts or by tidal-tectonic processes.

This inferred surface heat flux of 1-2 mW/m^2 is an order of magnitude smaller than that inferred for Ithaca Chasma, a flexural feature formed $\sim$ 4 Ga (Giese et al., 2007). Our values are lower presumably because they represent the heat flux closer to the modern day, although it may also be the case that Ithaca Chasma represented a local heat flux maximum. Some hypothesize that Ithaca Chasma formed in response to Tethys entering a resonance with Dione (Chen and Nimmo, 2008; Hussmann et al., 2019). As this would excite Tethys' eccentricity, Ithaca Chasma would have formed in response to eccentricity tides rather than our predicted obliquity tides. Given that Ithaca Chasma is an ancient feature, it seems likely that it formed in response to early eccentricity tides, while more recently the eccentricity damped and Tethys has been dominated by obliquity tides (inclination damps more slowly than eccentricity). As Odysseus crater is younger than Ithaca Chasma (Giese et al., 2007), it may even be that the Odysseus impactor excited Tethys' inclination (and obliquity along with it) and/or broke an earlier eccentricity-type resonance (Zhang and Nimmo, 2012).

Integrating average heat flux of 1-2 mW/m^2 across the entire surface, we find Tethys emits a total power of $\dot{E}$=3.5-7.1 GW, of which up to around 10% may be from radiogenic heating. According to Chen et al. (2014) and references therein, the rate of

solid body dissipation is given by

$$\dot{E} = \frac{3}{2}\frac{k_2}{Q}\frac{(\omega R)^5}{G}(7e^2 + \sin^2\theta_0), \tag{2.30}$$

for a tidal Love number k_2, tidal quality factor Q, angular rotational frequency ω, radius R, gravitational constant G, eccentricity e, and obliquity θ_0.

Taking the inferred heat flow and assuming Tethys parameters in Table 2.2, we find $\frac{k_2}{Q}$=0.08-0.17. For reference, $\frac{k_2}{Q} \sim 0.01$ for Enceladus (Nimmo et al., 2018) and Io (Lainey et al., 2009), where a higher value is more dissipative. It is hard to imagine present-day Tethys this dissipative without other obvious evidence such as recent resurfacing or active plumes.

Instead of requiring such a dissipative structure, we can appeal to the obliquity. The obliquity in Table 2.2 of 0.039° is a theoretical Cassini state value calculated from the hydrostatic shape of Tethys (Equation 68 of Chen et al., 2014), and not an observation. This obliquity varies little with assumed moment of inertia or even using the spherical harmonic coefficients of topography converted to gravity (using k_2 instead of h_2 in Equations 2.3 and 2.4). Increasing the obliquity to a value of 0.12-0.17°, the required k_2/Q then drops to < 0.01.

Using the solid-body tidal heating numerical model of Roberts and Nimmo (2008), we can calculate the k_2/Q and power produced for a given spherically-symmetric material profile of Tethys. As a proof-of-concept we assumed a 250 km thick ice shell (47% of Tethys' radius), the upper 156 km of which is porous. To begin, we assume the interior has the rigidity and viscosity of pure rock as a point of comparison. We

assumed the rigidities of solid ice, porous ice, and rock were 3.3×10^9 Pa, 3.3×10^8 Pa, and 10^{11} Pa, respectively; while their viscosities were taken to be 10^{13} Pa s, 10^{18} Pa s, and 10^{20} Pa s, respectively. This structure requires an obliquity of 0.17° to produce 4.2 GW of tidal heating, and has a k_2/Q of 0.006. While the viscosity of ice is expected to vary exponentially with respect to temperature, we kept it constant for simplicity. Including this dependence, one would expect to need an even higher obliquity to generate the same amount of heating. As we demonstrated earlier, the interior of Tethys may itself be tidally flexing. Replacing the rock rigidity and viscosity with 4×10^{10} Pa and 7×10^{13} Pa s, respectively, we now need only an obliquity of 0.14° to produce 4.2 GW of tidal power, and calculate a k_2/Q of 0.009.

The calculations described above suggest that Tethys requires an obliquity that is a minimum of 0.08-0.15° greater than the value derived assuming it occupies a Cassini state. As obliquity and inclination are intricately linked, we briefly investigate the change in Tethys' inclination from an impact. We find that to change Tethys' inclination by 0.1-0.3° (using Equation 11 in Canup (2004), modified for an impact at some angle from the orbital axis), we calculate a 2000 kg m^{-3} density object impacting at 0.4-1 km s^{-1} would have a diameter of about ∼180 km and leave a crater with a similar diameter to Odysseus (following Barnouin-Jha et al., 2007; Zhang and Nimmo, 2012). Such a slow impactor implies it would have been a near-neighbor of Tethys prior to the collision.

As we expect a high obliquity to damp over time, we consider two possibilities: either Tethys has a high obliquity at present (discussed above), or Tethys *had* a high

obliquity. As discussed earlier, the conduction timescale of a 100 km ice shell is hundreds of millions of years. An ice shell up to 250 km as we are inferring can easily push this timescale to a billion years. Then higher tidal heating from a high past obliquity could still be expressed in the present-day surface topography, even though the heat production is no longer operating, because lateral temperature contrasts have not yet diffused away. Further, given the sensitivity of the porous layer thickness to the maximum historic heat flow, the average thickness of the porous layer when Tethys was hotter could have been locked in as the ice will not easily regenerate porosity at depth. Thus, the present-day topography may be a window into a warmer past. Because Tethys' topography may betray its heating state from a billion years ago, this may suggest Tethys did not coalesce out of Saturn's ring system 100 Myr ago as suggested by Ćuk et al. (2016). However, this potential billion-year minimum lifetime does not discriminate between Lainey et al. (2020)'s rough estimates for Tethys' lifetime between a constant Saturn Q case ($\sim$ 1.5 Gyr) or a resonance-locking case ($\sim$ 4 Gyr). Of note, the estimated age of Odysseus crater ranges from between 0.2–1.9 Gyr to $\sim$3.9 Gyr (Giese et al., 2007), 1.06–3.76 Gyr (Dones et al., 2009), 0.4–1.0 Gyr (Kirchoff and Schenk, 2010), or on the order of 3.5 Gyr (Kirchoff et al., 2018). If Tethys' current long-wavelength topography is due to a tidal heating state 1 Gyr ago, this coincides with some estimates for Odysseus' age and thus perhaps with when the Odysseus impactor increased Tethys' obliquity. However, crater counting is an inexact science that still grapples with how different impactor populations at Saturn affect crater production functions (e.g. Zahnle et al., 2003; Ferguson et al., 2022). The mechanism by which the obliquity could have been

excited to generate our inferred tidal heating remains unclear but would be interesting to study in future work. Another potential avenue to explore in future is the role of lateral variations in the thickness of the porous layer (cf. Besserer et al., 2013).

2.7 Conclusion

We have assumed that Tethys' long-wavelength shape is influenced by tidal heating, and have derived the heat fluxes required to match the observations. Our best-fit models require Pratt isostasy (suggesting the absence of an ocean) and obliquity tides, consistent with Tethys' extremely small eccentricity. The resulting inferred structure consists of an outer porous ice layer, a solid ice layer and then an ice/rock core with a density similar to that of Enceladus's.

The heat fluxes required to explain the topography are modest, $1-2$ mW m^{-2}, but exceed the likely present-day heat production for reasonable values of k_2/Q for Tethys. We suggest that this inferred heat flux is a signature of higher heating rates in Tethys' relatively recent past, perhaps due to a period of higher obliquity.

Acknowledgements

We are grateful to Mikael Beuthe and an anonymous reviewer for their constructive comments. Conversations with Brynna Downey improved our consideration of orbital dynamics.

Open Research

Data generated from models and analyzed in this work are hosted in a dryad repository (Gyalay and Nimmo, 2023). The python code used to produce the data has also been uploaded to the repository.

Chapter 3

Effects of Transient Obliquity Tides Within Mimas' Warm, Icy Interior Preserved as a Frozen Fossil Figure

> HERCULES: What's this? The baleful Giants are taking arms. Tityos has escaped the shades and, with breast all torn and empty, has almost reached the sky. Cithaeron is tottering, lofty Pellene quakes, and Tempe's beauty fades. Here one Giant has seized Pindus' peak, there one has seized Oete, while horribly Mimas rages.
>
> —*Hercules Furens*, by Seneca, translated by Frank Justus Miller

A slightly modified version of this chapter will be submitted to the *Journal of Geophysical Research: Planets* as an article by S. Gyalay, F. Nimmo, and B. G. Downey.

Key Points

- We infer spatial variations in tidal heating and ice-shell thickness from Mimas' non-hydrostatic shape.

- Our inferred Mimas interior has no sub-surface ocean but requires high obliquity tides in Mimas' past.
- Mimas' past obliquity may have been excited by gravitational interaction with an inward-migrating debris disk that formed Saturn's rings.

Abstract

Mimas has a high eccentricity and an anomalously high physical libration like its neighbor, Enceladus, but does not appear to have a geologically active surface. We investigate Mimas' interior with a technique that infers spatial variations in tidal heating from its global shape. To account for its hydrostaic shape, we find Mimas' normalized moment of inertia is 0.375, indicating a relatively undifferentiated world. Its remaining topography is consistent with a ∼30 km thick conductive ice shell in Airy isostasy atop a weakly convecting ∼30 km thick layer that itself mantles a ∼140 km radius ice-rock interior. The convective shell's density must be closer to the interior density to satisfy our moment of inertia and provide a denser compensating layer for Airy isostasy. This ice-rock interior is elongated on the Mimas-Saturn axis, which can match Mimas' observed physical libration without appealing to an ocean. The inferred ice shell thickness variations indicate a high obliquity ($\approx 1.7^\circ$). We suggest this was a transiently high obliquity that damped rapidly, after which topography froze in when internal heat was conducted out of Mimas quicker than isostatic ice shell thickness variations could relax. We speculate on several possibilities for this transient high obliquity, including

excitement by ring-forming material following the recent tidal disruption of an eccentric satellite. We cannot rule out a young Mimatean ocean, but our inferred moment of inertia favors a Mimas that was solid when Saturn's rings formed, did not significantly melt during a recent resonance with Enceladus, and is solid today.

Plain Language Summary

While Saturn's moon Mimas appears to have an ancient surface covered in craters, it also has a highly elliptical orbit and a wobble in its rotation that is higher than expected. This wobble could indicate Mimas has either an ocean or an elongated core. To investigate the possibility of an ocean, we examine differences from sphericity in Mimas' shape, which we also refer to as topography. Some of this is from Mimas' tidal bulge and rotational flattening. Assuming the rest is due to differences in heat that arise due to tidal forces, we can relate Mimas' topography to its tidal heating pattern. Because a moon's tidal heating pattern is influenced by its interior structure, we can then make inferences on Mimas' interior. What we find indicates that the tidal heating conditions that produced Mimas' shape indicate its spin pole was once tilted much higher than one would expect at present day. This could have occurred long ago, after which the topography froze in when Mimas rapidly cooled. The tidal heating pattern we infer also indicates that Mimas did not have an ocean at the time of this strong tidal heating, and likely remains solid to this day.

3.1 Motivation: the Mimas-Enceladus Paradox

It is a truth universally acknowledged, that an icy satellite in possession of significant eccentricity, must be in want of a subsurface ocean. Like his more-famous brother, Enceladus, the icy satellite Mimas has an elliptical orbit around Saturn; with eccentricities 0.0047 and 0.0196, respectively. Each satellite is tidally stretched in response to the difference in gravity it experiences from Saturn at either end of the satellite. As such, a synchronous satellite (where its orbital period is equal to its spin period) would experience frictional heating as its tidal bulge stretches and shifts in response to oscillations in the magnitude and direction of Saturn's gravity. Further, the two moons have similar diameters and semi-major axes. However, because Mimas is closer to Saturn with a more eccentric orbit, then a Mimas with the ability to dissipate heat comparable to that of Enceladus should have $> 50\times$ the average surface heat flow of Enceladus due to tidal heating—yet while Enceladus experiences cryovolcanism and resurfacing, Mimas appears geologically inert despite the circumstances.

This has been dubbed by some as the "Mimas-Enceladus Paradox," and the paradox has only deepened in recent years with the measurement of Mimas' anomalously high libration (Tajeddine et al., 2014), which, like Enceladus' anomalously high libration (Thomas et al., 2016; Nadezhdina et al., 2016), indicates the satellite is wobbling in response to gravitational torques from Saturn on the satellite's tidal bulge more than one would expect for a fully solid, hydrostatic satellite. For Enceladus, this indicates its ice shell is decoupled from its interior by a subsurface ocean in agreement with results

from gravity data (Iess et al., 2014; Beuthe et al., 2016; Hemingway and Mittal, 2019). For Mimas, this could likewise indicate a subsurface ocean but may alternatively indicate an elongated, non-hydrostatic core (Tajeddine et al., 2014), rather than a subsurface ocean being required.

Recently, Rhoden and Walker (2022) have demonstrated that tidal heating within Mimas may be capable of maintaining a global, sub-surface ocean *without* relaxing craters on its surface. Further, the impact that created Mimas' largest crater, Herschel, could have occurred without cracking through Mimas' ice shell and may even be necessary to explain Herschel's geomorphology (Denton and Rhoden, 2022). However, another paradoxical aspect of Mimas' orbit is that if its eccentricity *did* incur enough tidal heating to maintain such an ocean, it would quickly dissipate Mimas' eccentricity and circularize its orbit in a timescale on the order of 50-60 Myr (e.g., Meyer and Wisdom, 2008; Noyelles et al., 2019). This is problematic because Mimas' eccentricity is not currently being excited in an eccentricity-type resonance (as opposed to its current *inclination*-type resonance; cf. e.g., Sinclair, 1983; Vienne et al., 1996; Champenois and Vienne, 1999), although it may have passed through such resonances with other moons in the past (e.g. Meyer and Wisdom, 2008). Further, a gap between Saturn's A and B rings known as the Cassini Division may have been cleared by a resonance with Mimas (Baillié et al., 2019) after Mimas was itself caught in a prior eccentricity-type resonance with Tethys or Enceladus and migrated inward (Noyelles et al., 2019). Unless the Saturnian satellites were young (cf., Ćuk et al., 2016), it would be a coincidence for humanity to observe a recently-formed, Mimatean, sub-surface ocean; but Saturn's

ring system may also have formed recently (Goldreich and Tremaine, 1982; Zhang et al., 2017; Iess et al., 2019), perhaps from the tidal disruption of an unstable satellite within the last ∼100 Myr (Wisdom et al., 2022). Hyodo and Charnoz (2017) also considered the possibility that a head-on collision of two of Saturn's satellites could generate the debris to form Saturn's rings recently, but found it was more likely that such a collision would result in a young satellite system with little-to-no rings. However, more recent work by Kegerreis et al. (2023) demonstrates that such a collision may have formed both Saturn's satellite system *and* rings recently. Moreover, a glancing impact between two of Saturn's satellites could have formed Saturn's ring with a debris cascade that did *not* destroy the satellite system that existed at the time (Kegerreis et al., 2023). Returning to the Cassini division, if its formation was due to a past high eccentricity and migration of Mimas, then Mimas may have gained its present eccentricity recently, within the rings' lifetime (a few 100 Myr). Even if the rings were primordial, the stability of the Cassini Division is on the order of 40-50 Myr and may only have formed 4-11 Myr (Baillié et al., 2019), implying an even *more* recent resonance in Mimas' past. If this eccentricity-type resonance was with Tethys, Mimas would have melted significantly; while if it was with Enceladus, Enceladus instead would have melted (and differentiated) while Mimas stayed relatively cool (Noyelles et al., 2019).

With evidence for a Mimatean ocean still circumstantial at best, only a look inside Mimas can truly answer this question. Unfortunately, there is no gravity data for Mimas. In recently work by Gyalay and Nimmo (2023) (Chapter 2), however, we argue that spatial variations in tidal heating within icy satellites such as Mimas may manifest

in the satellite's global shape. As the tidal heat distribution is sensitive to the satellite's interior structure (e.g. Segatz et al., 1988; Beuthe, 2013), we can infer Mimas' interior structure from its external shape. We begin with a summary of Gyalay and Nimmo (2023)'s mathematical methods in Section 3.2, analyze our results for Mimas in Section 3.3, and finally cover its implications for the history of the Saturn system in Section 3.4 before we recapitulate and conclude in Section 3.5.

3.2 Mathematical Methodology

This paper uses the same mathematical methods as Gyalay and Nimmo (2023) (Chapter 2), which inferred the interior structure of Tethys from its long-wavelength topography. We highlight the most important equations as a quick reference, but readers seeking a detailed treatment of the mathematics are encouraged to read that paper and its supplement (Appendix B), the latter of which includes a test on Enceladus that found its ocean.

3.2.1 Shape and spherical harmonics

For a massive enough icy satellite, its self-gravity should ensure that the satellite adopts a practically spherical shape in hydrostatic equilibrium. Of course, spinning bodies will become oblate due to rotational flattening. Further, a satellite is not in a (metaphorical) vacuum: because it orbits a planet, the planet will raise a tidal bulge upon the satellite. When a satellite is in a synchronous orbit, there is an average, "permanent," bulge along the axis that points from the satellite to its host planet.

The shape $H(\theta, \lambda)$ of nearly-spherical bodies such as icy satellites can be described as function of the distance between the satellite's surface from its center of mass as a function of colatitude θ ($\frac{\pi}{2}$ subtracted by the latitude, where Northern latitudes are positive) and longitude λ (where East is positive). As a surface defined in spherical coordinates, one may then describe the shape using spherical harmonics. Here, some function $f(\theta, \lambda)$ is the sum of spherical harmonics with coefficients $C_{l,m}$ and $S_{l,m}$ for each degree l and order m,

$$f(\theta, \lambda) = \sum_{l=0}^{\infty} \sum_{m=0}^{l} \left(C_{l,m} \cos m\lambda + S_{l,m} \sin m\lambda \right) P_{l,m} \left(\cos \theta \right), \tag{3.1}$$

where $P_{l,m}(\cos\theta)$ is an associated Legendre function (e.g., Blakely, 1995). The spherical harmonic degree l indicates the length-scale (or wavelength) over which some value oscillates across a sphere. This wavelength is (approximately) the sphere's circumference divided by the degree l.

Due to the axial symmetry of both rotational flattening and the tidal bulge, we need only the cosine terms of Equation 3.1 in even orders of degree-2. In this paper, we will refer to the spherical harmonic coefficients of shape as $H_{l,m}$. The second-order approximation of a satellite's hydrostatic shape from the theory of figures that accounts for rapid rotation (i.e., a spin period of less than a few days, as derived by Beuthe et al., 2016) are defined as a function of the fluid Love number h_2^F (of order unity), such that

$$\begin{aligned} H_{2,0}^{hyd} &= -\frac{5}{6} h_2^F R_0 q \left(1 + \frac{76}{105} h_2^F q \right), \\ H_{2,2}^{hyd} &= \frac{1}{4} h_2^F R_0 q \left(1 + \frac{44}{21} h_2^F q \right), \end{aligned}$$

where q is the ratio of rotational and gravitational forces, $q = \frac{\omega^2 R_0^3}{GM}$ (cf. Zharkov and

Gudkova, 2010; Tricarico, 2014). These equations are identical in function to Equations 2.3 and 2.4, except we use updated notation as follows: we use $H^{hyd}_{l,m}$ in place of $C^{tr}_{l,m}$ and h^F_2 in place of h_2. By dropping the higher order term within the parentheses, the ratio $-H^{hyd}_{2,0}/H^{hyd}_{2,2}$ can readily be calculated as its first order approximation, 10/3. Because the term $H^{hyd}_{2,2}$ has a greater second-order increase compared respectively to the second-order increase of $H^{hyd}_{2,0}$, the actual ratio $-H^{hyd}_{2,0}/H^{hyd}_{2,2}$ will shrink from 10/3.

For a hydrostatic body, the fluid Love number h^F_2 is related to the body's mean moment of inertia C (a measure of mass distribution) by the Darwin-Radau relation (e.g. Munk and MacDonald, 1960) (Equation 2.2), where the moment of inertia has been normalized by the satellite's mass M and mean radius R_0 squared. The normalized moment of inertia for a sphere of uniform density is 0.4 MR^2_0, and lower if more mass is concentrated in the core.

The observed tri-axial shapes of some icy satellites deviate from what one would calculate under the assumption of hydrostatic equilibrium even when accounting for rapid rotation. For instance, the ratio $-H_{2,0}/H_{2,2}$ is observed to be lower than expected from the hydrostatic assumption for Rhea or Tethys, but higher for Dione, Enceladus, or Mimas (e.g. Thomas, 2010; Nimmo et al., 2011). Focusing on Mimas, this implies some strong non-hydrostatic contribution to its degree-2 topography. If one assumes an icy satellite's shell is thermally conductive and in a steady state, spatial variations in tidal heat at the base of the ice shell (where ice is warmest and tends to be most dissipative at the orbital frequencies of icy satellites, e.g. Hemingway and Mittal, 2019) would ostensibly manifest as variations in ice shell thickness or ice shell density

(via thermal expansion) at those same wavelengths. With the assumption of isostasy (see, e.g., Hemingway and Masuyama, 2017; Beuthe, 2021, for thorough discussions on different methods of assuming isostasy and their respective merits), these would then translate to observable topography at the long wavelengths and thus contributes to the satellite's observable global shape (Chapter 2, Gyalay and Nimmo, 2023).

In addition to even orders of degree-2, tidal heating varies spatially in even orders of spherical harmonic degree-4 (Beuthe, 2013). Mimas degree-4 shape is also strongly dominated by its even-order terms as is its degree-2 shape (Nimmo et al., 2011), indicating some strong contribution to shape in those same spherical harmonics. Thus, in this paper, we assume the remainder of global shape (after removal of the hydrostatic shape) in even orders of degree 2 and 4 is due to isostatic topography variations in response to the spatial variations in steady state tidal heating.

3.2.2 Spherical harmonics of tidal heating

How tidal heating varies spatially across a satellite depends greatly on the depth or thickness of the tidal-heat-producing region (e.g., the ice shell), whether the tidal-heat-producing region overlies a more rigid (e.g., rocky mantle/core) or a more fluid (e.g., ocean) layer, and whether the tides are caused by the satellite's eccentricity (orbit's ellipticity) or obliquity (tilt of the satellite's spin axis relative to the normal of its orbital plane). Beuthe (2013) demonstrated that this distribution of tidal heat raised within a satellite could be constructed as the linear combination of three basis heating patterns, A, B, and C. These basis functions are themselves linear combinations of

spherical harmonic functions of even degrees $l \leq 4$ and even orders m. The basis set of angular functions ψ_J ($J = A,\ B,$ or C) are reproduced from Beuthe (2013) in Equations 2.18 to 2.21. Coefficients $a_{l,m}$ are constants that depend only on if tidal heating is due to the satellite's eccentricity or obliquity; values may be found in Table 2.1 (following Beuthe, 2013). Note that $\psi_0 = a_{0,0}$. Then given a spatially-averaged heat flux due to tidal heating F_0, we find the variations in heat flux F in Equation 2.22 where χ_J are weights of each basis angular function (Beuthe, 2013). Each weight ranges from 0 to 1, and the sum of all three is 1.

In the limit of a thin shell undergoing tidal heating atop an ocean, $(\chi_A,\ \chi_B,\ \chi_C) = \frac{1}{11}(2,\ 0,\ 9)$, while that same thin shell atop a rigid interior is completely dominated by $\chi_B \sim 1$ (Beuthe, 2013). In the opposite limit where the entire satellite produces tidal heat, the heating pattern is $(\chi_A,\ \chi_B,\ \chi_C) = (0.13,\ 0.31,\ 0.56)$ (Beuthe, 2013). One can infer the thickness of a satellite's ice shell, and whether it overlies a fluid layer, from the nonlinear dependence of a satellite's heating pattern weights on its ice shell thickness relative to its total radius (Figure 2.4; Chapter 2, Gyalay and Nimmo, 2023).

Often, the total heat flux distribution F (and thus its basis heating functions ψ_J) include contributions from a uniform background heat flux (e.g., in cases of radiogenic heating in the core) or, if the satellite is mostly composed of ice, tidal heating within the satellite's core (Gyalay and Nimmo, 2023). The heating pattern weights of a uniform heat flux are $(\chi_A,\ \chi_B,\ \chi_C) = (0.2,\ 0.4,\ 0.4)$, while the heating pattern weights of tidal heating in a homogeneous interior are $(\chi_A,\ \chi_B,\ \chi_C) = (0.13,\ 0.31,\ 0.56)$ (identical to the heating pattern of satellite experiencing full-body tidal heating; Beuthe,

2013).

Following some mathematical finesse with the preceding five equations that take advantage of the orthogonality of spherical harmonics (see Appendix B, the supporting information of Chapter 2 or Gyalay and Nimmo, 2023), one can calculate the spherical harmonic coefficients of heat flux $F_{l,m}$ for even orders m of degrees $l = 2,\ 4$ as it deviates from the mean flux F_0 of a tidal heating distribution as a system of equations:

$$\frac{a_{0,0}}{a_{l,m}}\frac{F_{l,m}}{F_0} = \begin{cases} \chi_A + \frac{1}{2}\chi_B - \chi_C, & \text{if } l = 2, \\ \chi_A - \frac{2}{3}\chi_B + \frac{1}{6}\chi_C, & \text{if } l = 4. \end{cases} \tag{3.2}$$

Given spherical harmonic coefficients of heat flux for an inferred heating pattern at the base of Mimas' ice shell, we may then use this system of equations (Equation 3.2) to perform a multi-linear regression and calculate its best-fit tidal heating pattern weights. As a linear regression, we can also calculate the coefficient of determination R^2 which here essentially measures how well some inferred heat pattern can be approximated by a tidal heating pattern. In general, the magnitude of the degree 4 spherical harmonic coefficients of heat flux are lower than the degree 2 terms and have less of an effect upon the resulting best-fit heating pattern weights compared to the degree terms. However, we still require these terms to avoid a degenerate fit (this is discussed in more depth in 2, Gyalay and Nimmo, 2023).

3.2.3 Inferring a heating pattern from topography

To determine the tidal heating pattern weights of Mimas' interior, we must first infer the heat flux distribution at the base of Mimas' ice shell. As mentioned

previously, we can relate the basal heat flux to Mimas' topography by assuming its ice shell is in isostatic equilibrium. There are two endmember methods of maintaining isostatic equilibrium in spite of topographic variation: compensation beneath regions of thinner shell in Airy isostasy, or variation in shell density in Pratt isostasy. In both scenarios, the ice shell thickness varies about some mean shell thickness $d = d_0$ that we can define using Fourier's law of heat conduction assuming the thermal conductivity k of ice is temperature dependent $k = k_0/T$ (e.g. Klinger, 1980) along with average values of the surface temperature T_S, temperature at the base of the ice shell T_B, and heat flux at the base of the ice shell F_b;

$$F_b = \frac{-k_0 \ln \frac{T_S}{T_B}}{d\left(1 - \frac{d}{R_0}\right)}. \tag{3.3}$$

We detail adjustments for assuming porosity in the upper portion of the ice shell in Gyalay and Nimmo (2023) (Chapter 2).

3.2.3.1 Airy isostasy

In the case of Airy isostasy, the ice shell thickness variations Δd can be related to variation in the surface topography h. When assuming equal-pressure isostasy, this is also a function of the ratio between gravity at the surface of the satellite g_S and gravity at the base of the ice shell g_B. This results in Equation 2.9, where ρ_C is shell density and $\Delta\rho$ is the density contrast between the ice shell and the underlying material (Hemingway and Masuyama, 2017). In the limit of a thin shell $d \ll R_0$, $g_B = g_S$ and Equation 2.9 reduces to the classic equal-mass solution. If the ice shell is thick, however,

a consideration equal-mass isostasy needs to account for difference in volume due to a change in topography using Equation 2.10.

One can then directly calculate the basal heat flux F_b of a given location using Equation 3.3 with the appropriate adjustment of $d = d_0 + \Delta d$, where Δd is calculated from topography with Equation 2.9 when assuming equal-pressure isostasy or Equation 2.10 when assuming equal-mass isostasy. One could also consider minimum-stress isostasy (Beuthe, 2021), which can be approximated by equal-weight isostasy. Results using equal-weight isostasy will fall between the results expected for equal-pressure and equal-mass isostasy, and thus we continue with a consideration of equal-mass and equal-pressure isostasy as endmembers.

3.2.3.2 Pratt isostasy

In Pratt isostasy, we must vary the ice shell's density to maintain mass or pressure at depth despite surface topography. In our consideration of Pratt isostasy, we made the simplifying assumption that changes in density were due to the thermal expansion or contraction of the ice shell in response to changes in basal heat flux, as done by Gyalay and Nimmo (2023) (Chapter 2). Lateral variations in upper ice shell porosity may exist in response to viscous pore closure during some past epoch of high heat flux (e.g. Besserer et al., 2013), but would require a consideration of the global thermal evolution of Mimas that is outside the scope of this paper.

By relating the basal ice shell temperature T_B to the basal heat flux F_B in Equation 3.3, Gyalay and Nimmo (2023) (Chapter 2) derive that the change in basal

heat flux implied by topography due to Pratt isostasy in Equation 2.17, where α_0 is the thermal expansivity at the average ice shell temperature $\bar{T} = \frac{1}{2}(T_B + T_S)$. The change in average ice shell temperature $\Delta\bar{T}$ from the reference $\bar{T}_0 = \frac{1}{2}(T_{B,0} + T_{S,0})$ is related to the change in density of the ice shell as derived from the surface topography. This formulation depends on whether we assume equal-mass or equal-pressure Pratt isostasy (Hemingway and Masuyama, 2017; Gyalay and Nimmo, 2023). Treatment of Pratt isostasy in the consideration of upper shell porosity is detailed in supporting material (Appendix B) of Gyalay and Nimmo (2023) (Chapter 2).

3.2.4 Summary of Methodology

To infer the interior of Mimas, we repeat the methodology of Gyalay and Nimmo (2023) (Chapter 2). We begin with the observed topography from Nimmo et al. (2011) from which we subtract the contribution from its hydrostatic shape as calculated using Equations 2.3 and 2.4 for some assumed moment of inertia $C/(MR_0^2)$. From the remnant topography, we calculate spatial variations in basal heat flux using Equation 3.3 when assuming Airy isostasy or 2.17 when assuming Pratt isostasy; both of which require some assumptions about the average ice shell thickness d_0, upper ice shell porosity ϕ, and average basal ice shell temperature T_B. Latitudinal variation in surface temperature is calculated following Nadeau and McGehee (2017) using Mimas' bolometric bond albedo A_{BB} (Appendix B of Chapter 2, Gyalay and Nimmo, 2023). In either case of Pratt or Airy isostasy, we must also assume an equal-mass or equal-pressure treatment of isostasy. We may then perform a multi-linear regression upon

the spherical harmonic coefficients of heat flux $F_{l,m}$ in the System of Equations 3.2 to calculate the heating pattern weights χ_J, with the assumption of either eccentricity or obliquity tides. These weights then can be used to determine the tidal heating state and thus interior structure of Mimas.

3.3 Results and Discussion

The parameters we used in our Mimas model are presented in Table 3.1, held constant or varied as specified in order to explore our wide parameter space. For each model, we computed the heating pattern weights χ_J and their coefficient of determination R^2 as a goodness of fit. Another goodness of fit measurement we undertook was the root mean square (RMS) difference between observed topography and topography forward modeled from our best fit heating pattern weights χ_J. We further check for self-consistency of each model, such as whether the thickness and density of interior layers is compatible with the assumed moment of inertia. For more detail on calculating RMS and our other self-consistency checks, see Gyalay and Nimmo (2023) (Chapter 2).

Scouring through our results (which can be found in an online repository, Gyalay et al., 2023), we find no successful models that assumed Pratt isostasy. This leaves Airy isostasy models, implying Mimas' ice shell lies atop a denser, more-fluid layer. The assumptions of equal-mass isostasy and equal-pressure isostasy returned similar results. Further, any models that assumed eccentricity tides had a high misfit between Mimas' observed topography and topography forward-modeled from the mod-

Table 3.1: Assumed and varied parameters for Mimas

Parameter		Value	Note
Radius	R_0	198.2 km	(Roatsch et al., 2009)
Ang. Rotation Rate	ω	7.72×10^{-5} rad s^{-1}	(JPL 2020 Satellite Ephemerides)
Bulk Density	$\bar{\rho}$	1148 kg m^{-3}	(Roatsch et al., 2009)
Bolometric Bond Albedo	A_{BB}	0.54	(avg. of Howett et al., 2010, 2011)
Avg. Surface Temp.	$T_{S,0}$	74 K	Calculated from A_{BB}
Thermal Cond. Constant	k_0	567 W m^{-1}	(Klinger, 1980)
Annealing Temp.*	T_A	140 K	(Besserer et al., 2013)
Solid Ice Density	ρ_{ice}	940 kg m^{-3}	
Porosity	ϕ	0.0-0.3	0.1 steps
Avg. Ice Shell Thickness	d_0	2-76 km	2 km steps
Avg. Basal Temp.	$T_{B,0}$	200-270 K	10 K steps
Moment of Inertia	C	0.3-0.4 MR_0^2	0.005 MR_0^2 steps
Isostasy Type		Equal-Mass or Equal-, Pressure, Pratt or Airy	
Tide Type		Obliquity or Eccentricity	

*Temperature at which we assume the ice shell transitions from porous to solid.

els' respective best-fit heating patterns. This leaves obliquity tides, indicating that the tidal heating that formed Mimas' shape was due to a high tilt but little-to-no eccentricity.

Focusing on Mimas models that assumed equal-pressure Airy isostasy and obliquity tides, we display the misfits of models with upper ice shell porosity of $\phi = 0.2$ in Figure 3.1. Of these results, 36 of the models fulfilled all of our self-consistency checks. All these best-fit models assumed a moment of inertia of 0.375 MR_0^2 with an assumed average ice shell thickness of about ∼30 km (where the upper ∼30% is porous). This thickness of an ice shell requires an average surface heat flow of ∼20 mW m^{-2} (for a total power of 10 GW, comparable to the tidal power expected for present-day Enceladus,

Table 3.2: Spherical Harmonic Coefficients of a particularly well-fitting and self-consistent model of Mimas where $d_0 = 28$ km, $\phi = 0.2$, $C = 0.375\ MR_0^2$, $T_B = 270$ K, and the ice shell is undergoing equal-pressure Airy isostasy and obliquity tides.

Degree l	2		4		
Order m	0	2	0	2	4
Observed Shape[a] $H_{l,m}^{obs}$ (km)	-7.74	1.83	0.290	0.0172	0.00163
Hydrostatic Shape[b] $H_{l,m}^{hyd}$ (km)	-7.20	2.28			
Residual Topography[c] $H_{l,m}^{res}$ (km)	-0.54	-0.45	0.290	0.0172	0.00163
Shell Thickness[d] $d_{l,m}$ (km)	-3.64	-3.05	1.95	0.116	0.00110
Basal Topography[e] $H_{l,m}^{bas}$ (km)	3.10	2.60	-1.66	-0.0986	-0.00934
Surface Temperature[f] $T_{l,m}$ (K)	-8.69		-1.29		
Basal Heat Flux[g] $F_{l,m}^{b}$ (mW m^{-2})	4.04	2.20	-0.655	-0.0155	0.00253

[a]Unnormalized from Nimmo et al. (2011)
[b]Calculated with Equations 2.3 and 2.4
[c]$H_{l,m}^{res} = H_{l,m}^{obs} - H_{l,m}^{hyd}$
[d]Calculated with a form of Equation 2.9 that accounts for shell porosity (Chapter 2 Gyalay and Nimmo, 2023)
[e]$H_{l,m}^{bas} = H_{l,m}^{res} - d_{l,m}$
[f]Calculated using Nadeau and McGehee (2017). $T_{6,0} = 0.174$ K
[g]Multiply by $\left(\frac{R_0 - d_0}{R_0}\right)^2$ for surface heat flow

Hemingway and Mittal, 2019). We include the spherical harmonic coefficients of various parameters for a particularly successful model in Table 3.2.

In the standard visco-elastic model (e.g., Peale and Cassen, 1978; Wisdom, 2004), the total power dissipated by tides $\dot{E}$ in a synchronous satellite is related to that satellite's obliquity θ and orbital eccentricity e by Equation 2.30, for a satellite's tidal Love number k_2, tidal quality factor Q, angular rotational frequency ω, radius R_0, and Newton's gravitational constant G. By convention, obliquities are measured relative to a precessing reference frame where, for a positive inclination, satellites in the first Cassini State (see Section 3.4.2) have negative obliquities (e.g., Peale, 1969). For Mimas' current eccentricity $e = 0.02$ then, the obliquity θ would need to be -3°

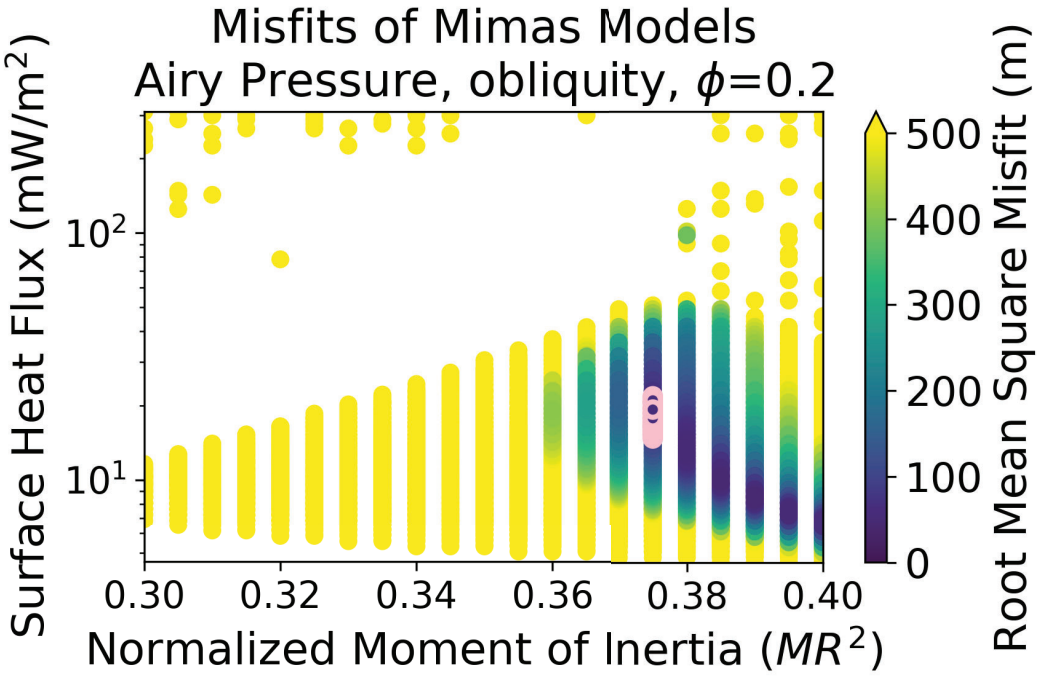

Figure 3.1: For each isostasy and tide type combination, we varied the parameters of upper layer porosity, average total conductive ice shell thickness, average temperature at the base of the ice shell, and Mimas' moment of inertia (Table 3.1), where each combination of parameters is represented by a colored dot. Here, we present results for models that assumed equal-pressure Airy isostasy, obliquity tides, and an upper shell porosity of $\phi = 0.2$. All varied parameters except the moment of inertia are captured in the average heat flux. The color/brightness of the dot indicates the root mean square (RMS) goodness of fit, where the lower RMS (darker purple hues) are better fits. Results with lower RMS values have been plotted over results of higher RMS values to better highlight which heat fluxes and moments of inertia result in the best fits to observed topography. Results that satisfy the self-consistency constraints (Chapter 2, Gyalay and Nimmo, 2023) are circled in pink, and are thus our best-fit models of Mimas. We can then conclude that Mimas needs a normalized moment of inertia 0.375 MR_0^2 and a surface heat flux of 20 $mW\ m^{-2}$ for a tidal heating pattern to be responsible for ice shell thickness variations.

for the power of obliquity tides to be equivalent to the power of eccentricity tides, or $-\theta > 9^\circ$ for obliquity tides to overpower eccentricity tides by at least a factor of 10. Mimas' obliquity has not been measured (the only icy satellite with a measured obliquity is Titan, see Stiles et al., 2008), but even -3° is far greater in magnitude than the value of $\theta = -0.04^\circ$ estimated by Chen et al. (2014) under the assumption that Mimas is in a Cassini State (defined in subsection 3.4.2). This may imply that the tidal heating pattern we infer from topography may have been from *before* Mimas gained its eccentricity, perhaps during some period of high obliquity after which the resulting ice shell thickness variations froze in. We discuss this issue further below and in the next section.

How well a satellite dissipates its heat tidally is captured in the ratio k_2/Q in Equation 2.30. We would need to know this ratio's value in order to better estimate the obliquity required to dissipate a given tidal power. As this has not been measured for Mimas, we begin with a value $k_2/Q = 0.01$ as an upper bound estimate (assuming Mimas is as dissipative as Io or Enceladus; Lainey et al., 2009; Nimmo et al., 2018, respectively, as references for Io and Enceladus's k_2/Q) to find that a tidal dissipation $\dot{E} \approx 10$ GW within Mimas requires a minimum obliquity $-\theta > 0.42^\circ$ when assuming no eccentricity tides.

Curiously, the tidal heating pattern of our best-fit Mimas does not immediately appear to agree with our assumed parameters—namely, the assumption of a ∼30 km thick ice shell operating under Airy isostasy. Across the 36 self-consistent best-fit results in Figure 3.1, we found that the inferred heating pattern weights (χ_A, χ_B, χ_C)

$(0.269 \pm 0.009,\ 0.463 \pm 0.007,\ 0.267 \pm 0.016)$. This does not immediately indicate an ocean world with weights $\left(\frac{2}{11},\ 0,\ \frac{9}{11}\right)$ as one would expect from the fact that our best-fits assumed Airy isostasy. In fact, each individual heating pattern weight would seem to indicate a different radius of Mimas' interior (everything beneath the ice shell) relative to its total radius regardless of whether we assume a rigid or fluid interior (Figure 2.4). Instead, it appears that in addition to some fraction of the total heating due to tidal heat produced within the ice shell χ_T, the inferred heating pattern includes some fraction of the total heating that is due to a uniform background heat flux χ_U with pattern $(0.2,\ 0.4,\ 0.4)$ and/or some fraction of the total heating due to tidal heating of the core χ_H with heating pattern $(0.13,\ 0.31,\ 0.56)$. Writing this as an equation,

$$\begin{bmatrix} 0.269 \\ 0.463 \\ 0.267 \end{bmatrix} = \chi_T \begin{bmatrix} \chi_{A,T} \\ \chi_{B,T} \\ \chi_{C,T} \end{bmatrix} + \chi_U \begin{bmatrix} 0.2 \\ 0.4 \\ 0.4 \end{bmatrix} + \chi_H \begin{bmatrix} 0.13 \\ 0.31 \\ 0.56 \end{bmatrix}, \tag{3.4}$$

where $\chi_T + \chi_U + \chi_H = 1$. We subtract the heating patterns due to a uniform pattern or due to core heating with increasing factors χ_U and χ_H, respectively, until the three heating pattern weights due only to tidal heating in the shell converge on a single interior radius (as seen in Figure 2.4). We find the remaining heating pattern weights are $(0.338,\ 0.533,\ 0.127)$; which is indicative of tidal heating within an ice shell atop a *rigid* interior for an shell thickness of 28.5% the satellite's total radius, or 56 km thick for Mimas. There is no solution if we assume the ice shell is atop a fluid layer. The tidal heating pattern we infer from Mimas' topography suggests that $49.1 - 67.4\%$ of Mimas' total heat is produced by tidal heating within its ice shell, where the remainder

is some combination of up to 50.9% from a uniform background heat flux and up to 32.6% from the tidal heat produced within Mimas' core. The fractions of the pattern due to a uniform background heat flux or tidal heating in the core can trade off linearly such that $\chi_H = 0.326 - 0.638\chi_U$ for $\chi_U \leq 0.509$.

The low bulk density of Mimas combined with our assumed moment of inertia imply the interior of Mimas beneath its ∼30 km ice shell has a density of ∼1300 kg m^{-3}. With such a low density, it is unlikely Mimas has enough rock for radioactivity to produce a significant background heat flux. This makes it more likely that the portion of the inferred heat distribution not due to tidal heating within the shell is due to tidal heating within the core. With a density of 1300 kg m^{-3}, the core is ∼ 80% ice by volume and can easily provide the appropriate fraction of tidal heating while still being colder (and importantly, more rigid) than the ice shell (e.g., Roberts, 2015).

The seemingly larger issue is the apparent mismatch between an assumed ice shell thickness of ∼30 km operating under Airy isostasy over a layer which is implicitly more fluid and an inferred ice shell thickness of 56 km atop a *rigid* interior implied by the inferred tidal heating pattern weights. In order to satisfy both constraints we posit that during the epoch of tidal heating that produced Mimas' present ice shell thickness variations, Mimas' ice shell was split into an upper, conductive layer with ∼ 30 km thickness and a deeper, convective layer that brings the total ice shell thickness to 56 km. The warmer, convective ice layer fulfills three purposes: it acts as the "fluid" layer that enables the conductive ice shell thickness to vary according to Airy isostasy, its contribution to tidal heating would lead to the tidal heating distribution of a thicker ice

shell as predicted by the inferred tidal heating pattern weights, and, finally, it transports tidal heat produced in Mimas' core to the conductive ice shell. While Mimas' core produces $33 - 51\%$ of the total tidal heating, it does not need to be as warm (or have as low a viscosity) as the ice shell to produce this amount of tidal heating. Further, the inclusion of rock within the core will raise its rigidity, explaining why the tidal heating pattern indicates a rigid interior. A weakly-convecting layer can also explain why a significant factor of Mimas total heating pattern could be due to a uniform heating pattern, as it could partially redistribute the tidal heating signature of core heating into a uniform heating pattern.

For a convective ice shell layer to be feasible within this ancient Mimas, it would have to be far more efficient at transporting heat out of Mimas than simple conduction. To examine this, we use the Rayleigh number Ra, which is the ratio of the timescale for conductive heat flow to the timescale for advective heat flow. Thus, the higher this ratio, the more likely a given regime is to be convective. The Rayleigh number can be calculated,

$$\mathrm{Ra} = \frac{\alpha_0 g_S \rho_C \Delta T d_0^3}{\eta \kappa}, \tag{3.5}$$

where α_0 is the volumetric thermal expansivity, g_S is the surface gravity, ρ_C is the shell density, ΔT is the temperature contrast at the top and bottom of the ice shell, η is the dynamic viscosity at the base of the ice shell, and κ is the ice shell's thermal diffusivity. Taking an order of magnitude approach, we can calculate the Rayleigh number of the ice shell using $\alpha_0 \approx 10^{-4}$ K^{-1} (e.g., Röttger et al., 1994), $g_S \approx 6 \times 10^{-2}$ m s^{-2}, $\rho_C \approx 9 \times 10^2$ kg m^{-3}, $\Delta T \approx 2 \times 10^2$ K, $d_0 \approx 6 \times 10^4$ m, $\eta \approx 10^{13}$ Pa s, and $\kappa \approx 10^{-6}$ m^2 s^{-1};

to find Ra$\approx 2 \times 10^7$. Because the ice shell's viscosity depends exponentially upon temperature, we must compare the Rayleigh number calculated in Equation 3.5 for some constant viscosity to the critical Rayleigh number,

$$\mathrm{Ra}_C = 21\,(\gamma \Delta T)^4 \tag{3.6}$$

where γ is the reciprocal of the rheological temperature scale (Solomatov, 1995). For ice, $\gamma \approx 10^{-1}$ K^{-1}, so then $\mathrm{Ra}_C \approx 3 \times 10^6$. As the Rayleigh number we calculated is greater than this value by about a factor of 10, convection is possible but not vigorous. Our interpretation of a thick stagnant lid is consistent with this picture.

We found we could use Roberts and Nimmo (2008)'s numerical solid body tidal heating code (modified to include obliquity tides in Gyalay and Nimmo, 2023) to replicate our inferred tidal heating pattern for a Mimas modeled with a rigid ice-rock core and an ice shell with a lower convective and upper conductive layers, where the upper portion of the conductive layer is porous. We provide the rigidity, viscosity, and density parameters of each layer in Gyalay et al. (2023). Importantly, this interior structure of Mimas is fully solid and thus would *not* have an ocean. The Roberts and Nimmo (2008) model will also numerically calculate Mimas' dissipativity k_2/Q for a given interior structure. In our case, we find $k_2/Q \sim 6 \times 10^{-4}$, as opposed to our previous upper bound of 10^{-2}. Then, to attain $\dot{E} = 10$ GW, we now require an obliquity of $\theta = -1.7°$.

In our models, the convective ice layer is approximated as a mixture of ice and rock, similar to that of the core. This is both to satisfy Mimas' high moment

of inertia and the requirement of Airy isostasy that the compensating layer be denser than the conductive ice shell. In reality, the fraction of rock within the ice shell might increase as a gradient from near the surface to a uniform density core composed of ice and rock. This would be consistent with a weakly differentiated Mimas (cf. a weakly differentiated Callisto, Nagel et al., 2004), which would be inconsistent with a Mimatean ocean. Further, if the convective ice shell has an average density closer to that of the ice-rock core rather than the icy conductive shell, then the basal topography of the conductive ice shell would appear to be the shape of the ice-rock core *including* a convective ice-rock layer. We find that by removing the hydrostatic shape due to a Mimas with $C = 0.375\ MR_0^2$, Mimas has residual topography coefficients of $H_{2,0}^{res}$ that under equal-pressure Airy isostasy imply a basal topography of ~ 6 km along the axis pointing towards Saturn and ~ -12 km pointing along Mimas' orbit (Table 3.2). This would then create an approximately 18 km difference in radius along the two axes. Thus the topography of this convective (now frozen) layer beneath the conductive ice shell could fulfill the "non-hydrostatic core" librational constraint of Tajeddine et al. (2014). This constraint predicts that if Mimas does not have an ocean, it may instead have an elongated core; where the core is 20 km longer in radius on the axis pointing towards Saturn than on the axis pointing forward along Mimas' orbit.

3.4 Implications for Saturn System History

We found that the non-hydrostatic shape of Mimas in even orders of spherical harmonic degrees 2 and 4 may be the product of shell thickness variations in response to obliquity tides. Specifically, a conductive ice shell is in Airy isostasy atop a soft convective shell that is composed of an ice-rock mixture. The convective ice-rock shell is itself tidally heating atop a rigid, interior—where this core is *also* tidally heating. This requires Mimas to have a rather high obliquity and little-to-no eccentricity in its orbit, which is in contrast to the high eccentricity presently observed for Mimas' orbit. We reason, then, that Mimas' current ice shell thickness variations (as inferred from its global shape) may have formed in response to spatial variations in tidal heating that arose during a period of abnormally high obliquity. We provide potential origins for a temporarily high obliquity later in this section. Once the obliquity was no longer excited, it would damp rapidly, allowing Mimas to cool so quickly that its ice-shell thickness variations would have frozen in. Only later might Mimas have gained its current high eccentricity. Does this scenario fit within the dynamical history of the Saturnian system?

3.4.1 A transiently high obliquity

We assume that Mimas is in a Cassini state and would tend towards a given obliquity that depends on Mimas' other orbital parameters (elaborated upon further in the next subsection, Section 3.4.2). Chen et al. (2014), for instance, calculated Mimas'

obliquity should be $\sim -0.04°$, while we infer that Mimas' global shape froze in following tides due to an obliquity $-\theta > 1.7°$. If that high obliquity was only temporary and not due to a Cassini state, it would quickly damp to the value predicted by the Cassini state (e.g., Ward, 1975). The damping timescale of obliquity τ_{obl} (e.g., Bills and Nimmo, 2011; Chen and Nimmo, 2011) can be estimated from the timescale of damping a wobbling rotator to principal axis rotation (Gladman et al., 1996), or,

$$\tau_{obl} = \frac{4\pi G\bar{\rho}\left(\frac{C}{MR_0^2}\right)}{\omega^3\left(\frac{k_2}{Q}\right)}. \tag{3.7}$$

Using our predicted values of $k_2/Q = 6 \times 10^{-4}$ and $C/\left(MR^2\right) = 0.375$ for Mimas, this timescale $\tau_{obl} \sim 40$ yrs—absurdly short in the history of the solar system. Thus, if a high obliquity is not maintained by some external forcing, it will fall to the value predicted by a Cassini state nigh instantaneously.

Freezing in the shell thickness variations then, would require that the timescale of relaxing shell thickness variations be long compared to the timescale of freezing Mimas. Following Nimmo (2004), the timescale to reduce shell thickness variations by a factor of e at a given spherical harmonic degree l is

$$\tau_{relax} = \frac{\eta_B}{\Delta\rho g_S \delta^3}\left(\frac{R_0}{l}\right)^2, \tag{3.8}$$

where η_B is viscosity at the base of the conductive ice shell and g_S is the surface gravity. δ is some lengthscale defined,

$$\delta = \frac{R_G T_B d_0}{Q_A \ln\left(\frac{T_B}{T_S}\right)}, \tag{3.9}$$

where R_G is the universal gas constant $R_G = 8.31$ J mol^{-1} K^{-1}, and Q_A is the activation

energy of ice Q_A=60 kJ mol^{-1}. In general, the temperature-dependent viscosity η is

$$\eta\left(T\right) = \eta_M \exp\left[\frac{Q_A\left(T_M - T\right)}{R_G T_M^2}\right] \tag{3.10}$$

where T_M is the melting temperature of ice. If Mimas' spatial variations in heat flow are no longer maintained this relaxation timescale can be rapid when $T_B \sim T_M$. However, as Mimas' ice shell continues to transport heat out of its interior, the temperature at the base of the conductive ice shell will drop along with the temperature throughout Mimas' core. By inspection of the preceeding three equations, the dependence of the relaxation timescale of isostatic variations τ_{relax} on the temperature at the base of the conductive ice shell T_B is dominated by the term $\exp\left[Q_A\left(T_M - T_B\right)/\left(R_G T_M^2\right)\right]$. Meanwhile, the timescale of cooling Mimas' interior is inversely proportional to the conducted heat flux, which scales roughly linearly with the temperature difference across the conductive ice shell $T_B - T_S$. Thus as Mimas cools, the relaxation timescale grows exponentially as compared to the conduction timescale–allowing the ice shell thickness variations to freeze in. The timescale to settle into isostatic ice shell thickness variations in the first place, meanwhile, is much faster than the timescale to relax away from those same thickness variations (cf., Equation 20 of McKenzie et al., 2000).

While we have shown that we can freeze in Mimas' topographic variations after a period of high obliquity during which ice shell thickness variations rapidly arose, is it reasonable to expect Mimas' obliquity to have ever reached a magnitude $ge1.7°$? To answer that, we examine Mimas' orbital dynamics under the assumption of a Cassini state.

3.4.2 Mimas in a Cassini state

In a Cassini state (an appropriate assumption for dissipative systems; e.g., Peale, 1969; Ward, 1975), there is a direct relation between a satellite's obliquity θ and its inclination i that depends on the satellite's orbital frequency ω and gravitational torques upon the satellite:

$$\frac{3}{2}\frac{\omega}{\dot{\Omega}}\left[(J_2 + C_{2,2})\cos\theta + C_{2,2}\right]\sin\theta = \frac{C}{MR_0^2}\sin(i-\theta), \tag{3.11}$$

where $\dot{\Omega}$ is the precession of the longitude of the ascending node (more concisely: nodal precession), which is a sum of all the gravitational perturbations to the satellite's orbit. Were the shell to be decoupled from the interior by an ocean, $C/\left(MR_0^2\right)$ would instead be closer to the normalized moment of inertia of the ice shell. As we inferred a fully-solid Mimas, we continue with our best fit $C = 0.375\ MR_0^2$. J_2 and $C_{2,2}$, meanwhile, are the spherical harmonic coefficients of the satellite's degree-2 gravity field (where by convention, zonal harmonics of gravity are labeled $J_l = -C_{l,0}$). In addition to spherical harmonic coefficients of shape in Equations 2.3 and 2.4, Beuthe et al. (2016) defines the gravity coefficients of a rapidly-rotating hydrostatic body as a function of another fluid Love number $k_2^F = h_2^F - 1$ as,

$$J_2^{hyd} = \frac{5}{6}k_2^F q\left(1 + \frac{16}{21}h_2^F q\right), \tag{3.12}$$

$$C_{2,2}^{hyd} = \frac{1}{4}k_2^F q\left(1 + \frac{64}{21}h_2^F q\right). \tag{3.13}$$

By dropping the higher order term within the parentheses, the ratio $J_2^{hyd}/C_{2,2}^{hyd}$ can also be readily calculated as its first order approximation, 10/3. While Mimas' gravity

field has not been measured, isostatically-compensated topography variations are not expected to have a significant effect on the satellite's gravity variations. We make the simplifying assumption then that Mimas' degree-2 gravity is that of a rapidly-rotating, hydrostatic satellite.

Mimas' nodal precession $\dot{\Omega}$, meanwhile, depends on the torques on Mimas from Saturn's oblateness as measured by Saturn's gravity coefficient $J_{2,Sat}$, as well as from other moons orbiting Saturn. The term that depends only on Saturn's oblateness is

$$\dot{\Omega}_{Sat} = -\frac{3}{2}\omega J_{2,Sat}\left(\frac{R_{Sat}}{a}\right)^2, \tag{3.14}$$

where R_{Sat} is Saturn's radius (e.g., Murray and Dermott, 1999). Calculating this at Mimas' semi-major axis a, $\omega/\dot{\Omega}_{Sat} \approx -410$, compared to the total observed value $\omega/\dot{\Omega} = -382$, demonstrating that the contribution of Saturn's oblateness dominates Mimas' nodal precession.

The contribution to Mimas' nodal precession from another moon orbiting Saturn $\dot{\Omega}_m$ at a semi-major axis a_m with mass M_m depends on whether that satellite's orbit is interior or exterior to Mimas' a:

$$\dot{\Omega}_{moon} = \begin{cases} -\frac{1}{4}\omega\frac{a_m}{a}\frac{M_m}{M_{Sat}}b^{(1)}_{3/2}\left(\frac{a_m}{a}\right), & \text{for } a_m < a, \\ -\frac{1}{4}\omega\left(\frac{a_m}{a}\right)^2\frac{M_m}{M_{Sat}}b^{(1)}_{3/2}\left(\frac{a}{a_m}\right), & \text{for } a_m > a, \end{cases} \tag{3.15}$$

where $b^j_s(x)$ is a Laplace coefficient as a function of a value $0 < x < 1$ (Murray and Dermott, 1999). As a note, the small contribution from the Sun may be calculated for $M_m = M_{Sun}$ and a_m is Saturn's semi-major axis.

Taking advantage of the fact that both θ and i are expected to be small angles,

we may rearrange and simplify Equation 3.11 to find,

$$\sin\theta \approx \frac{\sin i}{\cos i + \frac{3}{2}\frac{\omega}{\dot{\Omega}}\frac{(J_2+2C_{2,2})}{C/\left(MR_0^2\right)}}. \tag{3.16}$$

This avoids having to solve a transcendental equation with four sets of solutions. For Mimas' currently measured $i = 1.574°$ (higher than many icy satellites due to an inclination-type resonance with Tethys, e.g., Sinclair, 1983; Vienne et al., 1996; Champenois and Vienne, 1999) and $\omega/\dot{\Omega} = -382$, we find its obliquity θ should be about $-0.03°$ using J_2 and $C_{2,2}$ calculated with Equations 3.12 and 3.13, respectively, using our inferred moment of inertia 0.375 MR_0^2. To increase Mimas' obliquity to the high value of $-\theta \geq 1.7°$ for the tidal heating pattern we infer shaped Mimas' present topography, we find by inspecting Equation 3.16 that we must either increase Mimas' inclination i, decrease its semi-major axis a, or increase its nodal precession rate $\dot{\Omega}$.

For instance, Gyalay and Nimmo (2023) suggested that an epoch of obliquity tidal heating may have occurred in Tethys' past when a large, slow impactor struck Tethys and momentarily increased its inclination while forming its largest crater, Odysseus (cf., Zhang and Nimmo, 2012). In that case, inclination only needed to be increased by $\sim 3°$ (to a total of $\sim 4°$), which is quite achievable by such an impact. However, we find that if all else is held constant in Equation 3.16, the inclination can never be high enough to achieve the requisite $-1.7°$ obliquity. Even an inclination of $90°$ only achieves an obliquity of -1.1°. Thus, despite the potential for impacts and previous resonances, it is impossible for an elevated inclination alone to explain an elevated obliquity.

While not explicitly included, the semi-major axis a is an innate part of multiple values in Equation 3.16. As we elaborate upon in Appendix C, however, even the lower obliquity needed to generate 10 GW of power at Saturn's Roche limit (where a satellite would be tidally disrupted) would require an inclination that is impossible to achieve with an impact or inclination-type resonance.

Unsatisfied with the likelihood of increasing Mimas' inclination with an impact (even when its orbit had a smaller semi-major axis), we turn to the last of our three options for momentarily increasing Mimas' obliquity: increasing the precession of the longitude of ascending node. Importantly, this relies on the use of Equation 3.15 to calculate an external perturber's effect on Mimas' orbit. We calculate this perturbation and its consequential effect on Mimas' obliquity (assuming its inclination is held constant) as a function of this perturber's mass and its semi-major axis orbiting Saturn in Figure 3.2. This figure demonstrates that even a 10^{18} kg object ($\sim \frac{1}{10}\times$ Mimas' mass) can increase Mimas' nodal precession rate by more than an order of magnitude, increasing its obliquity to our requisite $-1.7°$, when its semi-major axis is similar to that of Mimas.

The object in Figure 3.2 need not simply be one object, but could be multiple objects with similar semi-major axes whose masses combine to a total of M_m (see Equation 3.15). This is important, because if Saturn's rings formed recently from the tidal disruption of an eccentric satellite (e.g., Wisdom et al., 2022), there may have been at least 10^{21} kg of errant mass orbiting Saturn following the disruption at similar semi-major axes along highly eccentric orbits (already assuming $\geq 90\%$ of the disrupted

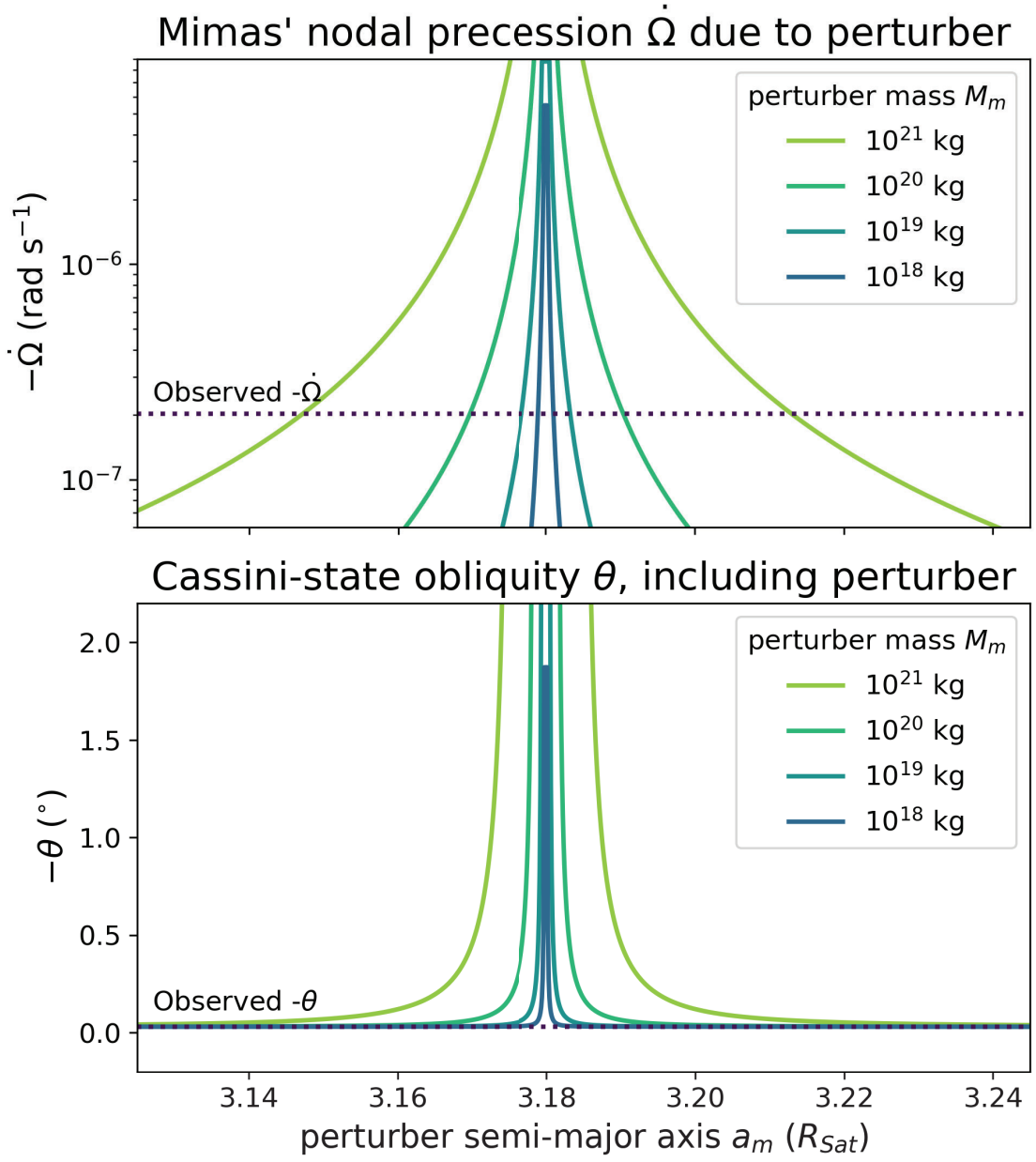

Figure 3.2: (Top) For a given object with mass M_m orbiting Saturn with a semi-major axis a_m, we plot the contribution of this object's perturbation [Brynna]ofto Mimas' [Brynna]nodal precession [Brynna]of longitude of ascending node $\dot{\Omega}$ calculated with Equation 3.15. Depending on the perturber's mass, it can increase Mimas' $\dot{\Omega}$ by orders of magnitude when its semi-major axis approaches Mimas' semi-major axis of 3.18 R_{Sat}. (Bottom) As Mimas' $\dot{\Omega}$ increases in the presence of this perturber, so too does Mimas' obliquity θ.

satellite's mass was ejected from the Saturn system; e.g., Hyodo et al., 2017a). For instance, Hyodo et al. (2017a) modeled the evolution of the debris disc following tidal disruption; in one of their models they assumed 1,000 10^{18} kg chunks orbiting Saturn, each with an eccentricity of 0.98 and an initial semi-major axis of 5×10^9 m ($\sim$86 R_{Sat}). An alternate source of debris that could form Saturn's rings is the collision of two satellites, which would deliver a Mimas-mass worth of material to a similar orbit as Mimas (without necessarily destroying Mimas in the case of a glancing collision, Kegerreis et al., 2023) (cf., Hyodo and Charnoz, 2017). In either case, as the debris disk evolved further, these chunks would collide and break apart, losing energy and decreasing both the semi-major axes and eccentricities of the remaining debris. Some of these (increasingly small) chunks would collide with the Saturnian satellites, while the rest would congregate into small circular orbits as part of Saturn's ring system. It stands to reason then, that there may have been a period of time where enough of this mass had a similar semi-major axis to Mimas (albeit at higher eccentricities and/or inclinations, avoiding impacts) to perturb Mimas' orbital precession. Then, it is only natural that Mimas' obliquity would increase in response to this greater orbital precession (Equations 3.16 and 3.15; Figure 3.2).

A full characterization of how long would-be ring particles took to migrate into the present-day orbits of Saturn's rings would require a dynamical evolution simulation outside the scope of this paper. However, it can be shown that the collisional timescale of chunks following the disruption of a satellite is on the order of 10^5 to 10^7 years (Dones, 1991; Hyodo et al., 2017a), perhaps as low as 10^2 or 10^3 years at Mimas' semi-major

axis (Hyodo et al., 2017a). Thus, whatever migrating ring-forming chunks that shared a semi-major axis with Mimas may stay in their orbits for centuries, non-withstanding replenishment by ring-forming chunks that took longer to migrate that far inward. This timescale aligns well with that required to increase Mimas' obliquity when its nodal precession has increased in response to these ring-forming chunks. That timescale can be approximated by the same timescale for damping from an arbitrary obliquity to the Cassini state obliquity in Equation 3.7, as in both situations Mimas' obliquity trends towards that required by the Cassini state.

3.4.3 In the context of the present-day Saturn system

This recent era of debris disk evolution into Saturn's rings may also explain a similar epoch of transient obliquity tidal heating Gyalay and Nimmo (2023) (Chapter 2) inferred for Tethys. Both moons' obliquities (via orbital precession) may have been excited by the same ring particles to-be as they migrated inwards towards Saturn. Impacts from this debris disc could have formed the large impact basins on both Mimas and Tethys—which may explain their lack of relaxation were these impacts as recent as the formation of Saturn's young rings. Smaller impacts from this debris disc may also have formed the population of small elliptical craters found concentrated on Saturn's moons (e.g., Zahnle et al., 2003; Ferguson et al., 2022), though these may also be the result of unrelated sesquinary impacts. The lack of a similar signature of obliquity tides on Enceladus (whose orbit is between those of Mimas and Tethys) can be dismissed as easily-erased by its significant eccentricity tides.

Mimas' recent eccentricity, meanwhile, could be explained by either the impact that formed Herschel crater (cf. Zhang and Nimmo, 2012) or past mean motion resonances (e.g., Meyer and Wisdom, 2008; Noyelles et al., 2019). If the impact that formed Herschel crater was recent, any eccentricity excited by it may not yet have damped. Likewise, if the Cassini Division within Saturn's rings formed when Mimas and Enceladus entered a mean-motion resonance and migrated inward (Baillié et al., 2019; Noyelles et al., 2019), then this could only have happened within the rings' lifetime–also implying Mimas gained its eccentricity recently. Given the dynamic stability of the Cassini division, it may need to have formed within the last 4-11 Myrs (Baillié et al., 2019), placing an even more-recent constraint on Mimas' eccentricity gain. Either scenario may then explain why Mimas' orbit has not circularized despite the lack of a current resonance to maintain its eccentricity.

If Mimas' eccentricity is enough to maintain a subsurface ocean (e.g., Rhoden and Walker, 2022), why would Mimas' topography (due to ice shell thickness variations in Airy isostasy) not match what one expects for eccentricity tides in an ice shell atop an ocean as observed for Enceladus (cf., Beuthe et al., 2016; Hemingway and Mittal, 2019; Gyalay and Nimmo, 2023)? The answer may lie in the timescale of thermal conduction through Mimas' ice shell. If we take an order of magnitude approach, the timescale for heat to conduct through an ice shell is $\tau_{cond} = d_0^2/\kappa$, where κ is the thermal diffusivity. For ice, $\kappa \sim 10^{-6}$ m^2 s^{-1}. For a 24-31 km thick ice shell atop an ocean as implied by Mimas' libration (Tajeddine et al., 2014), this timescale is approximately 18-30 Myr. Herschel crater's morphology too may be consistent with an impact into an ice shell

atop an ocean, where the ice shell has been thinning over the last 10 (or more) Myr (Denton and Rhoden, 2022). Thus, it is possible that the ice shell thickness and ocean needed to match the libration constraint of Tajeddine et al. (2014) has formed rather recently but has not yet had enough time to overwrite the ice shell thickness variations and topography of the past epoch of high obliquity tides within a solid Mimas as we infer in this paper. A recently gained eccentricity may also explain why it has not yet damped: if Mimas were dissipative enough to generate a subsurface sea, we expect eccentricity to damp on a 50-60 Myr timescale.

However, an ocean is not necessary to explain Mimas' anomalous libration. We demonstrated earlier that the basal topography of the conductive ice shell would imply the denser ice-rock layers beneath it could act as the elongated, non-hydrostatic "core" Tajeddine et al. (2014) predicted as an alternate explanation for Mimas' libration.

Finally, Noyelles et al. (2019) presented two models for how an Enceladus-Mimas resonance may have allowed the satellites to migrate inward and form the Cassini division: one in which Enceladus grew extremely hot, potentially melting, and one in which Mimas instead was extremely hot. Enceladus' required eccentricity in the hot-Enceladus model would threaten the stability of Tethys, but having almost melted would certainly allow Enceladus to have differentiated (Noyelles et al., 2019) as its moment of inertia would imply (Iess et al., 2014). The comparatively-high moment of inertia, 0.375 MR_0^2, we infer for the hydrostatic component of Mimas shape, however, would necessarily imply that Mimas is *not* significantly differentiated—making the hot-Mimas scenario far less likely.

3.5 Conclusions

In this chapter, we demonstrated that the observed long-wavelength topography of Mimas is consistent with a ~ 30 km thick conductive ice shell with Airy-isostatic variations in shell thickness due to the spatial variations in heat flow one would expect of high obliquity tides within a solid Mimas. Below the conductive ice shell was a layer of a weakly convecting ice-rock mixture. As Mimas' obliquity is not currently expected to be high, we infer that this was merely a transient era of high obliquity. Once the obliquity damped, Mimas' ice shell would lose heat faster than its isostatic thickness variations could relax, freezing in this topography. This period of momentarily high obliquity is consistent with an increased precession of Mimas' longitude of ascending node, and may very well have been due to the debris disc of a satellite that was tidally disrupted by Saturn (Wisdom et al., 2022) migrating inward to form Saturn's rings (Hyodo et al., 2017a). While it is strange to infer high obliquity tides when Mimas instead has a high eccentricity, it is likely that Mimas' eccentricity is a more-recent phenomenon due to passage through a mean-motion resonance with another moon (Meyer and Wisdom, 2008), and would have to be recent if Mimas' influence created the Cassini division (Baillié et al., 2019; Noyelles et al., 2019) in Saturn's young rings (Goldreich and Tremaine, 1982; Zhang et al., 2017; Iess et al., 2019; Wisdom et al., 2022). This recently excited eccentricity may have begun melting of a young sub-surface ocean (Rhoden and Walker, 2022) that is consistent with Mimas' libration (Tajeddine et al., 2014) and the morphology of Mimas' largest crater (Denton and Rhoden, 2022). However, the

shape we infer for the ice-rock interior beneath Mimas' conductive ice shell resembles an elongated core that is *also* consistent with the libration measurement (Tajeddine et al., 2014). Our internal structure results are consistent with a solid Mimas both now and in the past, although the timescale of conduction through the ice shell could allow for the existence of an extremely young (less than 10 or so Myr old) ocean. Only a mission to the Saturn system that collects gravity data on Mimas may truly answer if there is a present, recently-formed ocean; but based on our findings of a relatively undifferentiated Mimas and an elongated core, we conclude that an ocean in Mimas is unlikely.

Appendix A

Appendix for Chapter 1

Equation 1.5 allows us to determine the maximum heat flux a region experienced as a function of the depth to pore closure in the crust. However, it also relies on assumptions of the rock types that make up the crust, the rheological constants for each rock type, surface temperature, rock density, thermal conductivity of the rock, and heat production within the rock.

One can find the uncertainty in maximum heat flux as a function of the uncertainties of each variable:

$$\begin{aligned}\delta F_C^2 &= \left(\frac{\partial F_C}{\partial k}\right)^2 \delta k^2 + \left(\frac{\partial F_C}{\partial T_S}\right)^2 \delta T_S^2 + \left(\frac{\partial F_C}{\partial Q}\right)^2 \delta Q^2 + \left(\frac{\partial F_C}{\partial H}\right)^2 \delta H^2 \\ &\quad + \left(\frac{\partial F_C}{\partial A}\right)^2 \delta A^2 + \left(\frac{\partial F_C}{\partial \rho}\right)^2 \delta \rho^2 + \left(\frac{\partial F_C}{\partial n}\right)^2 \delta n^2. \end{aligned} \tag{A.1}$$

Taking each partial derivative of Equation 1.5 and inserting it into Equation A.1, we find the uncertainty to be:

$$\begin{aligned}\delta F_C^2 &= F_C^2\left(\frac{\delta k}{k}\right)^2 + \left(\frac{k}{z}\right)^2 \delta T_S^2 + \left(F_C + \frac{kT_S}{z}\right)^2 \left(\frac{\delta Q}{Q}\right)^2 + \left(\frac{\rho z}{2}\right)^2 \delta H^2 \\ &\quad + \frac{\left(F_C + \frac{kT_S}{z} - \frac{\rho H z}{2}\right)^2}{\ln\left(\frac{tP^n A}{\ln(\phi_0/\phi_C)}\right)^2}\left[\left(\frac{\delta A}{A}\right)^2 + \left(\frac{n}{\rho} + \frac{Hz}{2}\right)^2 \delta\rho^2 + \ln(P)^2 \delta n^2\right]. \quad \text{(A.2)}\end{aligned}$$

By inspecting Equation A.2, one can see that the variables whose individual uncertainties have the largest effect upon the total uncertainty are the thermal conductivity k, the surface temperature T_S, and the activation energy Q.

Appendix B

Supporting Information for Chapter 2

B.1 Introduction

This supporting information serves to detail the math behind the equations we use in the models within our paper. In addition, we detail our results for Enceladus, a moon that is not the focus of our paper but serves to show the efficacy of our model in a situation for which we already know the answer. To begin, we repeat the methodology from Thomas and Dermott (1991) with updated data for a comparison to our results.

B.2 Thomas & Dermott (1991)'s Method

Using Voyager data, Thomas and Dermott (1991) made conclusions about Tethys' internal structure from its shape. Namely, they estimated Tethys had a MoI between 0.17-0.35 MR^2 and a mantle with a bulk density less than that of water ice. We present the formulae they used, such that we may use updated data to make better

conclusions that we can compare to our model's results.

The primary aspect of Tethys' shape used is the difference between the longest and shortest radii of Tethys (assuming a triaxial ellipsoid), $a-c$. In 1991, this was estimated to be 9.8±1.9 km, but is now constrained to 12.2±0.4 km (Nimmo et al., 2011). Tethys' bulk density ρ was assumed to be 1000 kg m^{-3} while we use 984±3 kg m^{-3}. Tethys' radius R_0 was then known to be 529.8±0.8 km but has been updated to 531.1±0.6 km. Along with the orbital frequency ω, we can calculate the ratio m of rotational to gravitational forces:

$$m = \frac{4\omega^2}{4\pi G\rho}. \tag{B.1}$$

This can then be used to calculate H, a factor that depends on the internal distribution of Tethys' density and is of order unity for a homogenous satellite:

$$H = \frac{a-c}{5mR_0}. \tag{B.2}$$

Finally, we can find a probable range of normalized MoI C/MR^2 that depends on H to be

$$\frac{2}{3}\left(1-\frac{2}{5H}\right) < \frac{C}{MR^2} < \frac{2}{3}\left(1-\frac{2}{5}\sqrt{\frac{2}{H}-1}\right), \tag{B.3}$$

where the lower bound assumes a point-core of infinite density, and the upper bound is the Darwin-Radau relation.

For updated values Tethys' parameters, we find H to be 0.85±0.03. Using the most extreme values of $H = 0.82$ and 0.88, we find an updated expected MoI range of 0.34-0.37 MR^2 from Thomas and Dermott (1991)'s methodology.

B.3 Surface temperature and Fourier's law for icy satellites

After removing the effects of rotation and tidal stretching from a satellite's topography, we can focus on the last two sources of topography we are considering: surface temperature and basal heat flux. We assume topography is due to present-day tidal heating and approximate tidal heating as heat flux through the base of the ice shell.

Given the bolometric Bond albedo A_{BB} of a planetary body, as well as its average distance from the sun a, we can compute the average surface temperature of that body:

$$T_{S,0} = \left[\frac{(1 - A_{BB})L_{\text{Sun}}}{16\pi\sigma_{SB}a^2}\right]^{1/4}, \tag{B.4}$$

where L_{Sun} is the solar luminosity, and σ_{SB} is the Stefan-Boltzmann constant. This assumes the planetary body is a black body of emissivity $\varepsilon \sim 1$.

Per Nadeau and McGehee (2017), the solar insolation upon a body whose host planet has an obliquity i varies as a 6th-degree polynomial σ_6 across a surface, and thus the surface temperature T_S varies accordingly:

$$T_S = T_{S,0}\sigma_6^{1/4}. \tag{B.5}$$

For latitude $\Theta = \frac{\pi}{2} - \theta$:

$$\sigma_6(\Theta, i) = 1 - \frac{5}{8}p_2(\cos i)p_2(\sin\Theta) - \frac{9}{64}p_4(\cos i)p_4(\sin\Theta) - \frac{65}{1024}p_6(\cos i)p_6(\sin\Theta), \tag{B.6}$$

where p_k are ordinary Legendre polynomials.

From surface temperature, one can determine basal heat flux given an average basal temperature and ice shell thickness using Fourier's law. The small radius of Tethys necessitates a formulation of Fourier's law that accounts for the spherical geometry of these bodies. We wished also to account for a temperature-dependent thermal conductivity $k = \frac{k_0}{T}$ (Klinger, 1980). It is essential to use a proper version of Fourier's law as we use it not only to determine average basal heat flux, but also in determining the basal heat flux distribution in Airy isostasy.

We begin from a differential form of Fourier's law for a total power H input into a slab of cross-sectional area A that varies as a function of distance from the center of a sphere r:

$$H = -k(T)A(r)\frac{dT}{dr}. \tag{B.7}$$

For a simple slab of constant A and k, $H = AF$ where F is the heat flux. Then Equation B.7 readily yields the classic form of Fourier's equation:

$$F = -k\frac{(T_S - T_B)}{d}. \tag{B.8}$$

For a temperature-dependent $k = k_0/T$ and spherical layer cross section $A(r) = 4\pi r^2$:

$$\frac{H}{4\pi r^2}dr = -\frac{k_o}{T}dT. \tag{B.9}$$

We integrate on both sides, knowing that $H = F_0 4\pi(R-d)^2$ for an average basal heat flux F_0. This yields our calculation of flux:

$$F = \frac{-k_0 \ln\frac{T_S}{T_B}}{d(1-\frac{d}{R})}. \tag{B.10}$$

In addition to using a spherical geometry, it is also useful to account for an outer porous-ice layer. Ice of porosity ϕ has a lower thermal conductivity k_p than that of solid ice (Shoshany et al., 2002):

$$k_{0,p}(\phi) = k_0(1 - \frac{\phi}{0.7})^{4.1\phi+0.22}, \tag{B.11}$$

which increases the required heat flux to maintain the same temperature difference across the same ice shell thickness. The porosity of the outer layer and thickness of both layers are constrained by the range in possible moments of inertia of the satellite.

To account for the porous layer, we again reformulate Fourier's law. Let there be a boundary between the porous layer and solid layer where the temperature reaches that where porous ice anneals, T_A. The derivation of Fourier's law for either spherical shell layer follows as the previous derivation for a single layer. For a lower boundary 1 and upper boundary 2, the power conducted by the moon can be described:

$$\frac{H}{4\pi}\Big(\frac{1}{R_1} - \frac{1}{R_2}\Big) = -k_0 \ln\frac{T_2}{T_1}. \tag{B.12}$$

We then arrive at two equations describing Fourier's Law for each layer, and one equation for Fourier's law across both layers:

$$F_0(R_0 - d)^2 = \frac{-k_{0,p}\ln(T_S/T_A)}{\frac{1}{R_0-L} - \frac{1}{R_0}} \text{ (Upper porous layer)} \tag{B.13}$$

$$F_0(R_0 - d)^2 = \frac{-k_0\ln(T_A/T_B)}{\frac{1}{R_0-d} - \frac{1}{R_0-L}} \text{ (Lower solid layer)} \tag{B.14}$$

$$F_0(R_0 - d)^2 = \frac{-\ln(T_S/T_B)}{\frac{1}{k_{0,p}}(\frac{1}{R_0-L} - \frac{1}{R_0}) + \frac{1}{k_0}(\frac{1}{R_0-d} - \frac{1}{R_0-L})} \text{ (Both layers together)} \tag{B.15}$$

where here L is the thickness of the porous layer. Equations B.13 and B.14 can be rearranged and combined to also yield equation B.15. For a porosity of $\phi = 0$, equation

B.15 reduces to the previously derived Fourier's law for a single-layered ice shell, equation B.10.

To solve for F given d, we can rearrange Equation B.13 as:

$$\frac{1}{R_0 - L} = \frac{1}{R_0} - \frac{k_{0,p} \ln(T_S/T_A)}{F(R_0 - d)^2} \tag{B.16}$$

which we substitute into Equation B.14. We proceed to solve for F:

$$F(R_0 - d)^2 = \frac{-k_0 \ln(T_A/T_B)}{\frac{1}{R_0 - d} - \frac{1}{R_0} + \frac{k_{0,p} \ln(T_S/T_A)}{F(R_0 - d)^2}} \tag{B.17}$$

$$F(R_0 - d)^2 \Big[\frac{1}{R_0 - d} - \frac{1}{R_0}\Big] + k_{0,p} \ln(T_S/T_A) = -k_0 \ln(T_A/T_B), \tag{B.18}$$

before finally simplifying to:

$$F = \frac{-k_0 \ln(T_A/T_B) - k_{0,p} \ln(T_S/T_A)}{(R_0 - d)\big[1 - \frac{R_0 - d}{R_0}\big]}. \tag{B.19}$$

Now that we know the flux at the base of an ice shell with thickness d and upper layer porosity ϕ, we can also solve for the thickness of just that porous region, L. We simply begin from Equation B.16 and rearrange to find:

$$L = R_0 - \frac{1}{\frac{1}{R_0} - \frac{k_{0,p} \ln(T_S/T_A)}{F(R_0 - d)^2}}. \tag{B.20}$$

B.4 Isostasy in icy satellites

Isostasy is the principle that the pressure at depth is constant (Hemingway and Masuyama, 2017). Using Airy isostasy the ice shell thins and is compensated from below by an ocean. The following equation from our paper calculates the change in ice

shell thickness required to yield a given topography h under Airy isostasy:

$$\Delta d = h\Big(1 + \frac{\rho_C}{\Delta\rho}\frac{g_S}{g_B}\Big). \tag{B.21}$$

In contrast to Airy isostasy, Pratt isostasy relies on changes in the crustal density to generate topography. If the crustal density changes by $\delta\rho$, the topography changes by h. Beginning as Hemingway and Masuyama (2017) did, we hold the pressure at depth constant:

$$\rho_C \int_{R_0-d}^{R_0} g(r)dr = (\rho_C + \delta\rho) \int_{R_0-d}^{R_0+h} g(r)dr, \tag{B.22}$$

which can be rearranged to

$$\delta\rho \int_{R_0-d}^{R_0+h} g(r)dr = -\rho_C \int_{R_0}^{R_0+h} g(r)dr. \tag{B.23}$$

For topography h that is $\ll R$, the gravity is nearly constant at g_S from R to $R+h$, so the right hand side of the equation becomes $\simeq -\rho_C g_S h$. We apply the same approximation to the upper portion of the left hand side to find

$$-(\rho_C + \delta\rho)g_S h \simeq \delta\rho \int_{R_0-d}^{R_0} g(r)dr. \tag{B.24}$$

Then we use

$$g(r) = \frac{4\pi G}{r^2}\int_0^r r'^2\rho(r')dr', \tag{B.25}$$

and assume that density varies in a stepwise manner:

$$\rho(r') = \begin{cases} \rho_{\text{core}}, & \text{if } r' < R_0 - d, \\ \rho_C, & \text{if } R_0 - d < r' < R_0, \end{cases} \tag{B.26}$$

where core density ρ_{core} can be found from bulk density $\bar{\rho}$ and crustal density ρ_C. This follows the assumption that topography $h \ll d$, and thus $R_0 + h \sim R_0$, $\rho_C + \delta\rho \sim \rho_C$, and $d \sim d_0$. Then

$$
\begin{aligned}
-(\rho_C + \delta\rho) g_S h &\simeq \delta\rho \int_{R_0-d_0}^{R} \frac{4\pi G}{r^2} \int_0^r r'^2 \rho(r') dr' dr && \text{(B.27)} \\
&= \delta\rho 4\pi G \int_{R_0-d_0}^{R} \left[\int_0^{R_0-d_0} r'^2 \rho_{\text{core}} dr' + \int_{R_0-d_0}^{r} r'^2 \rho_C dr' \right] \frac{dr}{r^2} && \text{(B.28)} \\
&= \delta\rho 4\pi G \int_{R_0-d_0}^{R_0} \left[\frac{(R_0-d_0)^3}{3} \rho_{\text{core}} + \frac{r^3 - (R_0-d_0)^3}{3} \rho_C \right] \frac{dr}{r^2} && \text{(B.29)} \\
&= \delta\rho \frac{4\pi G}{3} \left[\int_{R_0-d_0}^{R} \frac{(R_0-d_0)^3}{r^2} \rho_{\text{core}} dr + \int_{R_0-d_0}^{R_0} r \rho_C dr \right. \\
&\qquad \left. - \int_{R_0-d_0}^{R_0} \frac{(R_0-d_0)^3}{r^2} \rho_C dr \right] && \text{(B.30)} \\
&= \delta\rho \frac{4\pi G}{3} \left[\frac{-(R_0-d_0)^3 \rho_{\text{core}}}{r} + \frac{r^2 \rho_C}{2} + \frac{(R_0-d_0)^3 \rho_C}{r} \right] \Bigg|_{R_0-d_0}^{R_0} && \text{(B.31)} \\
&= \delta\rho \frac{4\pi G}{3} \left[(\rho_C - \rho_{\text{core}})(R_0-d_0)^3 \left(\frac{1}{R_0} - \frac{1}{R_0-d_0} \right) \right. \\
&\qquad \left. + \frac{\rho_C}{2} \left(R_0^2 - (R_0-d_0)^2 \right) \right]. && \text{(B.32)}
\end{aligned}
$$

In the limit of $d_0 \ll R_0$ this equation simplifies to $\frac{4}{3}\pi G\rho_m R_0 d_0\ \delta\rho$ as required.

Distributing terms and remembering that $g_B = \frac{4\pi}{3}\rho_{\rm core}(R_0 - d_0)G$

$$\begin{aligned} -(\rho_C + \delta\rho)g_S h \ &\simeq\ \delta\rho\Bigg\{\frac{4\pi G}{3}(R_0 - d_0)^2\rho_{\rm core} \\ &\qquad +\frac{4\pi G}{3}(R_0 - d_0)^3\Big(\frac{\rho_C}{R_0} - \frac{\rho_{\rm core}}{R_0} - \frac{\rho_C}{R_0 - d_0}\Big) \\ &\qquad +\rho_C\frac{2\pi G}{3}\big[R_0^2 - (R_0 - d_0)^2\big]\Bigg\} \qquad \text{(B.33)} \\ &=\ \delta\rho\Bigg\{g_B(R_0 - d_0) + \frac{4\pi G}{3}(R_0 - d_0)^3\Big(\frac{\rho_C}{R_0} - \frac{\rho_{\rm core}}{R_0} - \frac{\rho_C}{R_0 - d_0}\Big) \\ &\qquad +\rho_C\frac{2\pi G}{3}\big[R_0^2 - (R_0 - d_0)^2\big]\Bigg\}. \qquad \text{(B.34)} \end{aligned}$$

Recalling $g_S = \frac{4\pi G}{3R^2}\{(R_0 - d_0)^3\rho_{\rm core} + [R_0^3 - (R_0 - d_0)^3]\rho_C\}$, we add and then subtract $\frac{4\pi G}{3R_0}R_0^3\rho_C\delta\rho$ from the right hand side to find

$$\begin{aligned} -(\rho_C + \delta\rho)g_B h \simeq \delta\rho\Bigg\{ &\ g_S(R_0 - d_0) - g_S R_0 - \frac{4\pi G}{3}\rho_C(R_0 - d_0)^2 + \frac{4\pi G}{3}\rho_C R_0^2 \\ &+\rho_C\frac{2\pi G}{3}\big[R_0^2 - (R_0 - d_0)^2\big]\Bigg\}, \qquad \text{(B.35)} \end{aligned}$$

which finally reduces to

$$-(\rho_C + \delta\rho)g_S h \simeq \delta\rho\{g_B(R_0 - d_0) - g_S R_0 + 2\pi G\rho_C[(R_0)^2 - (R_0 - d_0)^2]\}. \qquad \text{(B.36)}$$

We can then rearrange our equation and find the change in crustal density required to generate the topography:

$$\delta\rho \simeq \frac{-\rho_C h}{\frac{g_B}{g_S}(R_0 - d_0) - R_0 + \frac{2\pi G}{g_S}\rho_C[R_0^2 - (R_0 - d_0)^2]}. \qquad \text{(B.37)}$$

B.5 Tidal heating from topography

We approximate tidal heating within a moon as the basal heat flux at the bottom of the moon's ice shell. As such, we may use Fourier's law and the principles of isostasy in order to infer the basal heat flux distribution.

As topography is the direct result of the ice shell thinning and thickening in Airy isostasy, we may use Fourier's law to calculate the change in basal heat flux. We begin with an average ice shell thickness and average basal temperature. We use Equation 2.9 to find the change in shell thickness from topography, and use the following equation from our paper to find the basal heat flux distribution:

$$F = \frac{-k_0 \ln(T_A/T_B) - k_{0,p} \ln(T_S/T_A)}{(R_0 - d)(1 - \frac{R_0 - d}{R_0})}. \tag{B.38}$$

Under Pratt isostasy, the topography is the result thermal expansion and contraction. Let there be an average ice shell temperature in a region, $\bar{T} = \frac{T_S + T_B}{2}$. Then using a temperature-dependent thermal expansivity of water ice $\alpha(T)$ (Röttger et al., 1994), the change in volume ΔV of a region from average is

$$\frac{\Delta V}{V} = \alpha_0 \Delta \bar{T}, \tag{B.39}$$

where α_0 is the thermal expansivity of water ice for the reference average temperature of the ice shell $\bar{T}_0$, $\Delta \bar{T} = \bar{T}_0 - \bar{T}$, and $\bar{T} = \frac{1}{2}(T_S + T_B)$.

For a given location, the change in ice shell volume is related to the change in shell density $\delta\rho$ from average crustal density ρ_C:

$$\frac{\Delta V}{V} = \frac{-\delta\rho}{\rho_C + \delta\rho}, \tag{B.40}$$

where $\delta\rho$ is a function of topography h (Equation B.37).

From Equation B.10 for a single-layer, solid ice shell,

$$T_B = T_S e^{F(d-d^2/R)/k_0}. \tag{B.41}$$

Let $d' = d_0 - \frac{d_0^2}{R_0}$, then

$$\begin{aligned}
\Delta\bar{T} &= \frac{1}{2}[\Delta T_S + (T_S e^{Fd'/k_0} - T_{S,0} e^{F_0 d'/k_0})] && \text{(B.42)}\\
&= \frac{1}{2}[\Delta T_S + (T_S e^{F_o d'/k_0} e^{\Delta F d'/k_0} - T_{S,0} e^{F_0 d'/k_0})] && \text{(B.43)}\\
&= \frac{1}{2}[\Delta T_S + e^{F_0 d'/k_0}(T_S e^{\Delta F d'/k_0} - T_{S,0})], && \text{(B.44)}
\end{aligned}$$

where ΔT_S is the variation in surface temperature T_S from the reference value $T_{S,0}$ and ΔF is the variation in basal heat flux F from the reference value F_0. Then, substituting $\Delta\bar{T}$ into equation B.39, we rearrange to find the change in basal flux ΔF required to yield the inferred density change $\delta\rho$:

$$\Delta F = \frac{k_0}{d'} \ln\Big(\frac{1}{T_S}\Big\{T_{S,0} + e^{-F_0 d'/k_0}\Big[\frac{2}{\alpha_0}\frac{(-\delta\rho)}{\rho_C + \delta\rho} - \Delta T_S\Big]\Big\}\Big). \tag{B.45}$$

For an ice shell with an upper porous layer, we assume an expansivity that is a volume-weighted average of the expansivities for the porous and solid ice layers. We assume the pore-spaces do not expand with the ice and thus substitute α_0 with α_0'

$$\alpha_0' = \alpha_0\left[\frac{V_{0,p}}{V_0}(1-\phi) + \frac{V_{0,s}}{V_0}\right], \tag{B.46}$$

where $V_{0,p}$, $V_{0,s}$, and V_0 are volumes of the porous ice shell, solid ice shell, and total ice shell, respectively. We also substitute $\frac{d'}{k_0}$ with $(\frac{d'}{k_0})'$ appropriate for a two layer system:

$$(\frac{d'}{k_0})' = (R_0 - d_0)^2\Big[\frac{1}{k_{0,p}}\Big(\frac{1}{R_0 - L_0} - \frac{1}{R_0}\Big) + \frac{1}{k_0}\Big(\frac{1}{R_0 - d_0} - \frac{1}{R_0 - L_0}\Big)\Big]. \tag{B.47}$$

The final formula for change in heat flux from topography using Pratt isostasy with an upper porous layer is thus

$$\Delta F = \frac{1}{(\frac{d'}{k_0})'} \ln\Big(\frac{1}{T_S}\Big\{T_{S,0} + e^{-F_0(d'/k_0)'}\Big[\frac{2}{\alpha_0'}\frac{(-\delta\rho)}{\rho_C+\delta\rho} - \Delta T_S\Big]\Big\}\Big). \tag{B.48}$$

This equation reduces to Equation B.45 for $\phi = 0$.

B.6 Multi-linear Regression

As tidal heating can be decomposed into the *linear* combination of basis heating patterns, we can perform a multilinear regression upon the heating pattern inferred from topography. We begin by arranging the heat flux distribtuiont F_T (Equation 2.22),

$$F_T(\theta,\lambda) = \frac{F_{0,T}}{\psi_0}(\chi_A\psi_A + \chi_B\psi_B + \chi_C\psi_C),$$

to be in terms of harmonic functions ψ_l rather than angular functions ψ_J. We find

$$\frac{F(\theta,\lambda)}{F_0}a_{0,0} = \Big(\chi_A+\chi_B+\chi_C\Big)\psi_0+\Big(\chi_A+\frac{1}{2}\chi_B-\chi_C\Big)\psi_2+\Big(\chi_A-\frac{2}{3}\chi_B+\frac{1}{6}\chi_C\Big)\psi_4. \tag{B.49}$$

Composing $F(\theta,\lambda)$ as a series of spherical harmonics, we can derive heat flux coefficients $C^F_{l,m}$ from $F(\theta,\lambda)$. Then, because spherical harmonic functions are orthogonal, we can drop the associated Legendre functions and cosines within $F(\theta,\lambda)$ and ψ_l in equation B.49 to retrieve

$$\frac{a_{0,0}}{a_{l,m}}\frac{C^F_{l,m}}{F_0} = \begin{cases} \chi_A + \frac{1}{2}\chi_B - \chi_C, & \text{if } l = 2, \\ \chi_A - \frac{2}{3}\chi_B + \frac{1}{6}\chi_C, & \text{if } l = 4, \end{cases} \tag{B.50}$$

where $a_{l,m}$ come from Table 1 in the main text, and depend if we assume eccentricity or obliquity tides. Recall that $\chi_A + \chi_B + \chi_C = 1$. We reformulate this set of equations in matrices to solve with linear algebra:

$$\begin{bmatrix} (\frac{a_{0,0}}{a_{2,0}}\frac{C^F_{2,0}}{F_0} - 1) \\ (\frac{a_{0,0}}{a_{2,2}}\frac{C^F_{2,2}}{F_0} - 1) \\ (\frac{a_{0,0}}{a_{4,0}}\frac{C^F_{4,0}}{F_0} - 1) \\ (\frac{a_{0,0}}{a_{4,2}}\frac{C^F_{4,2}}{F_0} - 1) \\ (\frac{a_{0,0}}{a_{4,4}}\frac{C^F_{4,4}}{F_0} - 1) \end{bmatrix} = \begin{bmatrix} -\frac{1}{2} & -2 \\ -\frac{1}{2} & -2 \\ -\frac{5}{3} & -\frac{5}{6} \\ -\frac{5}{3} & -\frac{5}{6} \\ -\frac{5}{3} & -\frac{5}{6} \end{bmatrix} \begin{bmatrix} \chi_B \\ \\ \chi_C \end{bmatrix}. \tag{B.51}$$

Note that in the case of obliquity tides, $a_{4,4} = 0$. As the final row on the left hand side would then be undefined, we remove the final row of both 5x2 matrices in the case of obliquity tides.

For a matrix equation of the form $\underline{Y} = \mathbf{X}\underline{B}$, where underlined variables are vectors and bold variables are 2-dimensional matrices, we can estimate coefficients $\underline{B}$ (i.e. heating pattern weights χ_B and χ_C) with regressed coefficients $\underline{b} = (\mathbf{X}^T\mathbf{X})^{-1}(\mathbf{X}^T\underline{Y})$ where T signifies a transposed matrix. For this multi-linear function, we calculate a goodness-of-fit value known as the coefficient of determination R^2:

$$R^2 = \frac{\Sigma_{i=1}^n(\hat{y}_i - \bar{y})^2}{\Sigma_{i=1}^n(y_i - \bar{y})^2}, \tag{B.52}$$

where y_i are components of $\underline{Y}$, $\hat{y}_i$ are components of the matrix product $\mathbf{X}\underline{b}$, and $\bar{y}$ is the mean of the components of $\underline{Y}$.

B.7 Verification

B.7.1 Forward model

We also forward model the topography given our derived tidal heating pattern weights, moment of inertia, and average basal heat flux. Using the following equation from our paper, we find the basal heat flux distribution as a function of the tidal heating pattern weights.

$$\frac{F(\theta,\lambda)}{F_0} = \chi_D + \frac{\chi_T}{\psi_0}(\chi_A\psi_A + \chi_B\psi_B + \chi_C\psi_C). \tag{B.53}$$

For Pratt isostasy, we use Equation B.42 to find the change in average shell temperature for a given basal heat flux. Then, combining Equations B.39 and B.40 we find

$$\frac{-\delta\rho}{\rho_C + \delta\rho} = \alpha'(\bar{T}_0)\Delta\bar{T} \tag{B.54}$$

$$\Rightarrow \delta\rho = \frac{-\rho_C\alpha'(\bar{T}_0)\Delta\bar{T}}{1+\alpha'(\bar{T}_0)\Delta\bar{T}}. \tag{B.55}$$

Rearranging Equation B.37, we can then use the change in crustal density to solve for the topography due to tidal heating:

$$h = \frac{-\delta\rho}{\rho_C}\Big\{\frac{g_B}{g_S}(R_0 - d_0) - R_0 + \frac{2\pi G}{g_S}\big[R_0^2 - (R_0-d_0)^2\big]\Big\}. \tag{B.56}$$

We can then integrate to find the spherical harmonic weights of topography due to tidal heating, and add those due to tidal and rotational stretching for a total modeled topography spherical harmonic weights. This can then directly be compared with the observations and their uncertainties.

For Airy isostasy, we still use Equation B.53 to find the basal heat flux distribution as a function of tidal heating pattern weights. We then have to invert Equation B.38 to find d as a function of F. First, we rearrange equation B.13 to

$$R_0 - d = \sqrt{\frac{-k_{0,p}}{F} \frac{\ln(T_S/T_A)}{(\frac{1}{R_0-L} - \frac{1}{R_0})}}. \tag{B.57}$$

For ease of derivation, let κ_1 be a constant such that

$$\kappa_1 = \frac{-k_{0,p}}{F} \ln\Big(\frac{T_S}{T_A}\Big). \tag{B.58}$$

Then,

$$R_0 - d = \sqrt{\frac{\kappa_1}{(\frac{1}{R_0-L} - \frac{1}{R_0})}}. \tag{B.59}$$

We can then substitute $R_0 - d$ from equation B.59 into equation B.14, and solve for $R_0 - L$, which we can then substitute back into equation B.59 to solve for $R_0 - d$. This way we solve for both d and L.

First, equation B.59 into B.14:

$$F\frac{\kappa_1}{\frac{1}{R_0-L} - \frac{1}{R_0}} = \frac{-k_0 \ln(T_A/T_B)}{\sqrt{\frac{\frac{1}{R_0-L} - \frac{1}{R_0}}{\kappa_1}} - \frac{1}{R_0-L}} \tag{B.60}$$

$$\Rightarrow \sqrt{\frac{\frac{1}{R_0-L} - \frac{1}{R_0}}{\kappa_1}} - \frac{1}{R_0-L} = \frac{-k_0 \ln(T_A/T_B)}{F_0\kappa_1}\Big(\frac{1}{R_0-L} - \frac{1}{R_0}\Big). \tag{B.61}$$

Let there be another constant κ_2 defined

$$\kappa_2 = \frac{-k_0 \ln(T_A/T_B)}{F\kappa_1} = \frac{k_0 \ln(T_A/T_B)}{k_{0,p} \ln(T_S/T_A)}. \tag{B.62}$$

Then,

$$\sqrt{\frac{\frac{1}{R_0-L}-\frac{1}{R_0}}{\kappa_1}}-\frac{1}{R_0-L} = \kappa_2\Big(\frac{1}{R_0-L}-\frac{1}{R_0}\Big) \quad \text{(B.63)}$$

$$\Rightarrow \sqrt{\frac{\frac{1}{R_0-L}-\frac{1}{R_0}}{\kappa_1}}^2 = \Big(\frac{\kappa_2+1}{R_0-L}-\frac{\kappa_2}{R_0}\Big)^2. \quad \text{(B.64)}$$

After squaring both sides, we can follow some simple arithmetic to rearrange and collect like terms until we find a second-order polynomial expression of $R_0 - L$:

$$(R_0-L)^2\Big(\frac{\kappa_1\kappa_2^2}{R_0^2}+\frac{1}{R_0}\Big)+(R_0-L)\Big[\frac{-2\kappa_1\kappa_2}{R_0}(\kappa_2+1)-1\Big]+\kappa_1(\kappa_2+1)^2=0, \quad \text{(B.65)}$$

which can then be solved for with the quadratic equation. Let

$$a = \frac{\kappa_1\kappa_2^2}{R_0^2}+\frac{1}{R_0} \quad \text{(B.66)}$$

$$b = \frac{-2\kappa_1\kappa_2}{R_0}(\kappa_2+1)-1 \quad \text{(B.67)}$$

$$c = \kappa_1(\kappa_2+1)^2. \quad \text{(B.68)}$$

Then

$$R_0 - L = \frac{-b \pm \sqrt{b^2-4ac}}{2a}, \quad \text{(B.69)}$$

which yields L. Substituting equation B.69 into equation B.59 also yields d. The $\pm$ is $+$ when $d < 0.5R_0$, and $-$ when $d > 0.5R_0$. We know the average shell thickness d_0 *a priori* because this is a forward model where d_0 is an input, but we do not always know if d is less or greater than $0.5R_0$, and thus tend to avoid models where the shell is too close to half the radius.

The full expressions for L and d are

$$L = R_0 - \frac{1 - \frac{2k_0}{R_0 F}\ln\left(\frac{T_A}{T_B}\right)\left[\frac{k_0}{k_{0,p}}\frac{\ln(T_A/T_B)}{\ln(T_S/T_A)} + 1\right]}{\frac{2}{R_0}\left\{1 - \frac{[k_0 \ln(T_A/T_B)]^2}{F k_{0,p} \ln(T_S/T_A)}\right\}} \pm \frac{\sqrt{1 - \frac{4k_{0,p}}{R_0 F}\ln\left(\frac{T_S}{T_A}\right)\left\{2\left[\frac{k_0}{k_{0,p}}\frac{\ln(T_A/T_B)}{\ln(T_S/T_A)}\right]^2 + 3\frac{k_0}{k_{0,p}}\frac{\ln(T_A/T_B)}{\ln(T_S/T_A)} + 1\right\}}}{\frac{2}{R_0}\left\{1 - \frac{[k_0 \ln(T_A/T_B)]^2}{F k_{0,p} \ln(T_S/T_A)}\right\}} \quad \text{(B.70)}$$

$$d = R_0 - \sqrt{\frac{\frac{-k_{0,p}}{F}\ln(T_S/T_A)}{(\frac{1}{R_0 - L} - \frac{1}{R_0})}}. \quad \text{(B.71)}$$

Once we find the difference in shell thickness from average Δd, we use Equation 2.9 to solve for topography and find spherical harmonic coefficients as earlier.

B.7.2 Consistency Checks

One way to check that a model is physically consistent is to construct a density profile. For instance, it does not make sense if the solid ice layer needs to have a negative thickness to satisfy bulk density and moment of inertia constraints.

Let our spherical model of Tethys with radius R, mass M, and bulk density $\bar{\rho}$ have three concentric layers from surface to center: a porous ice shell of thickness L and uniform density $\rho_P = \rho_{ice}(1 - \phi)$, a solid ice shell of thickness $d - L$ and uniform density $\rho_S = \rho_{ice}$, and an interior "core" with density ρ_{core}.

If we know the bulk density of our planetary body $\bar{\rho} = \frac{3M}{4\pi R_0^2}$ and the density of ice ρ_{ice} then

$$\bar{\rho} R_0^3 = \rho_P[R^3 - (R - L)^3] + \rho_S[(R - L)^3 - (R - d)^3] + \rho_{\text{core}}(R - d)^3. \quad \text{(B.72)}$$

For a sphere of radial density profile $\rho(r)$, the normalized moment of inertia is found

$$\frac{C}{MR^2} = \frac{1}{MR^2}\frac{8\pi}{3}\int_0^R \rho(r) r^4 dr. \tag{B.73}$$

Assuming our piece-wise density profile

$$\rho(r) = \begin{cases} \rho_{\text{core}}, & \text{for } 0 \leq r \leq R-d, \\ \rho_S, & \text{for } R-d < r \leq R-L \\ \rho_P, & \text{for } R-L < r \leq R. \end{cases} \tag{B.74}$$

then equation B.73 becomes

$$\frac{15MR^2}{8\pi}\frac{C}{MR^2} = \rho_P[R^5-(R-L)^5] + \rho_P[(R-L)^5-(R-d)^5] + \rho_{\text{core}}(R-d)^5. \tag{B.75}$$

We rearrange both Equations B.72 and B.75 to isolate ρ_{core} and some factor of $R-d$:

$$\rho_{\text{core}}(R-d)^3 = \bar{\rho}R^3 - \rho_P[R^3-(R-L)^3] - \rho_S(R-L)^3 \tag{B.76}$$

$$\rho_{\text{core}}(R-d)^5 = \frac{15MR^2}{8\pi}\frac{C}{MR^2} - \rho_P[R^5-(R-L)^5] - \rho_S(R-L)^5. \tag{B.77}$$

We divide Equation B.77 by Equation B.76 to find $(R-d)^2$. Rearranging, we then find the total shell thickness d as a result of this three-layer model:

$$d_{3\text{ layer}} = R - \sqrt{\frac{\frac{15MR^2}{8\pi}\frac{C}{MR^2} - \rho_P[R^5-(R-L)^5] - \rho_S(R-L)^5}{\bar{\rho}R^3 - \rho_P[R^3-(R-L)^3] - \rho_S(R-L)^3}}. \tag{B.78}$$

Then to find the bulk density of the interior, we simply plug $d_{3\text{ layer}}$ from Equation B.78 into either Equation B.76 or B.77 and solve for ρ_{core}.

For this density profile to be physically feasible under the constraints of the

moment of inertia and bulk density, we want $d_{3\text{ layer}}$ to be the same as the d we input. There can be some leeway in the model, as it is unclear how hot ice must be to viscously flow, so we place some broad constraints. First, we expect $d_{3\text{ layer}} > L$, else we have a solid ice layer of negative thickness. Secondly, we want $d_{3\text{ layer}}$ to not be so deep that its basal temperature would exceed the melting point of water. We define a maximum ice shell thickness $d_{\max}$ such that the basal temperature is 270 K (if the originally specified basal temperature T_B was not already 270 K), that we constrain $d_{3\text{ layer}}$ not to exceed.

From the same process for which we formulated Fourier's law for an upper porous layer (Equation B.13) and a lower solid layer (Equation B.14) of the ice shell, we can define Fourier's law for a layer below that extending to a maximum basal temperature T_{max} at a total shell thickness d_{max}:

$$F(R-d)^2 = \frac{-k_0 \ln(T_B/T_{max})}{\frac{1}{R_0-d_{max}} - \frac{1}{R_0-d}}, \tag{B.79}$$

which we rearrange to solve for d_{max}:

$$d_{max} = R_0 - \Big[\frac{1}{R_0-d} - \frac{k_0 \ln(T_B/T_{max})}{F_0(R_0-d)^2}\Big]^{-1}. \tag{B.80}$$

If $T_B = T_{max}$, $d_{max} = d$.

B.7.3 Uncertainty

With any model, it is important to ascertain how accurate it may be given any uncertainty in input parameters. In many aspects, we seek to minimize the error of any given inversion by testing over a wide parameter space. i.e. by inferring the heat flux distribution for a many combinations of input shell thicknesses, moments of inertia,

and upper ice shell porosities; we ascertain how changing each of those may affect our results. This leaves one last uncertainty to worry about: uncertainty in the observed spherical harmonic weights of topography (from Nimmo et al., 2011).

If we propagate the error in topography to the inferred basal heat flux, the spherical harmonic weights of that heat flux will have a fractional uncertainty on the order of the fractional uncertainty in spherical harmonic weights of topography. However, our multilinear regression more-so asks "can this inferred heat distribution be represented by tidal heating?" That would be information given by the coefficient of determination R^2. High R^2 close to 1 informs us when the patterns of tidal heating fit well to our heat flux distribution—which we expect after already accounting for other major contributors to the degree 2 and 4 topography.

Another measure of the how well our inferred tidal heating pattern weights fit is the aforementioned forward model. We can directly compare the spherical harmonic weights of forward modeled topography to the spherical harmonic weights of the observed topography, and we do so in the paper. We also compute the root-mean-squared (RMS) misfit of the observed and forward-modeled topographies. To get a sense of how this compares to uncertainty in observed spherical harmonic coefficients, we composed 100 sets of randomly generated spherical harmonic coefficients of topography, where each coefficient was randomly generated using a normal distribution using the mean and uncertainties provided by Nimmo et al. (2011). We calculated the RMS misfit of each randomly-generated topography compared to the mean observed topography, and find an average RMS misfit of 78$\pm$36 m.

As uncertainty in tidal heating pattern weights does not necessarily correspond with how well the tidal heating pattern weights fit the inferred basal heat flux distribution, it is important to utilize these other methods of checking consistency between the topography and tidal heating. Then by isolating for the best R^2, RMS, and only those that fulfill other constraints, we settle upon the range of models that best seem to explain Tethys.

B.8 Enceladus

Before inferring Tethys' interior, we tested our methodology on a world for which we already knew the moment of inertia and interior structure: Enceladus. As with Tethys, we use long-wavelength topography from Nimmo et al. (2011). As initial conditions, we varied the shell thickness from 2–76 km in 2 km increments, and the normalized MoI in increments of 0.005 MR^2. We tested both Airy and Pratt isostasy, as well as both eccentricity and obliquity tides. We varied the porosity of the upper ice shell ($\leq$ 140 K) from 0 to 0.3 in increments of 0.1. We assume Enceladus' mean radius of 252.1 km and bulk density of 1609 kg m^{-3} (Roatsch et al., 2009), and follow Chen et al. (2014) in assuming an angular rotation rate of 5.31×10^{-5} rad s^{-1}. As in our main manuscript, we assume solid water ice has a density of 940 kg m^{-3}. We found there were no good fits for tidal heating patterns if we assumed Pratt isostasy or obliquity tides, while Airy isostasy and eccentricity tides had high R^2 and low RMS values, with high heating pattern C weights (Figure B.1). This is consistent with observations of

Enceladus' eccentric orbit and subsurface ocean. Our goodness of fit measurements, the multilinear regression's coefficient of determination R^2 and the forward model's RMS misfit from the observed topography improved when we assumed higher porosities (up to 0.3) in the upper ice shell, which is consistent with other models such as that of Besserer et al. (2013). Further, the best fits for tidal heating patterns occurred for moments of inertia and ice-shell thicknesses that are roughly consistent with those inferred gravitationally (Iess et al., 2014; Beuthe et al., 2016). That is, our models with the highest R^2 and lowest RMS assumed have a moment of inertia 0.30-0.32, an ice shell thickness of 30-40 km, an ocean thickness of 25-50 km, and a core density of 1700-2300 kg m^{-3}.

In these best fit models, we find heating pattern weights $\chi_A \sim 0.16$, $\chi_B \sim 0.31$, $\chi_C \sim 0.53$ with deviations up to 0.03. Beyond the C weight being highest, these do not necessarily align with what we expect for a thin ice-shell overlaying an ocean (Figure 4 from the main text). The expected fraction of Enceladus' heating to be radiogenic is less than 1%, so we do not expect a large uniform heat flux component from radioactivity. These weights also closely resemble but do not quite match heating in a homogenous core (χ_A=0.13, χ_B=0.31, χ_C=0.56). Linear mixtures of the interior heating weights and heating weights for an ice shell 15% of Enceladus' radius cannot reproduce our inferred heating pattern weights for Enceladus. However, mixtures of a uniform heat flux pattern (χ_A=0.2, χ_B=0.4, χ_C=0.4) with the heating pattern weights of an ice shell 15% of Enceladus' radius can get quite close when 30% of the heating pattern is due to shell heating, and 70% of the heating pattern is uniform. There is no exact

match, but because the R^2 is not a perfect 1.0, the inferred heating pattern weights are likely muddled by other factors, such as the south polar terrain. While Enceladus is low in radionuclides, a large proportion of the inferred heating pattern being uniform can be due to heating in Enceladus' core, the heating pattern of which is then well-mixed into a uniform background flux by Enceladus' ocean. Given that Enceladus' large heat production is hard to produce tidally in its ice shell, core heating is a very likely explanation (Roberts, 2015; Choblet et al., 2017; Hemingway and Mittal, 2019)

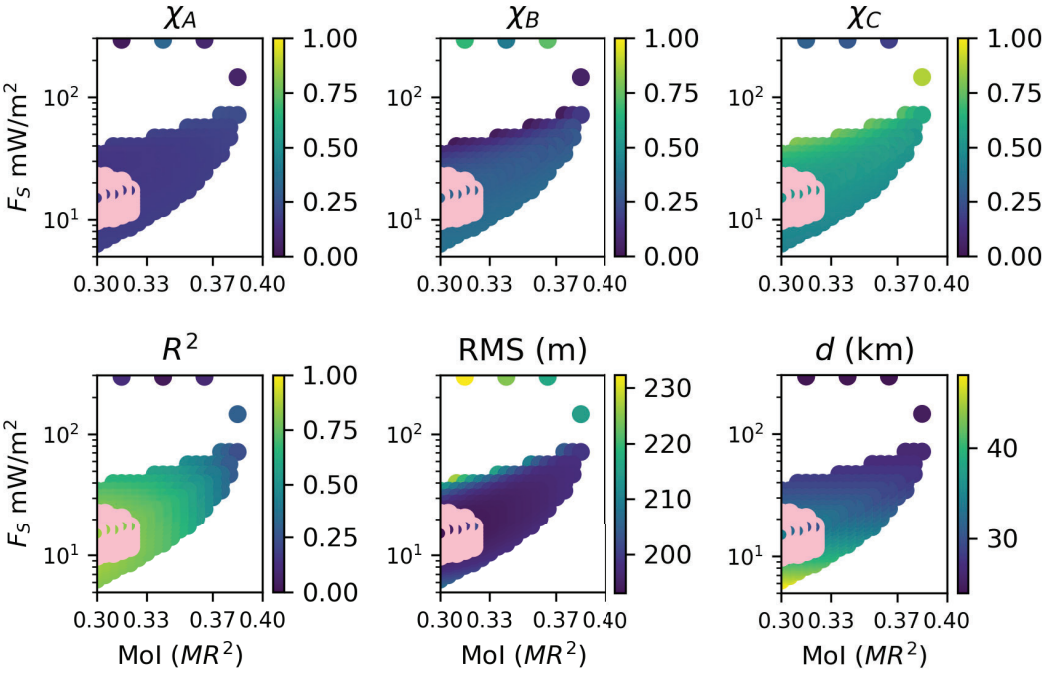

Figure B.1: Assuming an isothermal basal ice shell temperature of 270K, for an ice shell with 30% porosity at ≤140 K, under Airy isostasy and eccentricity tides assuming equal-pressure isostasy, we varied the ice shell thickness and moment of inertia parameters before inferring the heat flux distribution at the base of the ice shell. We then fit for the spatial patterns of tidal heating weights (χ_{A-C}) from Beuthe (2013). We plot only models where the ocean thickness from the moment of inertia is neither negative nor larger than possible. Of particular interest is the region with moment of inertia <0.34 MR^2 for a basal heat flux between 10 and 30 mW m^{-2}, where the coefficient of determination R^2 is high and the RMS misfit is low. Specifically, the pink circles mark where R^2 is >90th percentile and RMS is <10th percentile. These two indications of goodness of fit narrow down this region as when parameters best find tidal heating patterns from topography. d is the ice shell thickness assumed, from which the average surface heat flux F_S is calculated.

Appendix C

Appendix for Chapter 3

In Section 3.4.2, we state that the semi-major axis a of a satellite is embedded within many of the parameters of Equation 3.16. First, a synchronous satellite in a Keplerian orbit will have an orbital frequency $\omega = \sqrt{GM_{Sat}/a^3}$, where M_{Sat} is Saturn's mass. A decrease in a and thus increase in ω alone will reduce the inclination i necessary for a given obliquity θ. The gravity coefficients J_2 and $C_{2,2}$ also increase with ω^2 (via q in Equations 3.12 and 3.13) and compound this reduction. Mimas' $\dot{\Omega}$ is also dominated by a term that depends on Saturn's oblateness (Equation 3.14). This precession rate increases with lower a, but its contribution to $\sin\theta/\sin i$ is outweighed by those from ω and the gravity coefficients. Propagating these dependencies, the obliquity θ one expects from a satellite in a Cassini state orbiting at semi-major axis a with a given inclination i is

$$\sin\theta = \frac{\sin i}{\cos i - \frac{1}{J_{2,Sat}R_{Sat}^2} k_2^F \frac{M_{Sat}}{3\bar{\rho}a}\left(4 + \frac{136}{21} h_2^F \frac{M_{Sat}}{\bar{\rho}a^3}\right)}, \tag{C.1}$$

where we assumed the entirety of nodal precession rate is dominated by Saturn's oblateness using Equation 3.14. Finally, through Equation 2.30, the obliquity needed for our inferred dissipated power $\dot{E}$ of 10 GW decreases the smaller a (and thus larger ω) is. Inverting Equation 2.30, we find that the exact dependence of the obliquity θ required for a body of a given k_2/Q to dissipate $\dot{E}$ at a semi-major axis a is

$$\sin\theta = \left(\frac{2}{3}\frac{\dot{E}}{k_2/Q}\right)^{1/2}\left(\frac{1}{G^3 M_{Sat}}\right)^{1/4}\frac{a^{15/4}}{R_0^{5/2}}. \tag{C.2}$$

By requiring a lower obliquity for our inferred tidal heating state, inclination need not be as high. However, this would still require Mimas to be quite close to Saturn. This would indicate that the impact necessary to temporarily increase Mimas' inclination would be quite ancient. However, the required semi-major axis at the time of this impact or inclination-type resonance would require Mimas to be well within Saturn's Roche limit and at risk of tidal disruption: taking the extent of Saturn's A rings ($\sim$2.35 Saturn radii) as a proxy for Saturn's Roche limit, the required obliquity to generate 10 GW of tidal heating is -0.54° (Equation C.2), but the inclination to reach that obliquity at that semi-major axis is 51° (Equation C.1). Such a high inclination is unlikely to be the result of an impact or past inclination-type resonance.

Bibliography

K. Baillié, B. Noyelles, V. Lainey, S. Charnoz, and G. Tobie. Formation of the Cassini Division, - I. shaping the rings by Mimas inward migration. *Monthly Notices of the Royal Astronomical Society*, 486(2):2933–2946, 2019. doi: 10.1093/mnras/stz548.

O. S. Barnouin-Jha, S. Yamamoto, T. Toriumi, S. Sugita, and T. Matsui. Non-intrusive measurements of crater growth. *Icarus*, 188(2):506–521, 2007. doi: 10.1016/j.icarus.2007.01.009.

J. Besserer, F. Nimmo, J. H. Roberts, and R. T. Pappalardo. Convection-driven compaction as a possible origin of Enceladus's long wavelength topography. *Journal of Geophysical Research: Planets*, 118(5):908–915, 2013. doi: 10.1002/jgre.20079.

J. Besserer, F. Nimmo, M. Wieczorek, R. Weber, W. Kiefer, P. McGovern, J. Andrews-Hanna, D. Smith, and M. Zuber. GRAIL gravity constraints on the vertical and lateral density structure of the lunar crust. *Geophysical Research Letters*, 41(16): 5771–5777, 2014. doi: 10.1002/2014GL060240.

M. Beuthe. Spatial patterns of tidal heating. *Icarus*, 223(1):308–329, 2013. doi: 10.1016/j.icarus.2012.11.020.

M. Beuthe. Isostasy with Love – i: elastic equilibrium. *Geophysical Journal International*, 225(3):2157–2193, 2021. doi: 10.1093/gji/ggab073.

M. Beuthe, A. Rivoldini, and A. Trinh. Enceladus's and dione's flating ice shells supported by minimum stress isostasy. *Geophysical Research Letters*, 43(19):10088–10096, 2016. doi: 10.1002/2016GL070650.

B. G. Bills and F. Nimmo. Forced obliquities and moments of inertia of Ceres and Vesta. *Icarus*, 213(2):496–509, 2011. doi: 10.1016/j.icarus.2010.09.002.

R. J. Blakely. *Potential Theory in Gravity and Magnetic Applications*. Cambridge University Press, Cambridge (UK), 1995.

W. Bottke and J. Andrews-Hanna. A post-accretionary lull in large impacts on early Mars. *Nature Geoscience*, 10:344–348, 2017. doi: 10.1038/ngeo2937.

A. Broquet and M. Wieczorek. The gravitational signature of Martian volcanoes. *Journal of Geophysical Research: Planets*, 124(8):2054–2086, 2019. doi: 10.1029/2019JE005959.

R. M. Canup. Dynamics of lunar formation. *Annual Review of Astronomy and Astrophysics*, 42:441–475, 2004. doi: 10.1146/annurev.astro.41.082201.113457.

Y. Caristan. *High temperature mechanical behavior of Maryland diabase*. PhD thesis, Massachusetts Institute of Technology, 1980.

S. Champenois and A. Vienne. The role of secondary resonances in the evolution of the Mimas-Tethys system. *Icarus*, 140(1):106–121, 1999. doi: 10.1006/icar.1999.6115.

E. M. A. Chen and F. Nimmo. Implications from Ithaca Chasma for the thermal and orbital history of Tethys. *Geophysical Research Letters*, 35(19), 2008. doi: 10.1029/2008GL035402.

E. M. A. Chen and F. Nimmo. Obliquity tides do not significantly heat Enceladus. *Icarus*, 214(2):779–781, 2011. doi: 10.1016/j.icarus.2011.06.007.

E. M. A. Chen, F. Nimmo, and G. A. Glatzmaier. Tidal heating in icy satellite oceans. *Icarus*, 229:11–30, 2014. doi: 10.1016/j.icarus.2013.10.024.

G. Choblet, G. Tobie, C. Sotin, M. Běhounková, O. Čadek, F. Postberg, and O. Souček. Powering prolonged hydrothermal activity inside Enceladus. *Nature Astronomy*, 1: 841–847, 2017. doi: 10.1038/s41550-017-0289-8.

C. Clauser and E. Huenges. *Rock Physics and Phase Relations: A Handbook of Physical Constants*, volume 3, page 105. 1995.

S. Clifford. A model for the hydrologic and climatic behavior of water on Mars. *Journal of Geophysical Research: Planets*, 98(E6):10973, 1993. doi: 10.1029/93JE00225.

S. Clifford and T. Parker. The evolution of the Martian hydrosphere: Implications for the fate of a primordial ocean and the current state of the northern plains. *Icarus*, 154(1):40 – 79, 2001. doi: 10.1006/icar.2001.6671.

M. Ćuk, L. Dones, and D. Nesvorný. Dynamical evidence for a late formation of Saturn's moons. *The Astrophysical Journal*, 820(2):97, 2016. doi: 10.3847/0004-637X/820/2/97/.

D. Demming. *Introduction to Hydrology*. McGraw-Hill, 2002.

C. A. Denton and A. R. Rhoden. Tracking the evolution of an ocean within Mimas using the Herschel impact basin. *Geophysical Research Letters*, 49(24), 2022. doi: 10.1029/2022GL100516.

L. Dones. a recent cometary origin for Saturn's rings? *Icarus*, 92(2):194–203, 1991. doi: 10.1016/0019-1035(91)90045-U.

L. Dones, C. R. Chapman, W. B. McKinnon, H. J. Melosh, M. R. Kirchoff, G. Neukum, and K. J. Zahnle. *Saturn from Cassini-Huygens*, chapter Icy Satellites of Saturn: Impact Cratering and Age Determination, pages 613–635. Springer, Dordrecht, 2009. doi: 10.1007/978-1-4020-9217-6_19.

W. B. Durham, W. B. McKinnon, and L. A. Stern. Cold compaction of water ice. *Geophysical Research Letters*, 32:L18202, 2005. doi: 10.1029/2005GL023484.

J. Eluszkiewicz. Compaction and internal structure of mimas. *Icarus*, 84(1):215, 2004. doi: 10.1016/0019-1035(90)90167-8.

S. N. Ferguson, A. R. Rhoden, M. R. Kirchoff, and J. J. Salmon. A unique Saturnian impactor population from elliptical craters. *Earth and Planetary Science Letters*, 593: 117652, 2022. doi: 10.1016/j.epsl.2022.117652.

A. Fowler. A mathematical model of magma transport in the asthenosphere. *Geophysical & Astrophysical Fluid Dynamics*, 33(1–4):63, 1985. doi: 10.1080/03091928508245423.

H.-P. Gail, S. Henke, and M. Trieloff. Thermal evolution and sintering of chondritic planetesimals ii. improved treatment of the compaction process. *Astronomy & Astrophysics*, 576(A60), 2015. doi: 10.1051/0004-6361/201424278.

B. Giese, R. Wagner, G. Neukum, P. Helfenstein, and P. C. Thomas. Tethys: lithospheric thickness and heat flux from flexurally supported topography at Ithaca Chasma. *Geophysical Research Letters*, 34(21):L21203, 2007. doi: 10.1029/2007GL031467.

K. Gillet, M. Calvet, and M. Monnereau. Scattering attenuation profile of the moon: Implications for shallow moonquakes and the structure of the megaregolith. *Physics of the Earth and Planetary Interiors*, 262:28, 2017. doi: 10.1016/j.pepi.2016.11.001.

B. Gladman, D. D. Quinn, P. Nicholson, and R. Rand. Synchronus locking of tidally evolving satellites. *Icarus*, 122(1):166–192, 1996. doi: 10.1006/icar.1996.0117.

P. Goldreich and S. Tremaine. The dynamics of planetary rings. *Annual Review of Astronomy and Astrophysics*, 20:249–283, 1982. doi: 10.1146/annurev.aa.20.090182.001341.

M. Golombek, N. Warner, J. Grant, E. Hauber, V. Ansan, C. Weitz, N. Williams, C. Charalambous, S. Wilson, A. DeMott, M. Kopp, H. Lethcoe-Wilson, L. Berger, R. Hausmann, E. Marteau, C. Vrettos, A. Trussell, W. Folkner, S. Le Maistre, N. Mueller, M. Grott, T. Spohn, S. Piquex, E. Millour, F. Forge, I. Daubar, N. Murdoch, P. Lognonné, C. Perrin, S. Rodriguez, W. Pike, T. Parker, J. Maki,

H. Abarca, R. Deen, J. Hall, P. Andres, N. Ruoff, F. Calef, S. Smrekar, M. Baker, M. Banks, A. Spiga, D. Banfield, J. Garvin, C. Newman, and W. Banerdt. Geology of the insight landing site on Mars. *Nature Communications*, 11:1014, 2020. doi: 10.1038/s41467-020-14679-1.

S. Gyalay and F. Nimmo. Estimates for Tethys' moment of inertia, heat flux distribution, and interior structure from its long-wavelength topography. *Journal of Geophsyical Research: Planets*, 128(2), 2023. doi: 10.1029/2022JE007550.

S. Gyalay, F. Nimmo, A.-C. Plesa, and M. Wieczorek. Constraints on thermal history of Mars from depth of pore closure below InSight. *Geophysical Research Letters*, 47 (16):e2020GL088653, 2020. doi: 10.1029/2020GL088653.

S. Gyalay, F. Nimmo, A.-C. Plesa, and M. Wieczorek. Heat flux and temperature at depth beneath InSight landing site through time. Dataset, 2020b.

S. Gyalay, F. Nimmo, and B. Downey. Inferring Mimas' spatial distribution of tidal heating from its long-wavelength topography. Dataset, 2023. URL `https://datadryad.org/stash/share/Bsf-w1PcaepcFiIv9x3KJR4Q9eijXjioh1swG-NXShs`. This is a private URL for peer review. The repository will be made public with a doi for the final draft.

B. Hahn, S. McLennan, and E. Klein. Martian surface heat production and crustal heat flow from Mars Odyssey gamma-ray spectrometry. *Geophysical Research Letters*, 38 (14), 2011. doi: 10.1029/2011GL047435.

J. Hanna and R. Phillips. Hydrological modeling of the martian crust with application to the pressurization of aquifers. *Journal of Geophysical Research: Planets*, 110(E1), 2005. doi: 10.1029/2004JE002330.

S. Hauck and R. Phillips. Thermal and crustal evolution of Mars. *Journal of Geophysical Research: Planets*, 107(E7):6–1 – 6–19, 2002. doi: 10.1029/2001JE001801.

D. Hemingway and I. Masuyama. Isostatic equilibrium in spherical coordinates and implications for crustal thickness on the Moon, Mars, Enceladus, and elsewhere. *Geophysical Research Letters*, 44(15):7695–7705, 2017. doi: 10.1002/2017GL073334.

D. Hemingway and T. Mittal. Enceladus's ice shell structure as a window on internal heat production. *Icarus*, 332:111–131, 2019. doi: 10.1016/j.icarus.2019.03.011.

D. Hewitt, J. Neufeld, and J. Lister. High rayleigh number convection in a three-dimensional porous medium. *Journal of Fluid Mechanics*, 748:879, 2014. doi: 10.1017/jfm.2014.216.

C. J. A. Howett, J. R. Spencer, J. Pearl, and M. Segura. Thermal inertia and bolometric Bond albedo values for Mimas, Enceladus, Tethys, Dione, Rhea and Iapetus as derived from Cassini/CIRS measurements. *Icaurs*, 206(2):573–593, 2010. doi: 10.1016/j.icarus.2009.07.016.

C. J. A. Howett, J. R. Spencer, P. Schenk, R. E. Johnson, C. Paranicas, T. A. Hurford, A. Verbiscer, and M. Segura. A high-amplitude thermal inertia anomaly of probable

magnetospheric origin on saturn's moon mimas. *Icarus*, 216(1), 2011. doi: 10.1016/j.icarus.2011.09.007.

H. Hussmann, A. Rodríguez, N. Callegari Jr., and D. Shoji. Early resonances of Tethys and Dione: Implications for Ithaca Chasma. *Icarus*, 319:407–416, 2019. doi: 10.1016/j.icarus.2018.09.025.

R. Hyodo and S. Charnoz. Dynamical evolution of the debris disk after a satellite catastrophic disruption around Saturn. *Astronomical Journal*, 154(34), 2017. doi: 10.3847/1538-3881/aa74c9.

R. Hyodo, S. Charnoz, K. Ohtuski, and H. Genda. Ring formation around giant planets by tidal disruption of a single passing large kuiper belt object. *Icarus*, 282:195–213, 2017a. doi: 10.1016/j.icarus.2016.09.012.

L. Iess, D. J. Stevenson, M. Parisi, D. Hemingway, R. A. Jacobson, J. Lunine, F. Nimmo, J. W. Armstrong, S. W. Asmar, M. Ducci, and P. Tortora. The gravity field and interior structure of Enceladus. *Science*, 344(6179):78–80, 2014. doi: 10.1126/science.1250551.

L. Iess, B. Militzer, Y. Kaspi, P. Nicholson, D. Durante, P. Racioppa, A. Anabtawi, E. Galanti, W. Hubbard, M. J. Mariani, P. Tortora, S. Wahl, and M. Zannoni. Measurement and implications of Saturn's gravity field and ring mass. *Science*, 364(6445), 2019. doi: 10.1126/science.aat2965.

S. Karimi, A. Dombard, D. Buczkowski, S. Robbins, and R. Williams. Using the vis-

coelastic relaxation of large impact craters to study the thermal history of Mars. *Icarus*, 272:102 – 113, 2016. doi: 10.1016/j.icarus.2016.02.037.

J. Kegerreis, L. Teodoro, M. Ćuk, J. Cuzzi, V. Eke, P. Estrada, R. Massey, and T. Sandnes. A recent impact origin of Saturn's rings and mid-sized moons. In *54th Lunar and Planetary Science Conference*, number 2658, 2023.

H. Kieffer. Thermal model for analysis of Mars infrared mapping. *Journal of Geophysical Research: Planets*, 118(3):451 – 470, 2013. doi: 10.1029/2012JE004164.

M. R. Kirchoff and P. Schenk. Impact cratering records of the mid-sized, icy saturnian satellites. *Icarus*, 206(2):485–497, 2010. doi: 10.1016/j.icarus.2009.12.007.

M. R. Kirchoff, E. B. Bierhause, L. Dones, S. J. Robbins, K. N. Singer, R. J. Wagner, and K. J. Zahnle. *Enceladus and the Icy Moons of Saturn*, chapter Cratering Histories in the Saturnian system, pages 267–284. University of Arizona, Tuscon, 2018. doi: 10.2458/azu_uapress_9780816537075-ch013.

J. Klinger. Influence of a phase transition of ice on the heat and mass balance of comets. *Science*, 209(4453):271–272, 1980. doi: 10.1126/science.209.4453.271.

K. Kossacki and R. Lorenz. Hiding titan's ocean: Densification and hydrocarbon storage in an icy regolith. *Planetary and Space Science*, 44(9):1029, 1996.

V. Lainey, J. Arlot, O. Karatekin, and T. Van Hoolst. Strong tidal dissipation in Io and Jupiter from astrometric observations. *Nature*, 459:957–959, 2009. doi: 10.1038/nature08108.

V. Lainey, L. Gomez Casajus, J. Fuller, M. Zannoni, P. Tortora, N. Cooper, D. Murray, C andModenini, R. S. Park, V. Robert, and Q. Zhang. Resonance locking in giant planets indicated by the rapid orbital expansion of Titan. *Nature Astronomy*, 4: 1053–1058, 2020. doi: 10.1038/s41550-020-1120-5.

K. Lewis, S. Peters, K. Gonter, S. Morrison, N. Schmerr, A. Vasavada, and T. Gabriel. A surface gravity traverse on mars indicates low bedrock density at gale crater. *Science*, 363(6426):535–537, 2019. doi: 10.1126/science.aat0738.

P. Lognonné, W. Banerdt, W. Pike, D. Giardini, U. Christensen, R. Garcia, T. Kawamura, S. Kedar, B. Knapmeyer-Endrun, L. Margerin, F. Nimmo, M. Panning, B. Tauzin, J.-R. Scholz, D. Antonangeli, S. Barkaoui, E. Beucler, F. Bissing, N. Brinkman, M. Calvet, S. Ceylan, C. Charalambous, P. Davis, M. van Driel, M. Drilleau, L. Fayon, R. Joshi, B. Kenda, A. Khan, M. Knapmeyer, V. Lekaic, J. McClean, D. Mimoun, N. Murdoch, L. Pan, C. Perrin, B. Pinot, L. Pou, S. Menina, S. Rodriguez, C. Schmelzbach, N. Schmerr, D. Sollberger, A. Spiga, S. Stähler, A. Stott, E. Stutzmann, S. Tharimena, R. Widmer-Schnidrig, F. Andersson, V. Ansan, C. Beghein, M. Böse, E. Bozdag, J. Clinton, I. Daubar, P. Delage, N. Fuji, M. Golombek, M. Grott, A. Horleston, K. Hurst, J. Irving, A. Jacob, J. Knollenberg, S. Krasner, C. Krause, R. Lorenz, C. Michaut, R. Myhill, T. Nissen-Meyer, J. ten Pierick, A.-C. Plesa, C. Quantin-Nataf, J. Robertsson, L. Rochas, M. Schimmel, S. Smrekar, T. Spohn, N. Teanby, J. Tromp, J. Vallade, N. Verdier, C. Vrettos, D. Weber, R adn Banfield, E. Barrett, M. Bierwirth, S. Calcutt, N. Compaire, C. Johnson,

D. Mance, F. Euchner, L. Kerjean, G. Mainsant, A. Mocquet, J. Rodriguez Manfredi, G. Pont, P. Laudet, T. Nebut, S. de Raucourt, O. Robert, C. Russell, A. Sylvestre-Baron, S. Tillier, T. Warren, M. Wieczorek, C. Yana, and P. Zweifel. Constraints on the shallow elastic and anelastic structure of mars from insight seismic data. *Nature Geoscience*, 13:213, 2020. doi: 10.1038/s41561-020-0536-y.

S. Mackwell, M. Zimmerman, and D. Kohlstedt. High-temperature deformation of dry diabase with application to tectonics on venus. *Journal of Geophysical Research: Solid Earth*, 103(B1):975–984, 1998. doi: 10.1029/97JB0267.

C. Manning and S. Ingebritsen. Permeability of the continental crust: Implications of geothermal data and metamorphic systems. *Reviews of Geophysics*, 37(1):127 – 150, 1999. doi: 10.1029/1998RG900002.

P. McGovern, S. Solomon, D. Smith, M. Zuber, M. Simons, M. Wieczorek, R. Phillips, G. Neumann, O. Aharonson, and J. Head. Correction to "localized gravity/topography admittance and correlation spectra on Mars: Implications for regional and global evolution". *Journal of Geophysical Research: Planets*, 109(E7), 2004. doi: 10.1029/2004JE002286.

D. McKenzie, F. Nimmo, J. A. Jackson, P. B. Gans, and E. L. Miller. Characteristics and consequences of flow in the lower crust. *Journal of Geophysical Research: Solid Earth*, 105:11029–11046, 2000. doi: 10.1029/1999JB900446.

H. J. Melosh. *Impact cratering : a geologic process*. 1989.

J. Meyer and J. Wisdom. Tidal evolution of Mimas, Enceladus, and Dione. *Icarus*, 193 (1):213–223, 2008. doi: 10.1016/j.icarus.2007.09.008.

J. M. Moore, P. M. Schenk, L. S. Bruesch, E. Asphaug, and W. B. McKinnon. Large impact features on middle-sized icy satellites. *Icarus*, 171(2):421–443, 2004. doi: 10.1016/j.icarus.2004.05.009.

W. H. Munk and G. J. F. MacDonald. *The Rotation of the Earth: a Geophysical Discussion*. Cambridge University Press, Cambridge (UK), 1960.

C. D. Murray and S. F. Dermott. *Solar System Dynamics*. Cambridge University Press, Cambridge (UK), 1999.

A. Nadeau and R. McGehee. A simple formula for a planet's mean annual insolation by latitude. *Icarus*, 291:46–50, 2017. doi: 10.1016/j.icarus.2017.01.040.

I. E. Nadezhdina, A. E. Zubarev, E. S. Brusnikin, and J. Oberst. A libration model for Enceladus based on geodetic control point network analysis. *International Archives of the Photogrammetry, Remote Sensing and Spatial Information Sciences*, XLI-B4, 2016. doi: 10.5194/isprsarchives-XLI-B4-459-2016.

K. Nagel, D. Breuer, and T. Spohn. A model for the interior structure, evolution, and differentiation of callisto. *Icarus*, 169(2):402–412, 2004. doi: 10.1016/j.icarus.2003.12.019.

W. Neumann, D. Breuer, and T. Spohn. Modelling the internal structure of Ceres: Coupling of accretion with compaction by creep and implications for the water-rock

differentiation. *Astronomy & Astrophysics*, 584(A117), 2015. doi: 10.1051/0004-6361/201527083.

F. Nimmo. Non-Newtonian topographic relaxation on Europa. *Icarus*, 168(1):205–208, 2004. doi: 10.1016/j.icarus.2003.11.022.

F. Nimmo and R. T. Pappalardo. Ocean worlds in the outer solar system. *Journal of Geophsyical Research: Planets*, 121(8):1378–1399, 2016. doi: 10.1002/2016JE005081.

F. Nimmo, R. Pappalardo, and B. Giese. On the origins of band topography, Europa. *Icarus*, 166(1):21, 2003. doi: 10.1016/j.icarus.2003.08.002.

F. Nimmo, P. C. Thomas, R. T. Pappalardo, and W. B. Moore. The global shape of Europa: Constraints on lateral shell thickness variations. *Icarus*, 191:183–192, 2007. doi: 10.1016/j.icarus.2007.04.021.

F. Nimmo, B. G. Bills, and B. C. Thomas. Geophysical implications of the long-wavelength topography of the Saturnian satellites. *Journal of Geophysical Research*, 116:E11001, 2011. doi: 10.1029/2011JE003835.

F. Nimmo, A. C. Barr, M. Běhounková, and W. B. McKinnon. *Enceladus and the Icy Moons of Saturn*, chapter The thermal and orbital evolution of Enceladus: observational constraints and models, pages 79–94. University of Arizona, Tuscon, 2018. doi: 10.2458/azu_uapress_9780816537075-ch005.

B. Noyelles, K. Baillié, S. Charnoz, V. Lainey, and G. Tobie. Formation of the Cassini

Division - II. possible histories of Mimas and Enceladus. *Monthly Notices of the Royal Astronomical Society*, 486(2):2947–2963, 2019. doi: doi.org/10.1093/mnras/stz445.

G. Ohring and J. Mariano. Seasonal and latitudinal variations of the average surface temperature and vertical temperature profile on Mars. *Journal of the Atmospheric Sciences*, 25(5):673–681, 1968. doi: 10.1175/1520-0469(1968)025⟨0673:SALVOT⟩2.0.CO;2.

L. Pan, C. Quantin-Nataf, B. Tauzin, C. Michaut, M. Golombek, P. Lognonné, P. Grindrod, B. Langlais, T. Gudkova, I. Stepanova, S. Rodriguez, and A. Lucas. Crust stratigraphy and heterogeneities of the first kilometers at the dichotomy boundary in western Elysium Planitia and implications for InSight lander. *Icarus*, 338: 113511, 2020. doi: 10.1016/j.icarus.2019.113511.

E. Parmentier and M. Zuber. Early evolution of Mars with mantle compositional stratification or hydrothermal crustal cooling. *Journal of Geophysical Research: Planets*, 112(E2), 2007. doi: 10.1029/2005JE002626.

S. J. Peale. Generalized Cassini's laws. *Astronomical Journal*, 74(3):483–489, 1969.

S. J. Peale and P. Cassen. Contribution of tidal dissipation to lunar thermal history. 36:245–269, 1978. doi: 10.1016/0019-1035(78)90109-4.

A.-C. Plesa, S. Padovan, N. Tosi, D. Breuer, M. Grott, M. Wieczorek, T. Spohn, S. Smrekar, and W. Banerdt. The thermal state and interior structure of Mars. *Geophysical Research Letters*, 45(22):12198, 2018. doi: 10.1029/2018GL080728.

A. R. Rhoden and M. E. Walker. The case for an ocean-bearing Mimas from tidal heating analysis. *Icarus*, 376, 2022. doi: 10.1016/j.icarus.2021.114872.

I. Ribas. The sun and stars as the primary energy input in planetary atmospheres. *Proceedings of the International Astronomical Union*, 5(S264):3 – 18, 2010. doi: 10.1017/S1743921309992298.

T. Roatsch, R. Jaumann, K. Stephan, and P. C. Thomas. *Saturn from Cassini-Huygens*, chapter Cartographic mapping of the icy satellites using ISS and VIMS Data, pages 763–781. Springer, 2009. doi: 10.1007/978-1-4020-9217-6_24.

J. H. Roberts. The fluffy core of Enceladus. *Icarus*, 258:58–68, 2015. doi: 10.1016/j.icarus.2015.05.033.

J. H. Roberts and F. Nimmo. Tidal heating and long-term stability of a subsurface ocean on Enceladus. *Icarus*, 194(2):675–689, 2008. doi: 10.1016/j.icarus.2007.11.010.

K. Röttger, A. Endris, J. Ihringer, S. Doyle, and W. F. Kuhs. Lattice constants and thermal expansion of H_2O and D_2O ice i*h* between 10 and 265 k. *Acta Crystallographica*, 850:644–648, 1994.

A. Rust, J. Russel, and R. Knight. Dielectric constant as a predictor of porosity in dry volcanic rocks. *Journal of Volcanology and Geothermal Research*, 99(1):79–96, 1999. doi: 10.1016/S0377-0273(99)00055-4.

J. Schmoker and D. Gautier. Sandstone porosity as a function of thermal maturity.

Geology, 16(11):1007 – 1010, 1988. doi: 10.1130/0091-7613(1988)016⟨1007:SPAAFO⟩2.3.CO;2.

M. Segatz, T. Spohn, M. N. Ross, and G. Schubert. Tidal dissipation, surface heat flow, and figure of viscoelastic models of io. *Icarus*, 75(2):187–206, 1988. doi: 10.1016/0019-1035(88)90001-2.

U. Seipold. Temperature dependence of thermal transport properties of crystalline rocks: A general law. *Tectonophysics*, 291:161, 1998. doi: 10.1016/S0040-1951(98)00037-7.

Y. Shoshany, D. Prialnik, and M. Podolak. Monte Carlo modeling of the thermal conductivity of porous cometary ice. *Icarus*, 157(1):219–227, 2002. doi: 10.1006/icar.2002.6815.

A. T. Sinclair. A re-consideration of the evolution hypothesis of the origin of the resonances among Saturn's satellites. *International Astronomical Union Colloquium*, 74: 19–25, 1983. doi: 10.1017/S0252921100096871.

B. A. Smith, L. Soderblom, R. Beebe, J. Boyce, G. Briggs, A. Bunker, S. A. Collins, C. J. Hansen, T. V. Johnson, J. L. Mitchel, R. J. Terrile, M. Carr, A. F. Cook, J. Cuzzi, J. B. Pollack, G. E. Danielson, A. Ingersol, M. E. Davies, G. E. Hunt, H. Masursky, E. Shoemaker, D. Morrison, T. Owen, C. Sagan, J. Veverka, and V. E. Strom, R Suomi. Encounter with Saturn: Voyager 1 imaging science results. *Science*, 212(4491):163–191, 1981. doi: 10.1126/science.212.4491.163.

E. Smrekar, P. Lognonné, T. Spohn, W. Banerdt, D. Breuer, U. Christensen, V. Dehant,

M. Drilleau, W. Folkner, N. Fuji, R. Garcia, D. Giardini, M. Golombek, M. Grott, T. Gudkova, C. Johnson, A. Khan, B. Langlais, A. Mittelholz, A. Mocquet, R. Myhill, M. Panning, C. Perrin, T. Pike, A.-C. Plesa, A. Rivoldini, H. Samuel, S. St ahler, M. van Driel, T. Van Hoolst, O. Verhoeven, R. Weber, and M. Mieczorek. Premission insights on the interior of mars. *Space Science Reviews*, 215:3, 2019. doi: 10.1007/s11214-018-0563-9.

V. S. Solomatov. Scaling of temperature- and stress-dependant viscosity convection. *Physics of Fluids*, 7(2):266–274, 1995. doi: 10.1063/1.868624.

S. Squyres, R. T. Reynolds, A. L. Summers, and F. Shung. Accretional heating of the satellites of Saturn and Uranus. *Journal of Geophysical Research: Solid Earth*, 38 (B8):8779–8794, 1988. doi: 10.1029/JB093iB08p08779.

B. W. Stiles, R. L. Kirk, R. D. Lorenz, S. Hensley, E. Lee, S. J. Ostro, M. D. Allison, P. S. Callahan, Y. Gim, and L. Iess. Determining Titan's spin state from Cassini radar images. *Astronomical Journal*, 135(5):1669–1680, 2008. doi: 10.1088/0004-6256/135/5/1669.

V. Sun, K. Stack, L. Kah, L. Thompson, W. Fischer, A. Williams, S. Johnson, R. Wiens, R. Kronyak, M. Nachon, C. House, and S. VanBommel. Late-stage diagenetic concretions in the Murray formation, Gale crater, Mars. *Icarus*, 321:866 – 890, 2019. doi: 10.1016/j.icarus.2018.12.030.

R. Tajeddine, N. Rambaux, V. Lainey, S. Charnoz, A. Richard, A. Rivoldini, and

B. Noyelles. Constraints on Mimas' interior from Cassini ISS libration measurements. *Science*, 346(6207):322–324, 2014. doi: 10.1126/science.1255299.

P. C. Thomas. Sizes, shapes, and derived properties of the Saturnian satellites after the Cassini nominal mission. *Icarus*, 208(1):395–401, 2010. doi: 10.1016/j.icarus.2010.01.025.

P. C. Thomas and S. F. Dermott. The shape of Tethys. *Icarus*, 94(2):391–398, 1991. doi: 10.1016/0019-1035(91)90236-M.

P. C. Thomas, R. Tajedine, M. S. Tiscareno, J. A. Burns, J. Joseph, T. J. Loredo, P. Helfenstein, and C. Porco. Enceladus's measured physical libration requires a global subsurface ocean. *Icarus*, 264:37–47, 2016. doi: 10.1016/j.icarus.2015.08.037.

P. Tricarico. Multi-layer hydrostatic equilibrium of planets and synchronus moons: theory and application to Ceres and to solar system moons. *The Astrophysical Journal*, 782(2):99, 2014. doi: 10.1088/0004-637X/782/2/99.

D. Turcotte and G. Schubert. *Geodynamics*. Cambridge University Press, Cambridge (UK), 3 edition, 2014.

D. L. Turcotte, R. J. Willemann, W. F. Haxby, and J. Norberry. Role of membrane stresses in the support of planetary topography. *Journal of Geophysical Research: Solid Earth*, 86(B5):3951–3959, 1981. doi: 10.1029/JB086iB05p03951.

A. Vienne, L. Duriez, and S. CHampenois. The Mimas-Tethys and Enceladus-Dione

systems. *Symposium - International Astronomical Union*, 172:143–144, 1996. doi: 10.1017/S0074180900127251.

D. Wahl, M. Wieczorek, K. Wünnemann, and J. Oberst. Crustal porosity of lunar impact basins. *Journal of Geophysical Research: Planets*, 125(4), 2020. doi: 10.1029/2019JE006335.

W. R. Ward. Past orientation of the lunar spin axis. *Science*, 189(4200):377–379, 1975. doi: 10.1126/science.189.4200.377.

O. L. White, P. M. Schenk, A. W. Bellagamba, A. M. Grimm, A. J. Dombard, and V. J. Bray. Impact crater relaxation on Dione and Tethys and relation to past heat flow. *Icarus*, 288:37–52, 2017. doi: 10.1016/j.icarus.2017.01.025.

M. Wieczorek, G. Neumann, F. Nimmo, W. Kiefer, G. Taylor, H. Melosh, R. Phillips, S. Solomon, J. Andrews-Hanna, S. Asmar, A. Konopliv, F. Lemoine, D. Smith, M. Watkins, J. Williams, and M. Zuber. The crust of the Moon as seen by GRAIL. *Science*, 339(6120):671–675, 2013. doi: 10.1126/science.1231530.

J. Wisdom. Spin-orbit secondary resonance dynamics of Enceladus. *Astronomical Journal*, 128:484–491, 2004. doi: 10.1086/421360.

J. Wisdom, R. Dbouk, B. Militzer, W. B. Hubbard, F. Nimmo, B. G. Downey, and R. G. French. Loss of a satellite could explain Saturn's obliquity and young rings. *Science*, 377(6612):1285–1289, 2022. doi: 10.1126/science.abn1234.

T.-F. Wong and P. Baud. The brittle-ductile transition in porous rock: A review. *Journal of Structural Geology*, 44:25 – 53, 2012. doi: 10.1016/j.jsg.2012.07.010.

K. Zahnle, P. Schenk, H. Levison, and L. Dones. Crating rates in the ourter solar system. *Icarus*, 163(2):263–289, 2003. doi: 10.1016/S0019-1035(03)00048-4.

K. Zhang and F. Nimmo. Late-stage impacts and the orbital and thermal evolution of Tethys. *Icarus*, 218(1):348–455, 2012. doi: 10.1016/j.icarus.2011.12.013.

Z. Zhang, A. G. Hayes, M. A. Janssen, P. D. Nicholson, J. N. Cuzzi, I. de Pater, and D. E. Dunn. Exposure age of Saturn's A and B rings, and the Cassini Division as suggested by their non-icy material content. *Icarus*, 294:14–42, 2017. doi: 10.1016/j.icarus.2017.04.008.

V. Zharkov and T. Gudkova. Models, figures, and gravitational moments of Jupiter's satellite Io: effects of the second order approximation. *Planetary and Space Science*, 58(10):1381–1390, 2010. doi: 10.1016/j.pss.2010.06.004.